Mineral inclusions in diamonds from Chidliak (Nunavut, Canada): constraining the diamond substrates

by

Xinchen Xia

A thesis submitted in partial fulfillment of the requirements for the degree of

Master of Science

Department of Earth and Atmospheric Sciences
University of Alberta

Abstract

The Chidliak kimberlite pipe is located on the Hall Peninsula on Baffin Island in Nunavut. The first kimberlite in Chidliak was discovered in 2008. Previous studies (e.g., Hogberg et al., 2016) on Chidliak inclusion-free diamonds have suggested that 1) two diamond growth stages are recorded by carbon isotopic ratios and nitrogen concentrations; and 2) diamonds resided at temperatures from ~ 980 to 1350 ℃ corresponding to depths of ~ 150 to 200 km.

Seventy-four diamonds from the CH-7 kimberlite pipe at Chidliak were broken to release their mineral inclusions. The characteristics of major and minor elements of inclusions in diamond suggest a source dominated by eclogite, with a minor peridotitic component. The trace-element compositions of eclogitic garnet and clinopyroxene diamonds inclusions measured by laser ablation ICP-MS, and the presence of both negative and positive europium anomalies indicate low-pressure oceanic crustal protoliths.

Temperatures calculated from non-touching mineral inclusions reflect diamond formation at ~ 1050 to 1150 ℃ (derived from garnet-olivine associations and the single olivine thermometer). This result compares very well with the nitrogen-based mantle residence temperatures (~ 1000 to 1200 ℃) of the host diamonds, equivalent to a depth range of ~ 160 to 200 km when projected on the xenolith/xenocryst based local paleo-geotherm of 36 mW/m^2 (Pell et al., 2013).

Fragments of inclusion-bearing diamonds were measured via SIMS. The overall carbon isotopic data ($\delta^{13}C$ range of -25 to -1.6 ‰) shows a principal mode in class bin -5 to -4 ‰ (close to the typical mantle value: -5 ‰; Deines, 1980; Cartigny, 2005) with a secondary

mode in class bin -17 to -16 ‰, which is consistent with previous research (Hogberg et al., 2016) and an eclogite-dominated source determined from the suite of diamond inclusions. The $\delta^{13}C$ values of peridotitic and eclogitic diamonds range from -5.8 to -1.6 ‰ and -24.8 to -3.2 ‰, respectively. The $\delta^{15}N$ of peridotitic diamonds ranges from -6.9 to +4.7 ‰, whilst eclogitic diamonds have a broader distribution from -5.1 to +9.8 ‰. The narrow range in $\delta^{13}C$ of peridotitic diamonds is in agreement with a mantle-derived carbon source. For eclogitic diamonds, the characteristics and correlations of $\delta^{13}C$ and $\delta^{15}N$ indicate that the $\delta^{13}C$-depleted group (< -10 %) has a subduction origin, whereas the group with $\delta^{13}C$ > -10 ‰ results from mixing of predominantly mantle-derived fluids and subducted carbon. A lack of systematic correlations of $\delta^{13}C$-[N] and $\delta^{15}N$-[N] has been identified and is possibly due to the mixing of sources with distinct C and N, or the presence of more than one diamond population in the studied bulk sample.

Combining the SIMS data, CL imaging, and the presence of yellow-coated diamonds, at least two growth episodes of diamonds are revealed, with a resorption event between each stage. On the scale of individual diamonds, multiple pulses of fluids/melts are represented by the internal CL characteristics and associated variation in $\delta^{13}C$ values.

Acknowledgements

Firstly, I would like to express my special thanks of gratitude to my supervisor, Thomas Stachel, thank you for providing me an opportunity to learn about diamonds, for your constant guidance, encouragement, suggestions and patience. This study would not have been possible without diamond samples provided by Peregrine Diamonds Ltd.

I am grateful to Jeff Harris, for giving an introductory course to the world of diamonds and for assisting in breaking the first diamond in my life. The work reported here benefited from many experts of different laboratories. Thanks to Andrew Locock for the assistance with electron microprobe analyses of major and minor elements of inclusions within diamonds. Thanks are due to Richard Stern and Robert Dokken (CCIM: Canadian Centre for Isotopic Microanalysis), for helping with sample preparation, CL imaging and SIMS analyses. My thanks to Yan Luo for assisting with trace-element analyses using the laser ablation ICP-MS.

I heartily thank my colleagues and associates of the diamond research group, I really had a great time. With a special mention to Nicole Meyer who helped me a lot, for teaching me how to epoxy and polish diamonds, for discussions and suggestions about my work, and for help proofreading. My thanks to Theetso Motsamai for offering me valuable advice. Thanks to Matthew Hardman for helping to proofread. Thanks are due to Meiyan Lai, for guiding me to use FTIR.

Finally, I am much grateful to my family for encouraging and supporting me during the two years.

Table of Contents

List of Tables

List of Figures

List of Symbols and Abbreviations

~	Approximately
e.g.	For example
i.e.	That is
SCLM	Subcontinental lithospheric mantle
DTC	Diamond Trading Company
‰	Parts per thousand or per mille
%B	Percentage of nitrogen aggregated in B centers
$\delta^{13}C$	Carbon isotope composition relative to the international V-PDB standard
$\delta^{15}N$	Nitrogen isotope composition relative to air
CL	Cathodoluminescence
Cr#	Molar ratio of 100*Cr/(Cr+Al)
Mg#	Molar ratio of 100*Mg/(Mg+Fe)
G3	Eclogitic garnet
G4	Eclogitic/pyroxenitic garnet
G10	Harzburgitic garnet
G*D	"D" suffix denotes strong association with diamond
Ma	Millions of years ago
Ga	Billions of years ago
Myr	Millions of years
GPa	Gigapascal
FTIR	Fourier transform infrared spectroscopy
REE	Rare earth element
HREE	Heavy rare earth element
MREE	Medium rare earth element
LREE	Light rare earth element
Eu/Eu*	Geometric Eu anomaly calculated as $Eu_N/\sqrt{Sm_N * Gd_N}$
WDS	Wavelength Dispersive Spectrometry
EDS	Energy Dispersive Spectrometry

EPMA	Electron probe microanalyser
IR	Infrared
ICP-MS	Inductively couple plasma-mass spectrometry
SIMS	Secondary ion mass spectrometry
CCIM	Canadian Centre for Isotopic Microanalysis
Type Ib	Single substitutional nitrogen in diamond
Type IaA	Nitrogen in diamond aggregated A centers
Type IaAB	Nitrogen in diamond aggregated A and B centers
Type IaB	Nitrogen in diamond aggregated B centers
Type II	Nitrogen-free diamond
V-PDB	Vienna Pee Dee Belemnite
ppm	Parts per million
at. ppm	Atomic parts per million
σ	Sigma or one standard deviation from the mean
wt%	Weight percent
mW/m^2	Milliwatts per square meter
kbar	Kilobars
km	Kilometers
kV	Kilovolts

Chapter 1: Introduction

1.1. Introduction

Diamonds are brought to Earth's surface as xenocrysts instead of phenocrysts in kimberlite or lamproite magma (Richardson et al., 1984). Primary diamond deposits are mainly found in the most ancient and stable cratonic lithosphere (typically Archean in age), an almost exclusive association known as Clifford's Rule (Clifford, 1966; revised by Janse, 1994). The vast majority of diamonds (over 99 %) form in the region where subcratonic lithospheric mantle reaches into the diamond stability field (Boyd and Gurney, 1986; Stachel and Luth, 2015), which is equivalent to depths of typically 150 to 200 km but can be up to 250 km (Stachel and Harris, 1997; Cartigny et al., 2014). The subcratonic lithospheric mantle is highly depleted; compared with primitive mantle, cratonic peridotite is depleted in Al, Ca and Fe (Jordan, 1978; Stachel and Harris, 2008). The derivation of rare diamonds in the subcratonic lithosphere is linked to ascent of mantle-derived fluids and oceanic crust recycling into the mantle (Jordan, 1978; Boyd and Gurney, 1986; Stachel and Harris, 2008). Some diamonds derive from even greater depth (e.g., the transition zone and even the lower mantle; Harte & Harris, 1999).

Due to their economic value and scientific curiosity, diamond exploration and diamond studies are prevailing worldwide. Diamond is composed of nearly pure elemental carbon (sometimes substituted in trace amounts by other elements, such as nitrogen and hydrogen), and the carbon atoms are in a dense cubic crystal structure, which makes diamond the hardest known natural mineral phase, in addition to rendering it chemically inert. Because of the high purity of diamond, researchers focus attention on the solid minerals enclosed in diamonds instead of diamond itself (Stachel, 2014). Inclusions within diamonds are protected from interactions with fluids and melts, therefore, the original signatures of the cratonic mantle are well-preserved in subsequently changing environments. The geochemical studies on inclusions can shed light on diamond genesis and formation conditions (Meyer, 1987; Stachel, 2014), and provide useful tools for diamond exploration (Gurney, 1984).

The three suites of rocks that have been identified as substrates for diamond crystallization are peridotite, eclogite, and websterite. The upper mantle consists predominantly of peridotite whose mineral assemblage consists of olivine (> 40 %), orthopyroxene, clinopyroxene and garnet (and/or spinel). Clinopyroxene may disappear with increasing depletion, thus, in the order of depletion, peridotite can be termed as lherzolite (little to moderate depletion), harzburgite (strong depletion; with low to no clinopyroxene), dunite (extreme depletion; comprises > 90 % olivine; Le Maitre, 1989). Eclogite is composed principally of Na-rich omphacitic clinopyroxene and Cr-poor garnet (Cr_2O_3 < 1 wt%) and is a high-pressure metamorphic rock with a basaltic bulk composition (Stachel and Harris, 2009). The occurrence of the vast majority of eclogites in the lithospheric mantle is associated with a subduction origin (MacGregor & Manton, 1986; Jacob, 2004; Stachel and Harris, 2008). For inclusions in diamond, the composition of the websteritic suite is transitional between peridotite and eclogite, and there is no clear definition of websterite (e.g., Gurney et al., 1984). On the basis of the research on inclusion-bearing diamonds, peridotitic, eclogitic and websteritic substrates account for 65 %, 33 % and 2 %, respectively (Stachel and Harris, 2009).

Diamonds from the kimberlite pipes CH-6 and CH-7 at Chidliak have been studied by Nichols (2014; MSc thesis, partially published in Hogberg et al., 2016), however, those diamonds were void of mineral inclusions. According to Nichols (2014; MSc thesis), the time-averaged mantle residence temperatures calculated from nitrogen contents and aggregation states span a range of 980 to 1350 °C, with the majority of stones residing between 1000 and 1150 °C. Projected on the geotherm determined by Pell et al. (2012), the diamonds originated between 150 and 200 km. Based on CL images and distinct carbon isotope and nitrogen abundance signatures, two distinct stages of diamond growth are evident, with ^{13}C-depleted compositions and overall high nitrogen contents being indications for a partly to predominantly eclogitic origin (Hogberg et al., 2016).

1.2. Thesis Intent

The Chidliak project is an advanced exploration project by Peregrine Diamonds Ltd initiated in 2005. Kimberlite indicator minerals were collected during reconnaissance sampling of the Chidliak project area, and the first three kimberlites (CH-1, 2, 3) were explored in 2008 (Pell et al., 2013). All kimberlites found at Chidliak intrude Archean orthogneissic basement and supracrustal rocks (~2.92 to 2.80 Ga) at the Hall Peninsula block (Pell et al., 2012). All diamonds studied for this thesis are from the CH-7 kimberlite pipe.

The intent of this thesis is to determine the paragenesis of diamonds from Chidliak by studying the inclusion compositions and comparing the results with previous research on diamonds that lack mineral inclusions (Hogberg et al., 2016) to constrain the conditions of diamond formation. Physical characteristics and internal growth structures (imaged by CL) of diamonds can help to define diamond growth events. The compositions of inclusions measured by Electron Probe Microanalysis were used to decipher the paragenetic associations and evolution of the subcratonic lithospheric mantle. Inclusion- and nitrogen-based thermometers provided constraints on the physical conditions during diamond crystallization and mantle residence. Trace-element patterns of selected inclusions (eclogitic garnets and clinopyroxene), analyzed by Inductively Coupled Plasma Mass Spectrometry, were used to fingerprint the protoliths and metasomatic evolution of diamond substrates. Carbon and nitrogen isotope and nitrogen concentration measurements were completed by Secondary Ion Mass Spectrometry to identify the sources of diamond-forming fluids.

Chapter 2: Geological Background

2.1. Hall Peninsula

Until recently, the geology of the Hall Peninsula block (Figure 2.1) was poorly understood due to the limited amount of mapping that had been done (Blackadar, 1967). Subsequent research on Baffin Island has now provides more details on the geological and structural history (e.g., St-Onge et al., 2006, 2009; Corrigan et al., 2009; Whalen et al., 2010). Based on the early work and a geochronological study at reconnaissance scale conducted by Scott (1996), the Hall Peninsula region is segmented into three major lithological domains (Scott, 1996, 1999; St-Onge, et. al., 2006): the western domain (the Paleoproterozoic Cumberland Batholith), the central belt (Paleoproterozoic siliciclastic metasedimentary units and secondary metamorphosed plutonic rocks), and the eastern domain (Hall Peninsula Block; Figure 2.1).

2.1.1. Hall Peninsula Block

The tectonic setting of the Hall Peninsula block is still unclear, and it has been speculated that:

1) The metaplutonic rocks represent the distinct Archean Burwell microcontinent (Hoffman, 1989);

2) The Archean orthogneisses are reworked Archean gneisses within the Nagssugtoqidian Orogen, west Greenland (Jackson et al., 1990);

3) The eastern domain is the northern continuation of the Archean North Atlantic Craton (Scott and Campbell, 1993);

4) The Hall Peninsula block results from one of several microcontinents that were accreted during a two-phase, three-way collision of the Superior, Rae and North Atlantic cratons that occurred between 1.865 and 1.79 Ga (Snyder, 2010);

5) The “core zone”, made of the Hall Peninsula block, southern Cumberland Peninsula and Aasiaat domain, indicates the three-way collision of the North Atlantic craton, Rae craton and Incognita microcontinent (From et at., 2018).

On the basis of the results from U-Pb isotopic dating, the second and third assumptions are not mutually exclusive, as the Nagssugtoqidian collision (post-1.89 Ga) occurred prior to the collision in the Torngat Orogen (post-1.87 Ga; Scott, 1999), as discussed below.

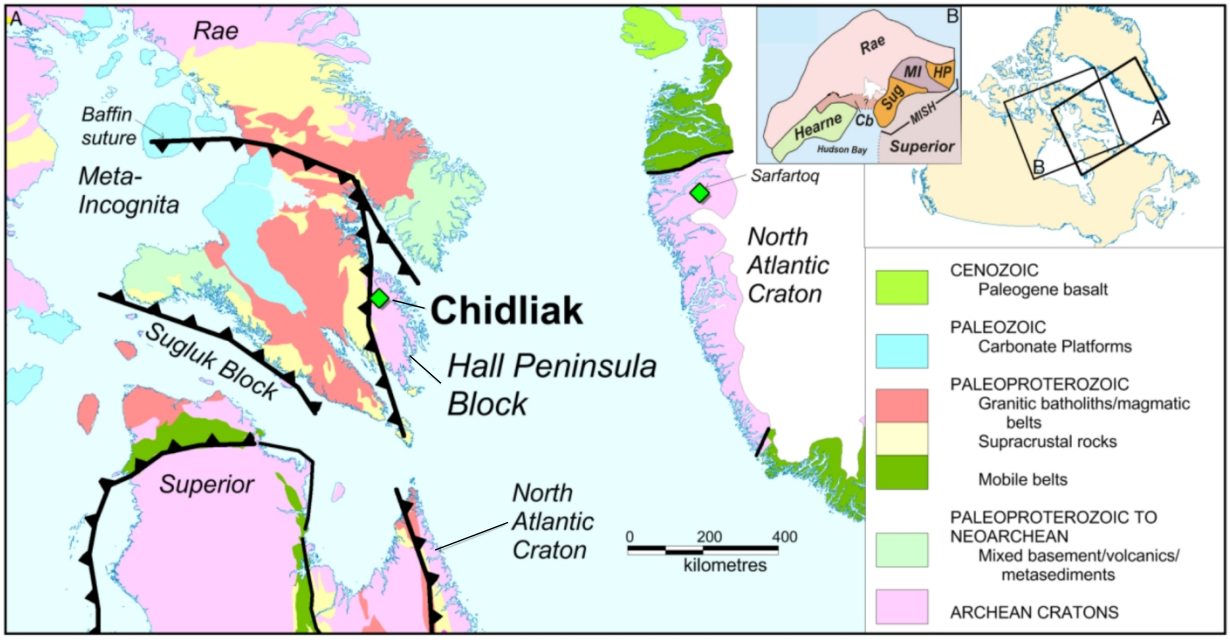

Figure 2.1. Location of the study area on the Hall Peninsula, southern Baffin Island. Figure is from Kopylova et al. (2017), modified from Chorlton (2007).

Hoffman (1989) posited that the eastern terrain of the Hall Peninsula is a microcontinent that belongs to the postulated Burwell craton. However, the southern part of this craton comprises the older Archean North Atlantic Craton and younger calc-alkaline intrusions, which have been dated as Proterozoic, at ca. 1.91-1.87 Ga (Scott, 1995a, b). The existence of the Burwell craton remains in doubt.

Jackson et al. (1990) suggested that Archean gneisses in the eastern domain of the peninsula are analogous to reworked gneisses on the Nagssugtoqidian Orogen (Aasiaat domain) of Western Greenland. Kalsbeek and Nutman (1995) documented the extent of metaplutonic rocks (~ 1.9 Ga) in the Archean gneisses (~ 2.9-2.6 Ga) of the Nagssugtoqidian orogen. Detailed U-Pb geochronological investigations in this orogen of Western Greenland (Connelly and Mengel, 1996) have established that magmatism

(~ 2.88-2.82 Ga) and orogeny (~ 2.81-2.75 Ga) occurred in the Archean and predated Paleoproterozoic tectonic thermal overprints (~ 1.85-1.83 Ga from zircon; ~ 1.78-1.72 Ga from titanite). Subsequently, Jackson et al. (1999) documented similar ages of magmatic events (~ 2.88-2.82 Ga) in West Greenland. These ages can be compared with the ages of the eastern tonalitic gneiss on the Hall Peninsular presented by Scott (1999). Moreover, the preservation of granulite-facies assemblages is variable within the Archean tonalitic orthogneiss of the eastern domain. From et al. (2012) proposed that the orthogneiss complex has been metamorphosed to granulite-grade by early metamorphic events, and subsequently overprinted by the amphibolite-grade metamorphism. Thus, the granulite-grade assemblages could be correlative with the granulite facies tonalitic gneiss of the Nagssugtoqidian orogen of West Greenland. The correlation between the Archean gneisses in the Hall Peninsula block and in West Greenland is strongly supported by lithological similarities, geochronologic data and metamorphic observations. However, it is worth noting that tonalitic gneisses have also been identified across every adjacent crustal entity (From, 2012).

Scott and Campbell (1993) proposed that the eastern Hall Peninsula is a northward continuation of the Archean North Atlantic Craton and Paleoproterozoic terranes in the Torngat Orogen, due to along-strike succession of the Paleoproterozoic units and tectonic thermal activities, which are considered to outline the ca. 1.9 Ga rim of the North Atlantic Craton. However, the North Atlantic Craton is characterized by discordant mafic dykes, which have not been apparent in the eastern domain of the Hall Peninsula (Scott, 1996). Thus, Scott (1996) supported the hypothesis that the eastern Hall Peninsula metaplutonic rocks are equivalents of intrusions (1.91-1.87 Ga) in the Burwell plutonic arc, which intrudes the North Atlantic Craton, and that the younger metasedimentary rocks are equivalent to the successive Tasiuyak gneiss in the Torngat Orogen. Furthermore, Scott (1996) proposed that the Hall Peninsula region is underlain by these Paleoprotozoic metaplutonic and metasedimentary units, while Hoffman (1989) held the opinion of an Archean basement. Representative samples collected by Scott (1996), from a corridor east of Iqaluit, were analyzed applying U-Pb isotopic dating. The orthopyroxene tonalite of the eastern terrain was observed to intrude supracrustal cover sequences of the central Hall Peninsula at 1890±2 Ma. The eastern metasedimentary cover rocks overlying the Archean

basement are considered to have the same origin as clastic units of the central portion, and they represent the northern continuation of the Tasiuya gneiss in the Torngat Orogen (northern Labrador). After further investigations, Scott (1999) concluded that the Archean rocks relate to the Archean gneisses of West Greenland, and the Paleoproterozoic cover rocks exposed within the central domain and contemporaneous tectono-thermal events in the eastern and intermediate terrains are related to the Torngat Orogen. Samples of the eastern Archean orthogneiss complex and supracrustal rocks have been examined by Scott (1999), producing a series of results from U-Pb and Pb-Pb isotopic dating. Four samples of tonalitic gneiss document a history of Mesoarchean magmatic events (~ 2.92-2.80 Ga), possible metamorphic activity occurred at ca. 2.77 Ga and subsequent tectono-thermal overprints took place between ca. 1.84-1.74 Ga during the Paleoproterozoic period, which suggest correlation with similar rocks in West Greenland. Rayner (2014) produced similar U-Pb zircon ages of Archean rocks recording identical tectonic thermal overprints at ca. 2.7 Ga and between ca. 1.86-1.74 Ga. Supracrustal rocks derived from Archean protoliths, were deposited before ca. 1.88 Ga (Rayner, 2014). These rocks were interpreted as the analogy of siliciclastic rocks (~ 1.96 Ga) in the western North Atlantic Craton (northern Labrador), despite of the interleaved contact with underlying Archean orthogneiss (Scott, 1999). In addition, some subordinate granitic veins formed between 1.84-1.76 Ga, due to the extensive metamorphism at that time (Scott, 1999). Structurally, the NNE trend of the Nagssugtoqidian suture zone is not compatible with the Torngat Orogen. U-Pb ages of subduction-related magmatism (~ 1.92-1.89 Ga) in Nagssugtoqidian, reported by Kalsbeek and Nutman (1995, 1996), indicate the time of collision (< 1.89 Ga). Magmatic events related to convergence in the Torngat Orogen occurred during 1.91-1.87 Ga, which implies that the age of Torngat collision is < 1.89 Ga. Therefore, Scott (1999) proposed that the Paleoproterozoic collision at the Nagssugtoqidian orogen of Western Greenland predated the collision at the Torngat Orogen by approximately 20 Myr.

Snyder (2010) suggested that the southeastern half of Baffin Island is one of several microcontinents formed during accretionary processes of a two-phase, three-way collision between 1.87 and 1.79 Ga, of the Superior, Rae and North Atlantic cratons. Indicator mineral garnets from Chidliak were analyzed by Snyder (2010) to constrain their origin and conditions of crystallization. Cr-Ca relationships were employed to indicate that some

G10 pyrope garnets originated in depleted Archean harzburgite at approximately 120-190 km depth. Such mantle rocks may have been provided by the Meta Incognita microcontinent, the Sugluk block or the Superior craton lithospheric keels.

From et al. (2018) grouped the Hall Peninsula block, the southern Cumberland Peninsula and the Aasiaat domain as "core zone" that resulted from a three-way collision between the North Atlantic Craton, the Rae craton and the Meta Incognita microcontinent. The magmatic and metamorphic zircons of orthogneiss samples were examined by From et al. (2018), indicating that 1) the U-Pb crystallization ages are between ca. 2.98 to 2.72 Ga and metamorphic ages between ca. 2.74 to 2.70 Ga; 2) εHf(t) signatures imply that the majority of magmatic rocks derive from the recycling of crust, and the magma source rocks were derived from the mantle at ~ 3.1 Ga; 3) the recycled Paleoarchean crust derived from depleted mantle with age modes of ca. 3.3 and 3.4 Ga, based on εHf(t) data of two Archean orthogneiss samples, and these rocks potentially come from the North Atlantic Craton.

2.1.2. Discussion

The Hall Peninsula is a petrologically diverse segment with a complicated tectonic and metamorphic history. The Archean orthogneiss complex and metasedimentary rocks show broad similarities with adjacent crustal blocks: the Meta Incognita microcontinent is similar to the Aasiaat terrain of West Greenland (Scott 1999; Hollis et al., 2006; Thrane and Connelly, 2006); the overlying Paleoproterozoic metasedimentary rocks are the northward continuation of the Torngat Orogen located in the northern Labrador (Scott and Gauthier, 1996; Scott, 1999).

The timing of kimberlite emplacement and the least radiogenic Sr/Nd isotope compositions from Chidliak perovskite are indistinguishable from Jurassic kimberlites in SW Greenland, which implies that the Chidliak block and the North Atlantic Craton share a common mantle source (Heaman el al., 2015). The bulk geochemical composition (carbonatitic metasomatism dominated) of mantle beneath Chidliak resemble the North Atlantic Craton, rather than SCLM beneath the adjacent Rae or Superior cratons (Wittig et al., 2008; Kopylova et al., 2017).

The present diamondiferous kimberlites are limited to within the eastern terrain of the Hall Peninsula, which implies that similar Archean rocks in Western Greenland are a potential diamond exploration area. Grütter and Tuer (2009) applied thermobarometry on clinopyroxenes and garnets from the Sarfartoq area, West Greenland, and revealed the existence of microdiamonds and the possibility of macrodiamond. Furthermore, Chidliak and the Sarfartoq region share a similar cool geotherm (~ 36 mW/m^2; Grütter and Tuer, 2009; Pell et al., 2012).

The preferred hypothesis is that the Hall Peninsula block formed part of the North Atlantic, and its formation relates to a convergence event (e.g., the collision of the North Atlantic Craton, Rae craton and Meta Incognita microcontinent/Superior craton; Snyder, 2010; From et al., 2018).

2.2. Exploration History and Chidliak Kimberlites

Southern Baffin Island was targeted for diamond exploration in 2005 by BHP Billiton (BHPB) and Peregrine Diamonds, with BHPB as operator, due to its underexplored state and the recovery of Paleoproterozoic to Mesoarchean zircons (Scott, 1999) suggesting an underlying Archean craton (Pell et al., 2013). Subsequently, kimberlite indicator minerals in this area were first reported in a regional till sampling survey. In 2008, the first three kimberlites CH-1, CH-2 and CH-3, were discovered. After further exploration, Pell et al. (2012) reported that 44 out of 64 kimberlites are diamondiferous, with 18 having commercial-sized diamonds; seven kimberlites contain diamonds of gem quality with coarse size-frequency distributions.

Heaman et al. (2012) combined U-Pb isotopic dating (via ID-TIMS) and Sr-Nd isotope analyses on groundmass perovskite to constrain the emplacement of Chidliak kimberlites to the Jurassic period between 156 to 138 Ma. Based on further U-Pb perovskite ages, the minimum duration of kimberlite emplacement was reported to be 157 and 139.1 Ma by Heaman et al. (2015). Combining the results of these two studies, Chidliak kimberlites are Jurassic and the duration of kimberlite magmatism spans from 157 to 138 Ma.

2.2.1. Kimberlite CH-7

The discovery of the CH-7 kimberlite occurred during ground exploration in 2009. CH-7 is located about 150 km from Iqaluit, Nunavut, and is a steep-sided, southwest-plunging body, having at least two distinct lobes with elliptical outlines and an estimated surface area of about one hectare (Pell et al., 2013). CH-7 comprises five principal geological units with distinct physical or geochemical characteristics, and some minor units: KIM-1 is a coherent kimberlite and coarse-grained; KIM-2 (volumetrically dominant), KIM-3 (apparently rootless) and KIM-4 are pyroclastic kimberlites; and KIM-5 (pyroclastic kimberlite and apparent coherent kimberlite) is of variable texture and variably lateritized (Nowicki et al., 2016). Various kinds of mantle xenoliths, including peridotites, eclogites and pyroxenites, are found in all of the kimberlite units at CH-7, with KIM-1 containing xenoliths greater than 30 cm in diameter (Nowicki et al., 2016).

Chapter 3: Diamonds from the Chidliak Kimberlites on the Hall Peninsula Block, Nunavut, Canada

3.1. Introduction

Seventy-four diamonds that contained visible potential mineral inclusions were collected from the main geological units KIM-2 to KIM-5 of the Chidliak kimberlite pipe CH-7 following exploration bulk sampling in 2015. The diamonds are in the DTC (Diamond Trading Company) sieve size range of -3 to -1 (i.e. about 1 mm in diameter). After visual inspection under a binocular microscope, their morphology, colour, surface textures, extent of resorption and signs of plastic deformation were photographed and described in Table 3.1. After recovery through breakage of their diamond hosts, inclusions were mounted individually and prepared for subsequent analysis.

A CAMECA SX100 electron microprobe was used to obtain major- and minor-element compositions of the inclusions, and high-precision analyses of the Al, Ca and Cr contents of olivine inclusions. Trace elements were determined by laser ablation ICP-MS. Nitrogen abundances and aggregation states within diamonds were measured using a Thermo Scientific Nicolet Nexus 470 FTIR spectrometer connected to a continuum IR microscope. The features of internal zonations were imaged by CL. The carbon and nitrogen isotope compositions and nitrogen concentrations were measured by a Cameca IMS1280 ion microprobe. Details on analytical methods are provided in Appendix A.

3.2. Physical Characteristics

3.2.1. Morphology

Various morphologies are displayed by natural diamonds, and these shapes provide important information on the diamond crystallization and growth environment (Tappert & Tappert, 2011). Three major types of diamonds (monocrystalline, fibrous, and polycrystalline) are classified according to Harris et al. (1975) and Tappert & Tappert (2011). Natural monocrystalline diamonds always occur in octahedral, cubic and dodecahedral habit. Rounded dodecahedra are normally the result of resorption (Moore et

Table 3.1. Physical characteristics of Chidliak diamonds

Sample	DTC Sieve Size	Morphology	Color	Surface Textures									Resorption	Inclusion (other than graphite)
				Stacked growth layers	Shield-shaped laminae	Trigons	Hexagons	Tetragons	Hillocks	Terraces	Late-Stage Etching	P.D.		
B1K5-1	-3+1	do	light brown		y				y	y			moderate	
B1K5-2	-3+1	o-agg	colorless	y		y-							weak	
B1K5-3	-3+1	o (flattened)	colorless											y
B1K5-4	-3+1	f	brown										weak-moderate	
B1K5-5	-3+1	cf	brown					y+			y		weak	
B1K5-6	-3+1	I	colorless	y		y								
B1K5-7	-3+1	of	light brown	y		y-							weak	
B1K5-8	-3+1	I	colorless			y					y		moderate	
B2K4-1	-3+1	f (flattened)	colorless	y							y		weak	y
B2K4-2	-3+1	o	colorless	y		y+					y			
B2K4-3	-3+1	o	light brown	y										
B2K4-4	-3+1	o	colorless	y		y-					y			
B2K4-5	-3+1	macle	brown			y-				y	y		moderate	
B2K4-6	-3+1	o	brown	y	y	y-					y		weak	y
B2K4-7	-3+1	o-agg (twin)	yellow	y	y	y-							weak	
B2K4-8	-3+1	do	colorless	y	y				y	y			pseudo-hemimorphic	y
B2K4-9	-3+1	o-agg	colorless	y	y	y-							weak	
B2K4-10	-3+1	I	colorless	y		y							moderate	y
B2K4-11	-3+1	of	colorless	y										
B2K4-12	-3+1	of	light brown	y		y					y		moderate	y
B2K4-13	-3+1	o-agg	colorless	y	y								weak	
B2K4-14	-3+1	I	light yellow	y							y			y
B2K4-15	-3+1	o-agg	colorless	y	y	y-					y		weak	
B2K4-16	-3+1	I	colorless	y						y	y			y
B2K4-17	-3+1	I	colorless								y			
B2K4-18	-3+1	f	yellow	y		y					y		weak	
B3K3-1	-3+1	of	brown	y		y-							weak	
B3K3-2	-3+1	of	colorless						y				weak-moderate	
B3K3-3	-3+1	I	intense yellow											

Table 3.1. cont.

Sample	DTC Sieve Size	Morphology	Color	Surface Textures									Resorption	Inclusion (other than graphite)
				Stacked growth layers	Shield-shaped laminae	Trigons	Hexagons	Tetragons	Hillocks	Terraces	Late-Stage Etching	P.D.		
B3K3-4	-3+1	df	brown			y-			y				mod-strong	
B4WK2-1	-3+1	o	brown	y							y			y
B4WK2-2	-3+1	o	light brown	y	y	y-					y		weak	y
B4WK2-3	-3+1	I	colorless											
B4WK2-4	-3+1	o-agg	colorless	y		y-					y			
B4WK2-5	-3+1	o-agg	colorless	y	y	y-							weak	
B4WK2-6	-3+1	I	light yellow	y		y-							weak	
B4WK2-7	-3+1	cf (fibrous)	colorless										weak	
B4WK2-8	-3+1	cf	colorless					y-					weak	
B4WK2-9	-3+1	of	colorless			y-					y		weak	
B4WK2-10	-3+1	I	light yellow			y					y			
B4WK2-11	-3+1	I	light brown			y							weak-moderate	
B4WK2-12	-3+1	of	brown	y	y						y		weak	
B5K2-1	-3+1	cf (re-entrant)	yellow					y-			y		weak-moderate	
B5K2-2	-3+1	o-agg	brown	y	y						y		weak-moderate	y
B5K2-3	-3+1	do-agg	brown	y	y				y	y			moderate-strong	
B5K2-4	-3+1	od	colorless	y		y-					y		moderate-strong	y
B5K2-5	-3+1	do	colorless	y	y	y-			y	y			moderate	
B5K2-6	-3+1	o	light brown	y										
B5K2-7	-3+1	I	colorless								y			
B5K2-8	-3+1	I	light brown		y								moderate	
B5K2-9	-3+1	do	colorless		y				y				modertate	
B5K2-10	-3+1	f	colorless			y	y				y			y
B5K2-11	-3+1	f (fibrous)	colorless										weak	
B5K2-12	-3+1	o	colorless	y		y-							moderate	
B5K2-13	-3+1	o	colorless											
N1K5-1	-1	o	brown	y	y	y-					y		weak	y
N1K5-2	-1	od (elongate, rounded)	colorless			y			y	y			mod-strong	y

Table 3.1. cont.

Sample	DTC Sieve Size	Morphology	Color	Surface Textures									Resorption	Inclusion (other than graphite)
				Stacked growth layers	Shield-shaped laminae	Trigons	Hexagons	Tetragons	Hillocks	Terraces	Late-Stage Etching	P.D.		
N1K5-3	-1	o-agg	light brown	y		y-					y			
N2K4-1	-1	d	yellow						y	y		y	mod-strong	
N2K4-2	-1	f	brown										moderate	y
N2K4-3	-1	I (knobbed)	colorless	y										
N2K4-4	-1	o	light brown	y	y	y-					y		weak	y
N2K4-5	-1	of (flattened)	colorless		y	y			y		y		weak	y
N2K4-6	-1	o-agg (twin)	colorless	y	y	y-							weak	y
N2K4-7	-1	od	brown	y		y-			y	y			pseudo-hemimorphic	y
N2K4-8	-1	I	brown	y		y		y			y		weak	y
N3K3-1	-1	f (yellow coat)	colorless, yellow			y								
N5K2-1	-1	do	colorless	y	y	y-			y	y			weak-moderate	
N5K2-2	-1	o	brown	y		y-					y		weak	y
N5K2-3	-1	I (rounded)	brown, colorless			y							strong	
N5K2-4	-1	od-agg	colorless	y									weak	
N5K2-5	-1	I	light brown	y		y					y			y
N5K2-6	-1	do	colorless	y	y	y-							moderate	
N5K2-7	-1	I	colorless/brown	y		y			y		y		weak	y

o=octahedron, d=dodecahedron, c=cuboid, agg=aggregate, f=fragment, I=irregular; P.D.=plastic deformation; ‘y’ means surface feature is identified, ‘-’ indicates negative orientation, ‘+’ indicates positive orientation

al. 1974), whereas octahedra and cubes reflect original habits. A variety of shapes can be observed among diamonds from worldwide deposits, but these habits generally result from the modification of primary forms (Tappert & Tappert, 2011).

As incomplete transitions in crystal form from octahedra (o) to dodecahedra (d) exist, a 50 % rule is applied to place the transitional shape into one of the two classes (e.g., do: octahedral faces dominant; od: dodecahedral faces dominant; Harris et al., 1975). A similar division is employed for irregular diamonds: if a diamond exhibits < 50 % of its original shape it will be designated as irregular; if not, it will be classified into the corresponding shape division (Harris et al., 1975). In addition, diamond aggregates of two or more crystals growing together are subdivided based on the above classifications, when distinct single crystal shapes can be distinguished (Harris et al., 1975), such as o-agg (octahedral aggregates). Diamond fragments with remaining broken surfaces are categorized according to the initial morphology (e.g., cubic fragment) and the category of fragments is applied if the original shape is discernible (Hogberg et al., 2016).

It is clear from the Table 3.1. that the studied small Chidliak diamonds are predominantly irregular (24 %). The second largest percentage of morphologies are octahedra (18 %, including one flattened octahedral crystal), followed by octahedral aggregates and twins (including macles, 15 %). Fragments constitute a large proportion and are categorized based on the recognizable primary features: octahedral, cubic, dodecahedral as well as fragments of unknown shape make up 11 %, 10 %, 4 % and 1 % respectively. Transitional morphologies are also present, with dodecahedron-octahedron (do; 8 %) having a significantly higher proportion than octahedron-dodecahedron (od; 5 %). Other minor shapes include rounded dodecahedra (1 %) and dodecahedral-octahedral aggregates (do aggregates; 1 %). In addition, a pseudohemimorphic sample (N2K4-7) with distinct resorption (rounded dodecahedral part and octahedral part) is present; such samples form because the octahedral part was enclosed in a xenolith that prevented resorption in the magma during kimberlite ascent.

3.2.2. Colour

Natural diamonds, controlled by colour centers, inclusions, strain and other factors, can display various colours. Diamonds are most commonly colourless, brown and yellow. Imperfections of and impurities in the diamond lattice can lead to transparent colours (Tappert & Tappert, 2011); Different colour centers result from different imperfections and impurities (Collins, 1982). The abundance of colour centers and the grain size of diamonds strongly affect the body colour: large diamonds usually display more intense colour than small ones (Tappert & Tappert, 2011). Yellow colour is produced by nitrogen impurities (N_3V center) which substitute for carbon in the atomic structure (Evans, T., & Phaal, C., 1962). Brown colouration is linked to plastic deformation caused by shearing stress under conditions of high temperature and high pressure (DeVries, 1975). However, the surface features indicative of deformation (e.g., deformation lines on dodecahedral faces) are generally absent at CH-7 and only observable on one stone (diamond N2K4-1). Inclusions of minerals/fluids also produce an effect on transparency and body colour. For instance, a cluster of graphite can cause opaque grey to black colour. In addition, the colour of diamond may vary slightly under different sources of light (Tappert & Tappert, 2011).

Just over half of the examined diamonds from CH-7 are colourless. Brown colours range from light to relatively dark brown and make up 31 %, followed by yellow tones (intense yellow to light yellow; 15 %). A further 2 % have mixed colours, such as colourless/yellow and colourless/brown.

3.2.3. Surface Textures

A large diversity of surface features is present on diamonds. They may result from dissolution of diamonds during residence in the mantle (due to metasomatism) or kimberlite ascent, or at various stages after diamond crystallization and shed light on the history of a diamond (Tappert & Tappert, 2011). Figure 3.1 summarizes the common surface textures, with certain features being found exclusively on specific crystal faces and others being observed on any face. Stacked growth layers (also known as triangular plates), shield-shaped laminae, trigons (both positive and negative), and hexagons (combination of positive and negative trigons; Evans and Sauter, 1961) are surface features only seen on octahedral crystal faces. A limited number of surface textures occur on cubic faces including positive and negative tetragons. Since the formation of dodecahedra is related to

resorption, the following textures are only present on dodecahedral surfaces: features resulting from resorption (terraces, hillocks and exhumation of plastic deformation lines) and features caused by late-stage etching (corrosion sculpture, shallow depressions, micro-disk patterns and micro-pits). Deformation lines first demonstrated by Williams (1932), suggest that diamonds have experienced plastic deformation by the displacement of carbon along octahedral planes (Phaal, C., 1964) and are often associated with brown body colour. Non-restricted surface textures include late-stage etching features (frosting, enhanced luster and ruts) and some distinctive textures related to placer deposition (e.g., percussion marks).

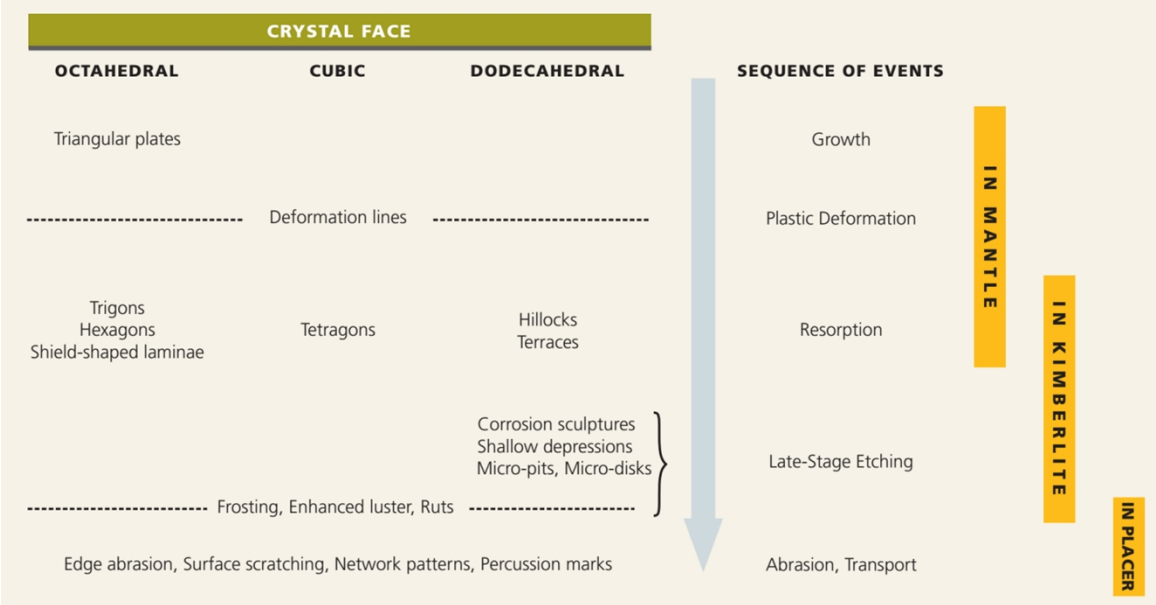

Figure 3.1. Common surface textures of diamonds and their sequence of formation. Figure is from Tappert & Tappert (2011).

On the octahedral faces of Chidliak samples (including octahedrons, octahedral aggregates, macles, octahedral fragments, octahedron-dodecahedron, dodecahedron-octahedron, fragments and irregular), the textures include stacked growth layers, shield-shaped laminae, trigons and hexagons. Both negative and positive trigons occur, with the positive type (only seen on one diamond) being much less common than the negative type. Negatively oriented

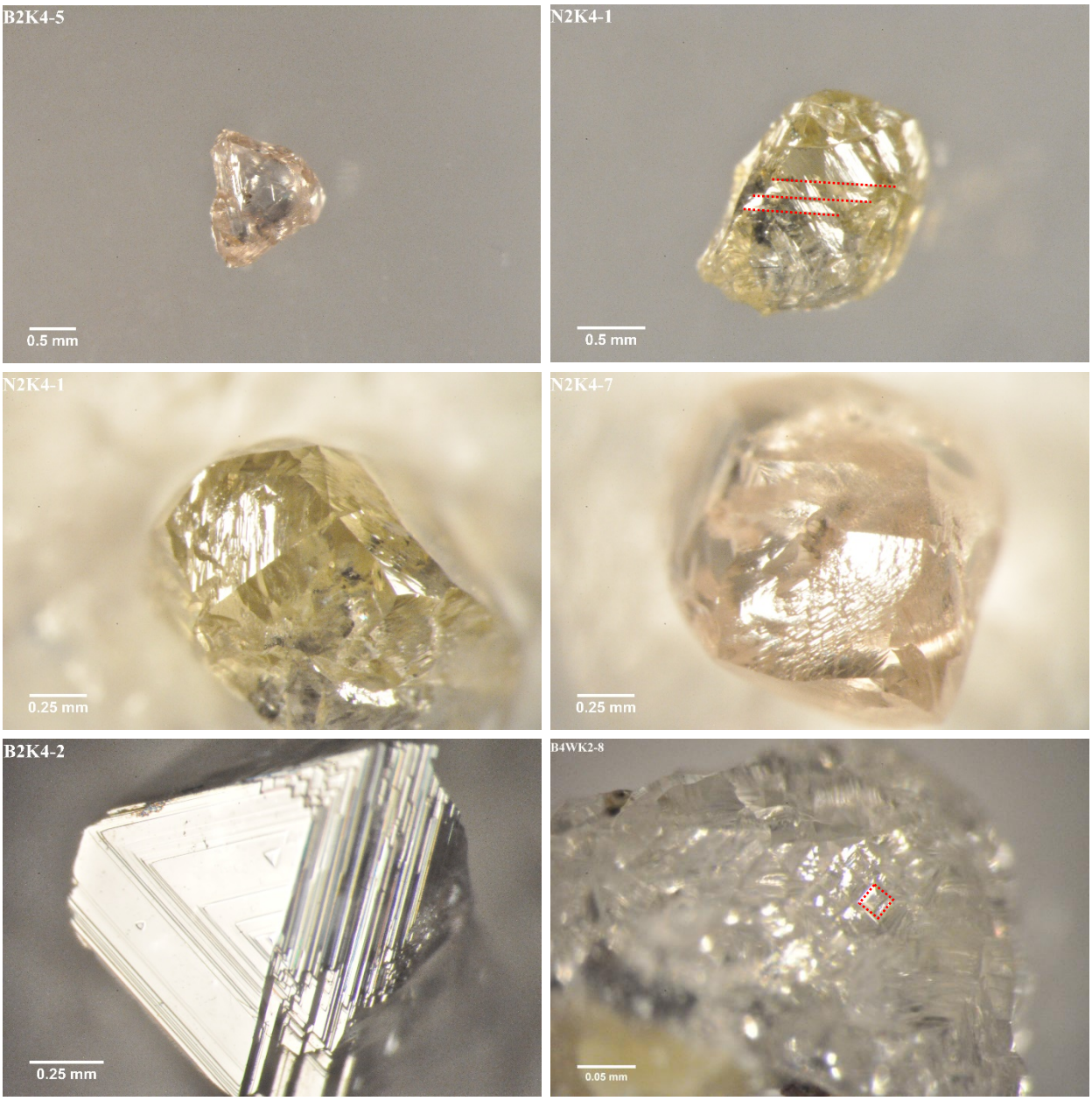

Figure 3.2. Examples of physical characteristics of Chidliak samples: a macle (B2K4-5), deformation lines (N2K4-1), terraces (N2K4-1), hillocks (N2K4-7), stacked growth layers (B2K4-2), tetragon (B4WK2-8).

tetragons are present on two cubic fragments, a third has tetragons in the positive orientation. Typical dodecahedral surface textures, such as hillocks and terraces are observable on most samples with dodecahedral faces (e.g., octahedron-dodecahedron), several fragments and some irregular diamonds. Deformation lines are only seen on

diamond N2K4-1. Textures resulting from late-stage etching (such as corrosion sculpture and ruts) are observed on nearly half of the studied samples.

3.2.4. The Resorption and Breakage of Diamonds

Resorption of diamonds may occur during the time of mantle residence or result from reaction between diamond and kimberlite magma during emplacement (Zhang and Fedortchouk, 2012). Based on the morphology and textural features, the extent of resorption of the examined diamonds classified from weak to strong. Individual samples experienced different degrees of resorption, but most resorbed stones exhibit weak to moderate resorption (Table 3.1). An uneven resorbed, pseudohemimorphic diamond (N2K4-7) was also observable. Part of this diamond was enclosed and preserved by the xenolith from the fluid/melt, while the other part was exposed and resorbed.

An unusually high level of diamonds breakage was identified in the 2015 CH-7 bulk sample (75 to 90 %; Nowicki et al., 2016) largely due to sample collection during large-diameter RC (reverse-circulation) drilling (McCandless, 2016a, b and c). Fragmentation increases with decreasing diamond size, consistent with similar observations on mechanical breakage of diamonds collected by RC drilling from KIM-2 to KIM-5 (McCandless, 2016a, b and c; Nowicki et al., 2016).

Thirty-one percent of examined diamonds from CH-7 in this study exhibit mechanical breakage surfaces, and 34 % of stones show resorbed breakage surfaces. Diamonds exhibiting unresorbed mechanical breakage surfaces, imply that the breakage occurred after emplacement and is possibly attributed to drilling and diamond recovery. For some diamonds with resorbed and etched breakage surfaces, the breakage must have happened before emplacement (mantle residence or kimberlite ascent) and resulted from fragmentation in the kimberlite.

3.3. Inclusions in Chidliak Diamonds

For diamonds from the subcratonic lithospheric mantle, mineral inclusions can be assigned on the basis of chemical composition into three suites (Meyer, 1987; Stachel & Harris,

2008): peridotitic (or ultramafic), eclogitic and websteritic. The peridotitic suite can be subdivided into lherzolitic, harzburgitic and wehrlitic parageneses. The websteritic suite is rare, and its chemical composition is transitional between the eclogitic and peridotitic suites (Gurney et al., 1984). Other minor suites (e.g., the calc-silicate suite described by Sobolev et al., 1984) have been identified. These suites reflect different geochemical environments of diamond formation.

Inclusions in diamonds are frequently less than 100 μm in maximum diameter (Meyer and Boyd, 1972), and large inclusions tend to be present in large diamonds even if no clear relationship has been noted (Meyer,1987). Typically, diamonds contain only one type of inclusion mineral, but sometimes multiple phases can be observed. Generally, inclusions are separated from each other. Separate inclusions can deliver insights into the conditions of diamond formation (Meyer, 1987).

On the basis of the genetic relationship between inclusions and host diamond, according to Meyer (1987), mineral inclusions are classified into three types: protogenetic (crystallized before their host diamond), syngenetic (grew contemporaneously with the host diamond) and epigenetic (postdates the host diamond). Protogenetic and syngenetic inclusions can be distinguished by their external shape: protogenetic ones tend to present irregular shapes or their typical mineral crystal form, while syngenetic inclusions are likely to have imposed morphologies and exhibit crystallographic controlled relationships with their diamond host (Harris and Gurney, 1979; Meyer, 1987). The genesis of epigenetic inclusions relates to penetration of fluids/melts along fractures in diamonds (Harris, 1968b), and their formation may occur during kimberlite ascent or residence on Earth's surface (Meyer, 1987). Syngenetic inclusion-bearing diamonds allow for absolute radiometric dating of diamond formation. Over the past three decades, ages of diamonds have been determined by the Rb-Sr, Sm-Nd and Ar-Ar systems on silicate inclusions, and the Pb-Pb (e.g., Rudnick et al., 1993) and Re-Os system (e.g., Pearson et al., 1999) on sulphides.

After visual examination, all seventy-four diamonds from CH-7 were crushed to release inclusions using a steel cracker. Twenty-two of these diamonds contained syngenetic inclusions which were then investigated by electron microprobe for their chemical compositions. For the remaining stones, no inclusions were recovered (excluding graphite)

Table 3.2. Electron microprobe data of syngenetic inclusions

Sample	B2K4-1a	B2K4-1b	B2K4-14a	B2K4-14b	B2K4-14c	B2K4-14d	B2K4-16	B4WK2-1a	B4WK2-1b	B4WK2-1c	B4WK2-2a	B4WK2-2b
Mineral	Grt	Grt	Cpx	Cpx	Cpx	Cpx	Grt	Grt	Ol	Ol	Rutile	Rutile
Assemblage	Grt	Grt	Cpx	Cpx	Cpx	Cpx	Grt	Grt, Ol	Grt, Ol	Grt, Ol	Rutile, Sul	Rutile, Sul
Paragenesis	E	E	E	E	E	E	E	P	P	P	E	E
SiO_2	40.44	40.13	55.78	55.82	55.81	55.50	41.35	41.07	41.85	41.46	0.02	⩽0.01
TiO_2	0.76	0.73	0.62	0.64	0.60	0.61	0.39	0.04	⩽0.01	⩽0.01	97.11	97.71
Al_2O_3	22.63	22.43	19.37	19.62	19.66	19.79	23.38	15.56	⩽0.01	⩽0.01	0.64	0.71
V_2O_3	0.02	0.03	0.06	0.05	0.04	0.06	⩽0.01	0.05	⩽0.01	⩽0.01	0.27	0.26
Cr_2O_3	0.03	0.04	0.06	0.05	0.05	0.05	0.08	11.40	0.05	0.05	0.03	0.03
FeO	14.30	13.74	2.44	2.50	2.44	2.45	10.90	6.33	7.42	7.41	1.06	0.78
NiO	⩽0.01	⩽0.01	⩽0.01	⩽0.01	⩽0.01	⩽0.01	⩽0.01	⩽0.01	0.38	0.37	⩽0.01	⩽0.01
MnO	0.22	0.20	0.02	0.02	⩽0.01	0.02	0.22	0.34	0.10	0.10	⩽0.01	⩽0.01
MgO	8.98	8.83	4.62	4.63	4.58	4.53	13.96	20.91	51.22	50.76	0.02	0.02
CaO	12.95	13.35	9.25	9.48	8.86	9.26	10.53	4.52	0.04	⩽0.01	⩽0.01	⩽0.01
Na_2O	0.28	0.27	7.65	7.73	7.50	7.59	0.13	⩽0.01	⩽0.01	⩽0.01	⩽0.01	0.02
K_2O	0.02	⩽0.01	0.14	0.15	0.14	0.14	⩽0.01	⩽0.01	⩽0.01	⩽0.01	⩽0.01	⩽0.01
P_2O_5	0.08	0.10	0.02	0.03	0.02	0.03	0.02	⩽0.01	⩽0.01	⩽0.01	⩽0.01	⩽0.01
Total	100.72	99.86	100.03	100.72	99.73	100.04	100.99	100.24	101.04	100.18	99.46	99.82
Si	3.00	3.00	1.93	1.92	1.93	1.92	2.98	2.99	1.00	1.00	0.00	0.00
Ti	0.04	0.04	0.02	0.02	0.02	0.02	0.02	0.00	0.00	0.00	1.97	1.97
Al	1.98	1.97	0.79	0.80	0.80	0.81	1.99	1.33	0.00	0.00	0.02	0.02
V	0.00	0.00	0.00	0.00	0.00	0.00	0.00	0.00	0.00	0.00	0.01	0.01
Cr	0.00	0.00	0.00	0.00	0.00	0.00	0.00	0.66	0.00	0.00	0.00	0.00
Fe^{2+}	0.89	0.86	0.07	0.07	0.07	0.07	0.66	0.39	0.15	0.15	0.02	0.02
Ni	0.00	0.00	0.00	0.00	0.00	0.00	0.00	0.00	0.01	0.01	0.00	0.00
Mn	0.01	0.01	0.00	0.00	0.00	0.00	0.01	0.02	0.00	0.00	0.00	0.00
Mg	0.99	0.98	0.24	0.24	0.24	0.23	1.50	2.27	1.83	1.83	0.00	0.00
Ca	1.03	1.07	0.34	0.35	0.33	0.34	0.81	0.35	0.00	0.00	0.00	0.00
Na	0.04	0.04	0.51	0.52	0.50	0.51	0.02	0.00	0.00	0.00	0.00	0.00
K	0.00	0.00	0.01	0.01	0.01	0.01	0.00	0.00	0.00	0.00	0.00	0.00
P	0.01	0.01	0.00	0.00	0.00	0.00	0.00	0.00	0.00	0.00	0.00	0.00
Total	7.99	7.98	3.91	3.92	3.90	3.91	8.01	8.01	3.00	3.00	2.02	2.02
Oxygens	12.00	12.00	6.00	6.00	6.00	6.00	12.00	12.00	4.00	4.00	4.00	4.00
Mg#	52.81	53.41	77.14	76.75	77.00	76.74	69.55	85.49	92.49	92.43		

Table 3.2. Cont.

Sample	B5K2-10	N1K5-1	N2K4-2	N2K4-4	N2K4-5a	N2K4-5b	N2K4-5c	N2K4-6	N2K4-8	N5K2-5
Mineral	Ol	Ol	Grt	Ol	Grt	Cpx	Cpx	Ol	Cpx	Cpx
Assemblage	Ol	Ol	Grt	Ol	Grt, Cpx	Grt, Cpx	Grt, Cpx	Ol	Cpx	Cpx
Paragenesis	P	P	E (-W)	P	E	E	E	P	E	E
SiO_2	41.36	41.49	42.57	40.99	40.79	54.96	54.80	41.38	55.40	54.08
TiO_2	⩽0.01	⩽0.01	0.17	⩽0.01	0.56	0.41	0.42	⩽0.01	0.73	0.60
Al_2O_3	⩽0.01	⩽0.01	23.63	⩽0.01	22.82	11.91	12.15	⩽0.01	15.19	20.32
V_2O_3	⩽0.01	⩽0.01	0.06	⩽0.01	⩽0.01	0.03	0.05	⩽0.01	0.05	0.06
Cr_2O_3	0.04	0.05	0.30	0.03	0.05	0.03	0.03	0.04	0.04	0.06
FeO	8.85	6.74	8.83	7.19	12.34	3.51	3.53	6.83	4.01	3.42
NiO	0.38	0.36	⩽0.01	0.34	⩽0.01	0.02	0.03	0.36	⩽0.01	⩽0.01
MnO	0.11	0.08	0.39	0.10	0.25	0.02	0.02	0.09	0.03	0.05
MgO	49.94	52.14	20.49	50.45	12.22	9.19	9.15	51.97	6.45	4.98
CaO	0.06	⩽0.01	4.69	0.02	11.40	13.66	13.21	⩽0.01	10.92	9.80
Na_2O	⩽0.01	⩽0.01	0.03	⩽0.01	0.18	6.65	6.68	⩽0.01	6.76	6.78
K_2O	⩽0.01	⩽0.01	⩽0.01	⩽0.01	⩽0.01	0.05	0.03	⩽0.01	0.11	0.13
P_2O_5	⩽0.01	⩽0.01	0.03	⩽0.01	0.02	0.02	0.02	⩽0.01	0.02	0.03
Total	100.75	100.88	101.20	99.14	100.66	100.48	100.13	100.71	99.73	100.31
Si	1.00	0.99	2.99	1.00	2.98	1.95	1.94	0.99	1.95	1.88
Ti	0.00	0.00	0.01	0.00	0.03	0.01	0.01	0.00	0.02	0.02
Al	0.00	0.00	1.95	0.00	1.97	0.50	0.51	0.00	0.63	0.83
V	0.00	0.00	0.00	0.00	0.00	0.00	0.00	0.00	0.00	0.00
Cr	0.00	0.00	0.02	0.00	0.00	0.00	0.00	0.00	0.00	0.00
Fe^{2+}	0.18	0.14	0.52	0.15	0.75	0.10	0.10	0.14	0.12	0.10
Ni	0.01	0.01	0.00	0.01	0.00	0.00	0.00	0.01	0.00	0.00
Mn	0.00	0.00	0.02	0.00	0.02	0.00	0.00	0.00	0.00	0.00
Mg	1.80	1.86	2.14	1.84	1.33	0.49	0.48	1.86	0.34	0.26
Ca	0.00	0.00	0.35	0.00	0.89	0.52	0.50	0.00	0.41	0.36
Na	0.00	0.00	0.00	0.00	0.03	0.46	0.46	0.00	0.46	0.46
K	0.00	0.00	0.00	0.00	0.00	0.00	0.00	0.00	0.00	0.01
P	0.00	0.00	0.00	0.00	0.00	0.00	0.00	0.00	0.00	0.00
Total	3.00	3.00	8.02	3.00	8.01	4.02	4.02	3.00	3.94	3.92
Oxygens	4.00	4.00	12.00	4.00	12.00	6.00	6.00	4.00	6.00	6.00
Mg#	90.96	93.24	80.53	92.60	63.84	82.36	82.21	93.13	74.12	72.19

Table 3.2. Cont.

Sample	B2K4-6	B2K4-8	B2K4-12	B4WK2-2	B5K2-2	B5K2-4	N1K5-2	N2K4-7	N5K2-2a	N5K2-2b	N5K2-7a	N5K2-7b
Mineral	Mss	Pyrrh.	Pyr.	Pyrrh.	Pyrrh.	Pent.	Pyrrh.	Pyrrh.	Pyrrh.	Pyrrh.	Pyrrh.	Pyrrh.
Assemblage	(Fe, Ni)S	FeS	FeS	FeS	FeS	(Fe, Ni)S	FeS	FeS	FeS	FeS	FeS	FeS
Paragenesis	P	E	E	E	E	P	E	E	E	E	E	E
Si	⩽0.01	⩽0.01	⩽0.01	⩽0.01	⩽0.01	⩽0.01	⩽0.01	⩽0.01	⩽0.01	⩽0.01	⩽0.01	⩽0.01
Zn	⩽0.01	⩽0.01	⩽0.01	⩽0.01	⩽0.01	⩽0.01	⩽0.01	⩽0.01	0.02	⩽0.01	0.02	⩽0.01
Cr	0.30	⩽0.01	⩽0.01	⩽0.01	⩽0.01	⩽0.01	⩽0.01	⩽0.01	⩽0.01	⩽0.01	⩽0.01	⩽0.01
Fe	46.65	58.06	45.21	58.55	56.13	25.92	58.47	59.18	58.40	57.87	59.07	58.79
Co	0.03	0.32	0.94	0.10	0.09	0.31	0.05	⩽0.01	0.09	⩽0.01	0.03	0.02
Ni	10.22	0.84	⩽0.01	0.32	1.50	37.14	0.54	0.92	0.17	0.39	0.49	0.46
Cu	⩽0.01	⩽0.01	0.09	0.06	0.39	⩽0.01	0.02	0.02	0.07	0.03	0.05	0.17
Mn	⩽0.01	⩽0.01	⩽0.01	⩽0.01	⩽0.01	⩽0.01	⩽0.01	⩽0.01	⩽0.01	⩽0.01	0.02	⩽0.01
Mg	⩽0.01	⩽0.01	⩽0.01	⩽0.01	⩽0.01	⩽0.01	⩽0.01	⩽0.01	⩽0.01	⩽0.01	⩽0.01	⩽0.01
S	38.51	39.03	53.55	39.23	39.47	32.89	38.97	36.87	39.63	38.90	38.75	39.06
Total	95.71	98.27	99.82	98.26	97.61	96.29	98.05	97.01	98.39	97.21	98.46	98.53

P - Peridotitic
E - Eclogitic
W-Websteritic

Grt - Garnet
Cpx - Clinopyroxene
Ol - Olivine
Sul - Sulphide

Pyr. - Pyrite
Pyrhh. - Pyrrhotite
Pent. - Pentlandite
Mss - Monosulphide solid solution

or they contained secondary/epigenetic inclusions. Major- and minor-element data are listed in Table 3.2.

3.3.1. Syngenetic inclusions

Inclusions were classified as syngenetic based on cubo-octahedral morphologies and absence of fractures extending to the diamond surface. For one diamond, part of one garnet inclusion was exposed to the diamond surface before recovery (B2K4-1), thus it may have re-equilibrated during residence in the mantle or become metasomatized by the magma during kimberlite emplacement (Tappert et al., 2005). This garnet, however, shares a similar major- and minor-element chemistry with other garnets completely enclosed in the same diamond, and thus the analytical results are included here with syngenetic inclusions. The fragmentation leading to exposure of the garnet is likely attributable to the sampling process after emplacement (Chapter 3.2.4).

Olivine

Six colourless olivine inclusions were recovered from five diamonds. The Mg# of olivines ranges from 91.0 to 93.2 (Figure 3.3, Table 3.2). Two olivines occurring in the same diamond (B4WK2-1) are of harzburgitic paragenesis, as indicated by coexistence with a harzburgitic garnet. One olivine (from B5K2-10) has a high CaO concentration of 0.06 wt% and likely crystallized in equilibrium with clinopyroxene (Stachel and Harris, 2008); the Mg# of this olivine is low (91.0) consistent with a likely lherzolitic paragenesis. The remainders have low CaO contents (< 0.02 wt%), suggesting a harzburgitic assemblage (Stachel and Harris, 2008). Additionally, these olivines have relatively high Mg# (92.6-93.2) consistent with a derivation from harzburgitic sources.

Garnet

Six garnet inclusions were released from five diamonds. Of these, five garnets whose perceived colour is orange, are grossular rich and have Cr_2O_3 contents < 0.4 wt%, which is a typical value for 98 % of eclogitic garnets (Meyer, 1987). Applying the 6 wt% CaO cut-off between the high and low-Ca groups (Grütter et al., 2004), these garnets are categorized as G3 and G4. According to the classification scheme in Grütter et al. (2004), G3 garnets are assigned to the eclogitic suite (Figure 3.4). The one G4 garnet has no co-

existing inclusions, and 4.69 wt% CaO, 0.30 wt% Cr_2O_3, 0.03 wt% NaO, Mg# > 80.5. Garnet class G4 contains both low-Ca eclogitic and low-Cr websteritic (pyroxenitic) garnets. Eclogitic garnet inclusions are generally rich in Na_2O (Na_2O > 0.07 wt%; Sobolev and Lavrent'ev, 1971; McCandless and Gurney, 1989), and websteritic garnet inclusions have elevated Cr# with Cr_2O_3 > 0.4 wt% (Grütter et al., 2004; Stachel and Harris et al. 2008). Based on a Cr_2O_3 < 0.04 wt%, the G4 garnet is likely eclogitic, but an unequivocal classification is not possible (Grütter et al., 2004). For Chidliak eclogitic inclusions, a negative correlation between Na_2O and Mg# is observed (Figure 3.5). This documents the variably strong depletion of Na in the eclogitic bulk rock compositions (Grütter and Quadling, 1999).

The sixth garnet is a peridotitic garnet occurring together with two olivines, recovered from sample B4WK2-1. It has a purple colour and is a chrome pyrope in composition, with contents of 4.5 wt% CaO, 11.4 wt% Cr_2O_3, 20.9 wt% MgO and 6.3 wt% FeO. The concentration of TiO_2 is 0.04 wt%, which falls on the cut-off (0.04 wt%; Stachel and Harris, 2008) between high- and low-Ti garnets. The garnet plots in the harzburgitic field and classifies as G10. The Mg# of this garnet is 85.5, with the average for harzburgitic and lherzolitic garnet inclusions worldwide being 88.0 and 86.6, respectively (Stachel and Harris, 2008).

Clinopyroxene

Eight pale-green omphacitic clinopyroxenes were found in four diamonds. They have Mg# < 85, typical of eclogitic clinopyroxene (Stachel and Harris, 2008). All of the clinopyroxene inclusions have contents of Cr_2O_3 < 0.4 wt% and high Al_2O_3 ranging from 12.0 to 20.3 wt% (the highest value is close to the worldwide highest value of 21.3 wt%; Stachel and Harris, 2008). Their compositions (Table 3.2) indicate the presence of a jadeite component, and the excess of Al over Na in some diamonds suggests an additional Tschermaks component (Stachel and Harris, 2008). The Cr# of all clinopyroxenes are very low (the highest Cr# is 0.21) and far below the cut-off value (Cr# < 7) between eclogitic and peridotitic clinopyroxenes. From a diagram of Mg# versus molar Cr#, all clinopyroxene inclusions plot within the eclogitic field (Figure 3.6), and the relatively high Na and very low Cr also aid to suggest an eclogitic origin (Figure 3.7). Two of these

clinopyroxenes (from diamond N2K4-5) were recovered together with an eclogitic garnet, establishing their derivation from eclogitic sources.

Sulphides

Sulphides within diamonds are at the center of black fractures but are yellow after release from their hosts. Twelve sulphides (Table 3.2) were recovered from ten diamonds, and they are all are Fe-Ni sulphides, including pyrite, pyrrhotite, pentlandite and monosulphide solid solution (Figure 3.8). The ranges for eclogitic and peridotitic sulphides are Ni < 12 wt% and Ni of 22 to 36 wt%, respectively (Figure 3.9; Yefimova et al., 1983, Bulanova et al., 1996 and Stachel and Harris, 2008). Ten out of twelve sulphides are iron sulphides and have very low Ni concentrations and Cr contents below the detection limit, indicating an eclogitic paragenesis; one of the sulphides occurred with two rutiles, which further confirms an eclogitic origin. The remaining two sulphides are iron nickel sulphides, with 10.2 wt% and 37.1 wt% Ni, respectively: the high-Ni sulphide clearly reflects a peridotitic source composition, and the second sulphide with intermediate-Ni but with its high Cr content also likely belongs to the peridotitic paragenesis (Figure 3.9).

Kullerud et al. (1969) showed that in the Fe-Ni-S system, FeS monosulphide precipitates at about 1200 ℃ and Ni-S in the MSS increasing with decreasing temperature. Hence, after the entrapment of sulphide melts in diamond, differences in compositions among sulphide inclusions may reflect different exsolution and cooling stages (Harris, 1992).

Rutile

Two dark-red and well-shaped rutile inclusions occur in diamond B4WK2-2 and coexist with an iron sulphide inclusion. They have very low contents of minor elements (Table 3.2). Rutile is uncommon as an inclusion in diamond and typically a member of the eclogitic suite (Meyer, 1987).

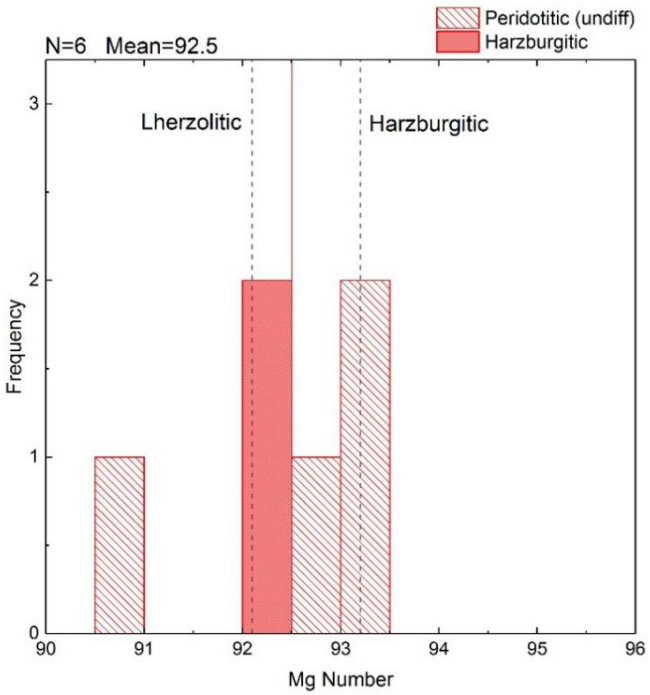

Figure 3.3. The Mg# of Chidliak olivine inclusions. The solid line indicates the mean composition (92.5). Two dashed lines represent the mean Mg# of lherzolitic (92.1) and harzburgitic (93.2) olivine inclusions worldwide (data from Stachel and Harris, 2008).

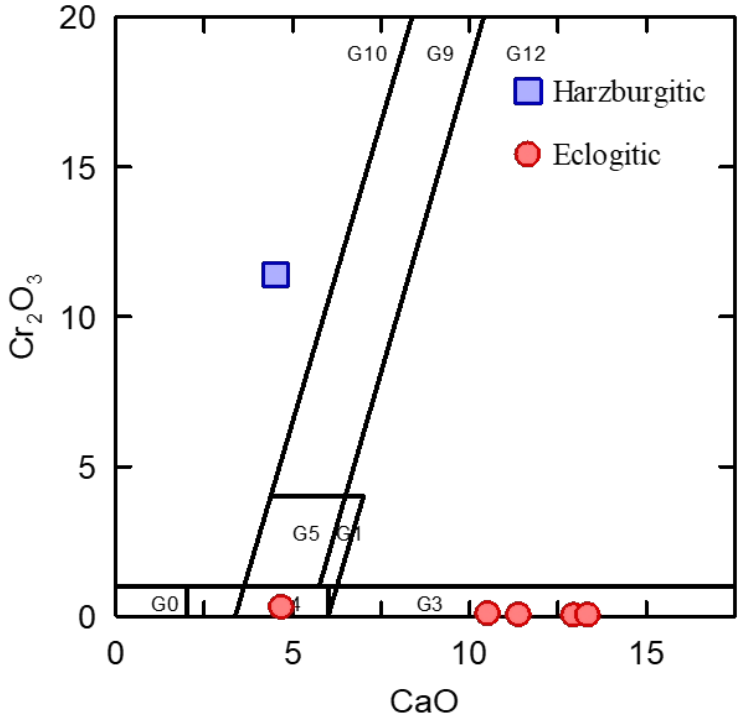

Figure 3.4. Cr-Ca plot for Chidliak garnet inclusions. Classification scheme is from Grütter et al. (2004).

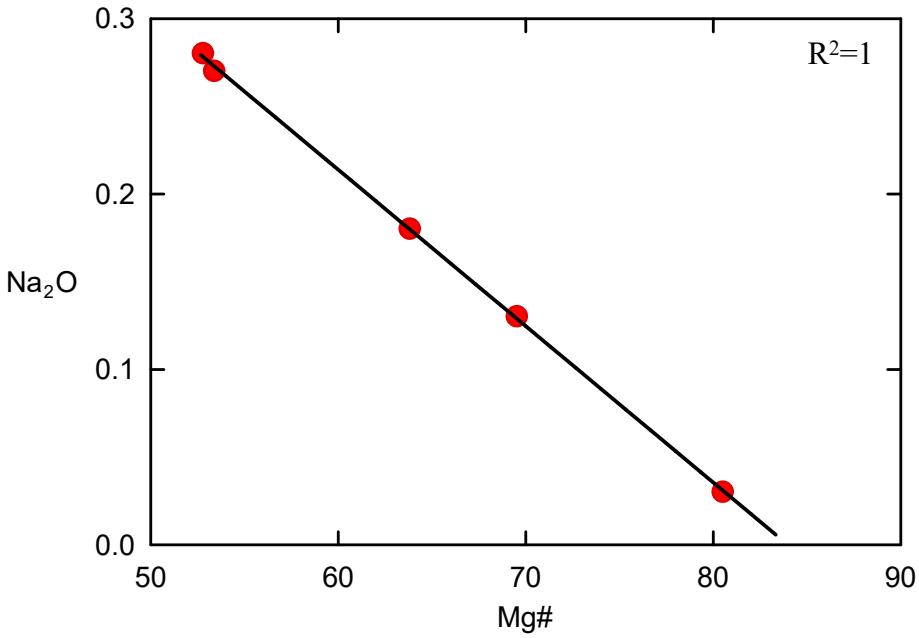

Figure 3.5. Na_2O versus Mg# for eclogitic garnet inclusions. A linear negative correlation is observable.

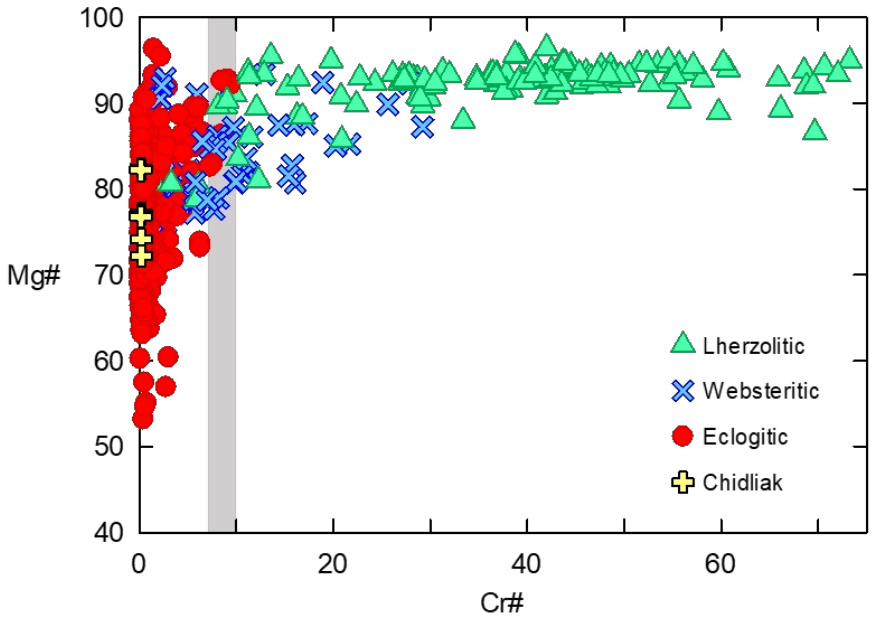

Figure 3.6. Mg# versus Cr# for clinopyroxene inclusions. The transition from P-type to E-type clinopyroxene inclusions occurs at the grey band (Cr#: 7-10; Stachel and Harris, 2008). Database is from Stachel and Harris (2008).

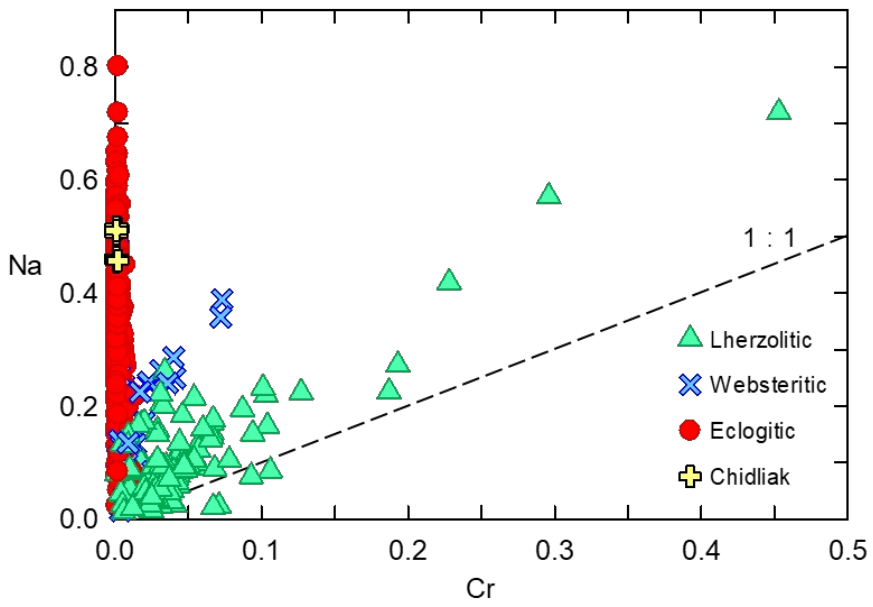

Figure 3.7. Na versus Cr (cations based on six oxygens per formula unit) for clinopyroxene inclusions. Database is from Stachel and Harris (2008).

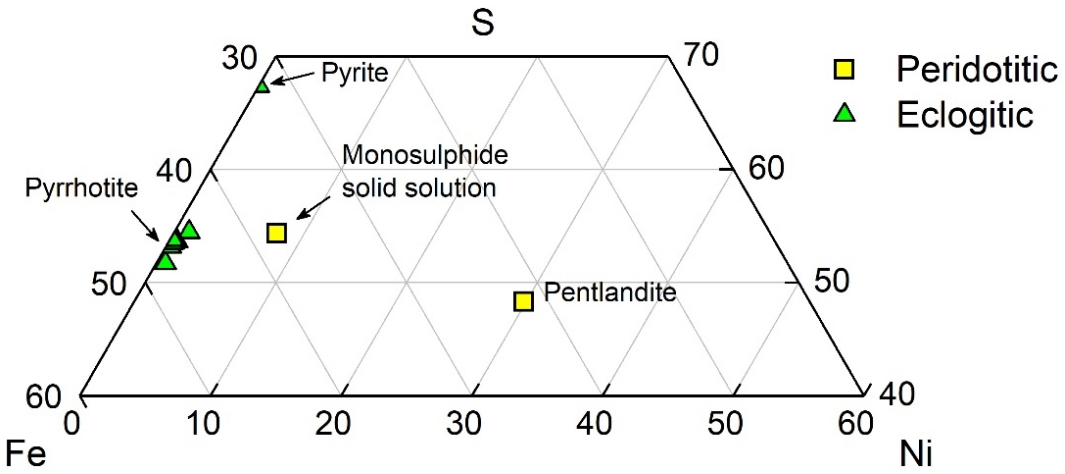

Figure 3.8. The composition of sulphide inclusions in the Fe-Ni-S quadrilateral (based on atomic proportions).

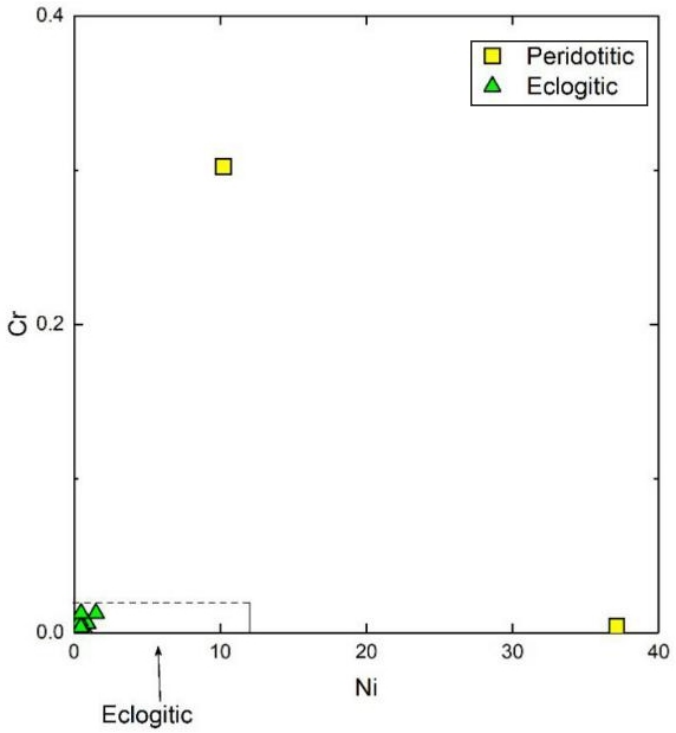

Figure 3.9. Cr versus Ni (wt%) for Chidliak sulphide inclusions. An eclogitic area is defined at Ni contents < 12 wt% (Bulanova et al., 1996) and Cr contents < 0.02 wt% (Stachel and Harris, 2008).

3.3.2. Epigenetic inclusions

The remaining 52 diamonds, after breakage, were found to be either inclusion-free, or to contain graphite, or soft whitish, greenish or orange materials of likely epigenetic origin. Several heterogeneous secondary minerals were also released. Such epigenetic minerals include mainly mixtures of sulphides, silicates (e.g., mainly serpentine-like), and potassium-bearing minerals (possibly altered mica) and are not considered further. Most of the epigenetic sulphides are composed mainly of Ni, Fe, Co and Mg, and have extremely high Ni contents > 50 wt%; however, due to the alteration, accurate compositions could not be obtained. A minor component among the secondary minerals are mixtures of hydrated aluminum sulphate minerals.

The highly altered sulphide inclusions have partially been replaced by silicates. The replacement of sulphides by silicates is a two-stage open system process due to the complete immiscibility of sulphide and carbonate-silicate melts in the upper mantle (Litvin

and Butvina, 2004; Hunt et al., 2008). The original sulphides were first partially removed by oxidizing melts/fluids passing through fractures into the diamond, and then the silicates were deposited and filled the cavity (Hunt et al., 2008). As the serpentine-like silicates are not stable in the diamond stability field, they likely precipitated at lower pressure/temperatures during or after kimberlite emplacement (Hunt et al., 2008).

3.3.3. Trace-Element Composition of Eclogitic Inclusions

Trace element analyses of a subset of eclogitic garnet and clinopyroxene inclusions were carried out using laser-ablation ICP-MS (Table 3.3). One spot per sample was analyzed because of the small size of inclusions (~ 100 to 200 μm). For plotting, the REE (rare earth element) contents are normalized (REE_N) to the C1-chorondrite composition after McDonough and Sun (1995).

The REE_N patterns of three high-Ca garnets (G3) show a steep positive $LREE_N$ trend and a flat $MREE_N$ and $HREE_N$. In comparison to the high-Ca garnets, the low-Ca garnet (G4; sample N2K4-2) has a similar positive $LREE_N$ slope, but this positive slope continues into the $HREE_N$, and thus, resulting in extremely low $LREE_N/HREE_N$ ($La_N/Lu_N = 0.001$; Figure 3.10).

For the high-Ca garnets, the $HREE_N$ concentrations (~ 2 to 4 times chondritic abundance) are considerably lower than the worldwide average, i.e., worldwide eclogitic garnet have average $HREE_N$ at ~ 30 times chondritic level (Stachel et al., 2004). For all garnets, a positive correlation between Sr content and LREE is observed. All high-Ca garnets have positive Eu anomalies.

The eclogitic clinopyroxene occurring with a garnet in diamond N2K4-5 has very low concentrations of $HREE_N$ compared to those from global locations (Stachel et al., 2004); The abundances of Yb and Lu are below the limit of detection. It has enriched $LREE_N$ relative to C1-chondrite with a positive slope peaking at Nd, followed by decreasing $MREE_N$ and $HREE_N$. Overall concentrations of REE_N in the clinopyroxene inclusion are considerably lower than the worldwide average: worldwide eclogitic clinopyroxene have average $LREE_N$ and $MREE_N$-$HREE_N$ at ~ 10 and ~ 1-4 times chondritic abundance,

respectively (Stachel et al., 2004). Like the garnet enclosed in the same stone, a distinct positive Eu anomaly (Eu/Eu* = 1.8) is present.

Table 3.3. Trace element compositions (ppm) for selected eclogitic garnet and clinopyroxene inclusions.

Sample	B2K4-1	B2K4-16	N2K4-2	N2K4-5a	N2K4-5b
Mineral	Grt	Grt	Grt	Grt	Cpx
Assembly	Grt	Grt	Grt	Grt, Cpx	Grt, Cpx
Paragenesis	E	E	E	E	E
Ti	4456	2332	1006.7	3387	2673
Sr	15.20	2.37	0.11	3.14	211.70
Y	7.40	6.22	35.68	6.25	0.18
Zr	33.95	4.97	20.67	5.86	1.69
Nb	0.03	0.37	0.15	0.37	0.44
Ba	0.00	<LOD	0.05	<LOD	0.03
La	0.12	0.02	0.02	0.03	0.30
Ce	1.21	0.27	0.21	0.32	1.29
Pr	0.63	0.11	0.09	0.12	0.23
Nd	6.68	1.04	0.86	1.25	1.15
Sm	2.12	0.65	0.57	0.74	0.22
Eu	1.23	0.48	0.24	0.55	0.11
Gd	1.69	0.94	1.19	1.18	0.15
Tb	0.24	0.19	0.35	0.21	0.01
Dy	1.41	1.23	4.09	1.27	0.06
Ho	0.27	0.27	1.34	0.25	0.01
Er	0.80	0.70	5.48	0.68	0.01
Yb	0.77	0.60	8.11	0.58	<LOD
Lu	0.11	0.08	1.40	0.09	<LOD
Hf	0.72	0.17	0.42	0.20	0.17

Unit is (ppm)
LOD - Limit of detection
E - Eclogitic
Grt - Garnet
Cpx - Clinopyroxene

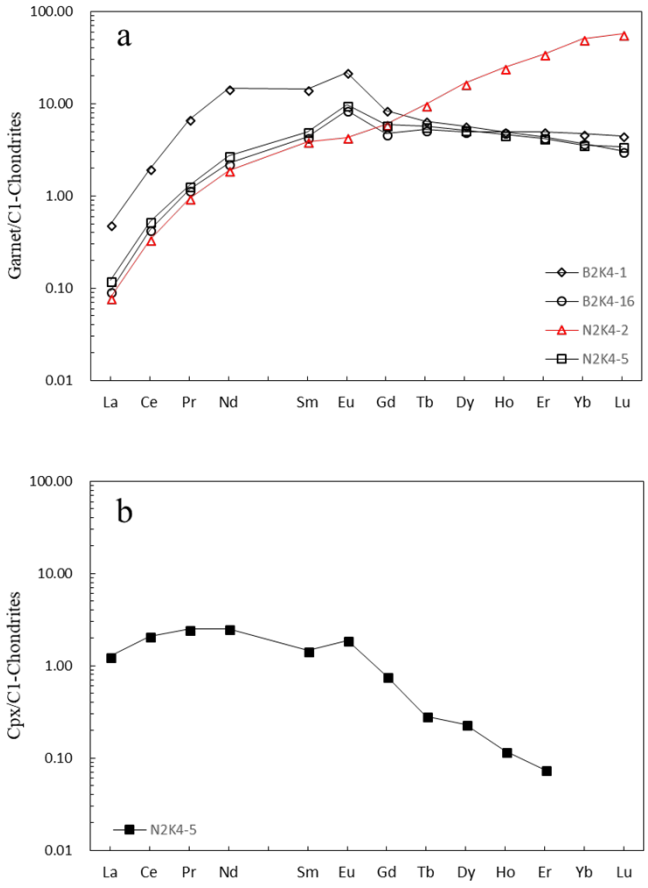

Figure 3.10. REE concentrations of (a) eclogitic garnet and (b) clinopyroxene inclusions. Low-Ca garnet N2K4-2 is highlighted in red. Compositions are normalized to C1-chondrite (McDonough and Sun; 1995).

3.4. Nitrogen Content and Aggregation State

Nitrogen is the most abundant impurity in diamond. It substitutes for carbon atoms in the diamond lattice due to similar ionic radius and valence (Cartigny, 2005). Nitrogen concentrations in diamonds can range from below the detection limit (at ~ 10 at. ppm) to 5500 at. ppm (Sellschop et al., 1979), but are normally lower than 1400 at. ppm, with a median value of 160 at. ppm. Eclogitic diamonds typically contain higher nitrogen (median: 484 at. ppm) than peridotitic stones (median: 82 at. ppm; Stachel, 2014).

Diamonds can be classified as Type I (nitrogen-bearing) and Type II (nitrogen lower than the detection limit; Harris, 1987). On the basis of different nitrogen-bearing centers, Type

I diamonds can be categorized as Type Ib (single substitutional nitrogen) and Type Ia (aggregated nitrogen; Evans and Qi, 1982). Type Ia is subdivided into Type IaA (> 90 % of nitrogen occurring as pairs called A-centers), Type IaAB (10-90 % A centers) and Type IaB (> 90 % of nitrogen occurring as N_4V aggregates called B centers; Davies, 1976; Evans et al., 1981). Nitrogen aggregation states are associated with total nitrogen contents and the temperature and residence time in mantle (Harris, 1987): single substitutional nitrogen atoms (C centers) rapidly aggregated into A centers at mantle temperature, and then gradually into B centers, which generally takes hundreds of millions to billions of years (Evans, 1992).

Fragments of Chidliak diamonds from inclusion release, were selected to quantify nitrogen abundance and characterize nitrogen aggregation states using Fourier-transform infrared spectroscopy (FTIR). The nitrogen contents show a range from 7 at. ppm (lower than the typical limit of detection of ~ 10 at. ppm) to 2443 at. ppm, with an average value of 499 at. ppm and a median value of 336 at. ppm (Table 3.4). The aggregation levels vary from 0 to 51 %B (=100*B/(A+B)), and therefore, no Type IaB diamonds are present. Except for one sample (B1K5-1), at least two spots per diamonds were analyzed, in case of variations in nitrogen abundance and aggregation state for each diamond. The variation in nitrogen content within single diamonds is generally around 50 at. ppm; it can, however, be as high as about 460 at. ppm in one sample (N5K2-7). The nitrogen concentrations of diamonds from SIMS in Hogberg et al. (2016) have a spread from < 1 to 3833 at. ppm and the median value is 1112 at. ppm, with diamonds from CH-6 and CH-7 having a median value of 1260 at. ppm and 1092 at. ppm, respectively.

One diamond (1 %; B3K3-3) containing both nitrogen in single substitution (C centers) and A centers is categorized as Ib-IaA. The majority of Chidliak stones (51 %) are assigned as Type IaA (one diamond with nitrogen below detection of ~ 10 at. ppm classifies as a low-N Type IaA), while Type IaAB comprise 44 % in the sample set. The remaining 4 % of stones show mixed aggregation states (one spot is Type IaA and the other spot is Type IaAB). The lack of Type II diamonds is unexpected, considering that worldwide 19 % of inclusion-bearing lithospheric diamonds are Type II (16 % of eclogitic and 84 % of peridotitic diamonds; Stachel, 2014) and that the previous study of Nichols (2014; MSc

thesis) found 9.4 % of Type II diamonds (non-included) at Chidliak. However, diamonds in Nichols (2014; MSc thesis) are only from phase K1, while diamonds examined here are from other phases. It may explain the absence of Type II diamonds in this study.

3.4.1. Platelet Peak

Platelets form during the aggregation of nitrogen into B centers (Sobolev et al., 1968). They are planar defects in the crystal lattice and are recognized as an absorbance peak at 1358-1378 cm^{-1} (Sobolev et al., 1968). The composition of platelets is now considered to be an assemblage of interstitial carbon atoms instead of interstitial nitrogen atoms (Woods, 1986; Goss, et al., 2003; Howell et al., 2012). Woods (1986) recognized a linear relationship of the platelet peak area and the N content in B centers that allows distinction of 'regular' (show a linear relationship) from 'irregular' diamonds (falling below this line). Short-lived thermal events (Evans et al. 1995) and deformation (Woods, 1986) may cause catastrophic platelet degradation, giving rise to 'irregular' types. Howell et al. (2012) observed a reduced rate of platelet formation in cuboid growth sectors and, therefore, the linear relationship between N in B centers and the platelet peak area can only be applied to non-cuboid diamonds. CL images can be used to identify cuboid growth sectors, but only fragments of 22 diamonds for SIMS analysis were polished and imaged in random orientation (with potential cuboid sectors are possibly not being exposed). Cuboid diamonds or growth sectors are, however, associated with elevated hydrogen contents, reflected by a peak area of the hydrogen related absorption peak at 3107 cm^{-1} of ≥ 20 cm^{-2} (Howell et al., 2002). The only diamond with 3107 cm^{-1} peak area ≥ 20 cm^{-2} is a pure Type IaA diamond. All pure Type IaA (all spots with %B < 2 %) diamonds (16 stones; 22 %) were excluded from the platelet degradation calculations, as such diamonds either have no platelet peak or only very minor platelet related absorption.

For Chidliak samples, 50 diamonds (68 %) contain measurable platelet defects, with nine of these diamonds having only one spot presenting the peak, and with the colourless core of one yellow-coated stone exhibiting a platelet peak and the yellow coat not exhibiting a platelet peak. For pure Type IaA diamonds without B centers (both spots have %B < 2 %), only five out of sixteen samples present a small platelet peak in at least one spot. Almost all samples from Chidliak plot below the regular trend and classify as "irregular" diamonds

Table 3.4. FTIR data for Chidliak diamonds. Time-averaged mantle residence temperatures are calculated after Leahy and Taylor (1997). For pure Type IaA diamonds, 0.5 %B was assumed for calculation of a maximum mantle residence temperature.

Sample ID	Spot#	Type	Total N (at. ppm)	%B	TN [3Ga]	TN [2Ga]	TN [1Ga]	Platelet Peak Area (cm^{-2})	3107 Peak Area (cm^{-2})
B1K5-1	1	IaAB	73.8	41.3	1168	1178	1196	0.75	0.78
B1K5-2	1	IaA	75.7	0.0	1051	1060	1075	3.12	1.03
B1K5-2	2	IaA	110.4	9.4	1111	1120	1137	3.18	1.04
B1K5-3	1	IaAB	1128.9	35.2	1095	1104	1121	32.53	1.40
B1K5-3	2	IaAB	1132.8	36.7	1097	1106	1122	35.34	1.18
B1K5-4	1	IaA	79.8	0.0	1050	1059	1074	1.49	1.20
B1K5-4	2	IaA	37.7	0.0	1066	1075	1091		2.29
B1K5-5	1	IaAB	338.1	50.8	1139	1149	1167	18.00	1.24
B1K5-5	2	IaAB	323.4	36.3	1126	1136	1153	21.78	0.81
B1K5-5	3	IaAB	379.4	44.5	1130	1140	1157	22.48	0.73
B1K5-6	1	IaA	1175.3	1.4	1015	1024	1038		11.50
B1K5-6	2	IaA	1131.1	0.0	995	1003	1017		51.44
B1K5-7	1	IaAB	846.2	19.7	1084	1093	1109	9.32	6.99
B1K5-7	2	IaAB	879.7	19.7	1083	1092	1108	8.86	4.28
B1K5-8	1	IaA	333.7	0.0	1020	1028	1043	3.82	0.72
B1K5-8	2	IaA	333.7	0.2	1002	1010	1024	5.06	0.89
B2K4-1	1	IaAB	897.4	20.2	1083	1092	1108	18.78	0.81
B2K4-1	2	IaAB	872.4	20.9	1084	1094	1110	16.25	0.60
B2K4-2	1	IaAB	603.7	15.5	1085	1094	1110	7.88	1.01
B2K4-2	2	IaAB	570.3	13.4	1082	1091	1107	8.03	1.21
B2K4-3	1	IaAB	420.3	46.1	1129	1139	1156	27.56	2.95
B2K4-3	2	IaAB	377.4	42.7	1128	1138	1156	23.30	2.70
B2K4-4	1	IaA	15.6	0.0	1086	1095	1111		0.71
B2K4-4	2	IaA	24.6	0.0	1076	1085	1101		0.67
B2K4-5	1	IaA	365	2.8	1055	1064	1079	3.83	0.56
B2K4-5	2	IaAB	356.8	10.9	1087	1097	1113	6.69	0.54
B2K4-6	1	IaA	104.5	3.6	1088	1098	1114	1.38	0.94
B2K4-6	2	IaA	54.7	3.7	1104	1113	1130	0.76	0.71
B2K4-7	1	IaA	25.5	0.0	1075	1084	1100		0.60
B2K4-7	2	IaA	31.6	0.0	1070	1079	1095		0.34
B2K4-7	3	IaA	35	5.1	1123	1132	1149		0.61
B2K4-8	1	IaAB	831.5	16.9	1080	1089	1105	16.23	1.11
B2K4-8	2	IaAB	782	12.0	1072	1081	1097	16.35	1.13
B2K4-9	1	IaA	217.9	10.0	1096	1106	1122		2.94
B2K4-9	2	IaA	221.8	7.9	1090	1099	1116		3.11
B2K4-10	1	IaAB	428.9	28.9	1111	1121	1137	21.37	
B2K4-10	2	IaAB	496.7	35.8	1115	1125	1141	24.19	0.12
B2K4-11	1	IaAB	516.8	17.9	1092	1101	1118	5.54	1.76
B2K4-11	2	IaA	519.5	6.0	1064	1073	1089	7.32	1.67
B2K4-12	1	IaA	348.5	7.0	1077	1086	1102	2.21	0.35
B2K4-12	2	IaA	334.2	0.0	1020	1028	1043	2.22	0.40
B2K4-13	1	IaA	202.6	1.2	1048	1057	1072	0.90	0.08
B2K4-13	2	IaA	221.3	3.0	1067	1076	1092	1.11	0.11
B2K4-14	1	IaAB	519.8	19.9	1095	1104	1121	7.43	0.62
B2K4-14	2	IaAB	994.2	18.3	1078	1087	1103	17.92	1.04
B2K4-15	1	IaAB	552.4	10.2	1076	1085	1101	6.78	2.41
B2K4-15	2	IaAB	560.1	17.4	1089	1099	1115	7.07	2.09

Table 3.4. Cont.

Sample ID	Spot#	Type	Total N (at. ppm)	%B	TN [3Ga]	TN [2Ga]	TN [1Ga]	Platelet Peak Area (cm^{-2})	3107 Peak Area (cm^{-2})
B2K4-16	1	IaA	40.4	0.0	1065	1074	1089		0.11
B2K4-16	2	IaA	40.2	0.0	1065	1074	1089		0.08
B2K4-17	1	IaAB	174.9	13.0	1108	1118	1135		2.67
B2K4-17	2	IaAB	142.7	27.4	1136	1146	1163	1.10	3.09
B2K4-18	1	IaAB	1478	34.9	1089	1098	1114	33.63	6.63
B2K4-18	2	IaAB	1730.7	41.1	1091	1100	1117	25.53	9.64
B3K3-1	1	IaAB	434.2	21.7	1102	1111	1128	14.12	0.35
B3K3-1	2	IaAB	448.6	25.9	1106	1116	1133	12.70	0.33
B3K3-2	1	IaAB	25.6	22.3	1172	1182	1201		0.15
B3K3-2	2	IaA	16.3	0.0	1085	1094	1110		0.21
B3K3-3	1	Ib-IaA	978.7	7.4	1055	1064	1080		6.13
B3K3-3	2	Ib-IaA	997.6	7.6	1056	1064	1080		6.33
B3K3-4	1	IaAB	344.3	40.2	1128	1138	1155	3.46	0.63
B3K3-4	2	IaAB	362.9	31.4	1118	1127	1144	4.51	0.80
B4WK2-1	1	IaA	181	5.0	1084	1093	1109	8.13	2.34
B4WK2-1	2	IaA	152	9.0	1102	1112	1128	8.25	5.11
B4WK2-2	1	IaA	157.6	0.0	1035	1044	1059		0.19
B4WK2-2	2	IaA	186.1	0.0	1032	1040	1055		0.15
B4WK2-3	1	IaAB	708.1	13.4	1077	1086	1102	10.29	0.89
B4WK2-3	2	IaAB	728.4	13.4	1076	1086	1102	12.21	0.84
B4WK2-4	1	IaAB	83.9	12.9	1126	1136	1153		0.40
B4WK2-4	2	IaAB	76.3	35.6	1161	1171	1189		0.36
B4WK2-5	1	IaAB	290.1	34.2	1126	1136	1153	11.16	1.49
B4WK2-5	2	IaAB	203.1	32.3	1133	1143	1160	9.17	1.85
B4WK2-6	1	IaAB	1812	13.0	1056	1065	1080		4.70
B4WK2-6	2	IaAB	1833.7	18.0	1064	1073	1088		4.67
B4WK2-7	1	IaA	1684.8	0.4	983	991	1004		3.20
B4WK2-7	2	IaA	1464.4	0.7	996	1004	1018		3.64
B4WK2-8	1	IaAB	733.7	20.1	1087	1097	1113	8.56	22.41
B4WK2-8	2	IaAB	651.7	26.0	1098	1107	1124	6.18	14.42
B4WK2-9	1	IaA	891.2	4.9	1048	1057	1072	4.94	5.81
B4WK2-9	2	IaA	941.2	3.9	1042	1050	1065	6.31	6.15
B4WK2-10	1	IaA	404.8	6.4	1071	1080	1096	2.51	0.36
B4WK2-10	2	IaA	574.9	2.0	1037	1046	1061	4.68	0.38
B4WK2-11	1	IaA	904.2	4.3	1045	1053	1068		2.19
B4WK2-11	2	IaA	878.8	0.0	1000	1008	1022	1.53	0.18
B4WK2-12	1	IaAB	679.8	11.3	1074	1083	1099	7.83	0.15
B4WK2-12	2	IaAB	621.3	10.9	1075	1084	1100	7.35	0.12
B5K2-1	1	IaA	890.8	0.0	1000	1008	1022		10.10
B5K2-1	2	IaA	997.2	2.5	1031	1039	1054		12.00
B5K2-2	1	IaA	294.4	6.4	1078	1088	1104	1.76	0.20
B5K2-2	2	IaA	287.5	2.9	1060	1069	1085	1.84	0.39
B5K2-3	1	IaAB	123.7	32.9	1146	1156	1173	1.62	2.88
B5K2-3	2	IaAB	114.1	14.5	1122	1131	1149	0.92	2.13
B5K2-4	1	IaA	222.5	7.4	1088	1098	1114	1.20	0.73
B5K2-4	2	IaA	160.5	7.8	1097	1107	1123	0.94	0.54
B5K2-5	1	IaAB	142.8	20.1	1126	1136	1153	4.65	0.50
B5K2-5	2	IaAB	125.9	17.6	1125	1135	1152	3.83	0.81
B5K2-6	1	IaAB	953.6	20.9	1082	1092	1108	15.28	5.98
B5K2-6	2	IaAB	1035.2	19.8	1079	1088	1104	15.43	13.05
B5K2-7	1	IaAB	1319.9	22.3	1077	1086	1102	18.68	0.36

Table 3.4. Cont.

Sample ID	Spot#	Type	Total N (at. ppm)	%B	TN [3Ga]	TN [2Ga]	TN [1Ga]	Platelet Peak Area (cm^{-2})	3107 Peak Area (cm^{-2})
B5K2-7	2	IaAB	1192.8	20.2	1076	1086	1101	18.46	0.73
B5K2-8	1	IaAB	510	45.5	1124	1134	1151		4.43
B5K2-8	2	IaAB	522.6	50.7	1128	1138	1155		4.70
B5K2-9	1	IaA	39.8	0.0	1065	1074	1090	0.62	0.52
B5K2-9	2	IaA	43.8	0.0	1063	1072	1087		0.92
B5K2-10	1	II	6.8	0.0	1105	1115	1131		0.75
B5K2-10	2	II	9.8	0.0	1097	1106	1122		1.33
B5K2-11	1	IaA	1822.4	2.0	1014	1022	1037		9.92
B5K2-11	2	IaA	1906.8	0.0	985	993	1006		10.44
B5K2-12	1	IaAB	85.3	36.5	1159	1169	1187	0.92	1.27
B5K2-12	2	IaAB	59.6	23.7	1152	1162	1180	1.36	0.37
B5K2-13	1	IaAB	36	13.1	1147	1157	1175		2.22
B5K2-13	2	IaAB	34.3	17.8	1157	1167	1185		2.27
N1K5-1	1	IaA	44.9	0.0	1062	1071	1087		0.68
N1K5-1	2	IaA	64.5	3.1	1096	1105	1122		0.45
N1K5-2	1	IaA	175.9	0.1	989	997	1011		
N1K5-2	2	IaA	167.1	0.0	1034	1043	1058	1.38	
N1K5-3	1	IaA	993.7	0.4	991	999	1013		1.05
N1K5-3	2	IaA	1001.1	0.0	997	1005	1020		1.09
N2K4-1	1	IaA	101.2	0.0	1045	1053	1069		4.14
N2K4-1	2	IaA	105.7	7.9	1107	1117	1134	0.52	3.96
N2K4-2	1	IaA	222.6	4.9	1078	1087	1103		15.44
N2K4-2	2	IaA	128.5	2.1	1071	1080	1096	2.17	7.73
N2K4-3	1	IaA	79.9	4.9	1102	1111	1128		1.20
N2K4-3	2	IaA	77.6	0.0	1050	1059	1074		1.16
N2K4-4	1	IaAB	84	16.9	1133	1143	1161	2.18	0.95
N2K4-4	2	IaAB	48.2	14.7	1143	1153	1171	0.84	0.35
N2K4-5	1	IaA	223.1	6.4	1085	1094	1110		
N2K4-5	2	IaA	217.9	7.2	1088	1097	1114		
N2K4-6	1	IaA	18.3	0.0	1082	1091	1108		0.17
N2K4-6	2	IaA	16.7	0.0	1084	1094	1110		0.17
N2K4-7	1	IaA	207.6	0.0	1029	1038	1053		0.42
N2K4-7	2	IaA	182.7	0.0	1032	1041	1056		0.11
N2K4-8	1	IaAB	629.3	14.1	1081	1090	1106	12.93	0.38
N2K4-8	2	IaAB	563.2	13.5	1082	1092	1108	11.94	0.33
N3K3-1-colorless	1	IaAB	2299.8	27.1	1070	1079	1095	11.00	4.31
N3K3-1-colorless	2	IaAB	2443.2	19.3	1059	1068	1084	12.74	8.05
N3K3-1-yellow coat	3	IaAB	1472.7	13.1	1060	1069	1085		3.04
N5K2-1	1	IaA	288.5	4.1	1069	1078	1093	1.74	0.19
N5K2-1	2	IaA	297.3	1.8	1049	1058	1074	2.01	0.17
N5K2-2	1	IaA	441.6	0.0	1014	1022	1037	4.56	0.80
N5K2-2	2	IaA	403.2	2.7	1051	1060	1076	3.39	0.78
N5K2-3	1	IaA	578	0.0	1008	1017	1031		1.81
N5K2-3	2	IaA	509.2	0.0	1011	1019	1034	2.06	0.50
N5K2-4	1	IaA	43.2	5.6	1119	1129	1146		1.29
N5K2-4	2	IaA	39.6	0.0	1065	1074	1090		1.38
N5K2-5	1	IaA	108.5	0.0	1043	1052	1067		0.39
N5K2-5	2	IaA	107.5	0.0	1043	1052	1067	0.79	0.50
N5K2-6	1	IaAB	370.4	14.5	1094	1103	1120	3.59	1.43
N5K2-6	2	IaAB	331.9	15.8	1099	1108	1125	2.31	1.32

Table 3.4. Cont.

Sample ID	Spot#	Type	Total N (at. ppm)	%B	TN [3Ga]	TN [2Ga]	TN [1Ga]	Platelet Peak Area (cm^{-2})	3107 Peak Area (cm^{-2})
N5K2-7	1	IaA	708.6	5.9	1057	1066	1081	11.61	0.19
N5K2-7	2	IaAB	1166.9	14.1	1067	1076	1092	20.75	0.39

(Figure 3.11). These "irregular" diamonds suffered "catastrophic platelet degradation" due to transient thermal events (Evans et al. 1995) and/or strain (Woods, 1986).

3.4.2. Hydrogen Peak

In the IR absorbance spectrum, hydrogen impurities result in a series of absorption peaks. The intensity of the main peak at 3107 cm^{-1} was measured, and one or more other weaker peaks at 3237 cm^{-1}, 2786 cm^{-1}, and 1404 cm^{-1} were noted in the majority of Chidliak diamonds. The peaks at 3107 cm^{-1}, 2786 cm^{-1} and 1404 cm^{-1} are attributed to the bending and stretching of carbon-hydrogen bonds (the vinylidene group: $C=CH_2$; Charette, 1959; Chrenko et al., 1967; Woods and Collins, 1983). Using first principle simulations, Goss et al. (2014) suggested that the 3107 cm^{-1} absorption peak results from a VN_3H defect (three nitrogen surrounding a vacancy decorated by a hydrogen).

The hydrogen related peaks were observed in seventy-two diamonds with one sample having peaks present in only one spot. The remaining two diamonds have no measurable hydrogen peaks. The hydrogen peak area varied from 0 to 54 cm^{-2}, with the majority of stones (93 %) falling between 0 and 10 cm^{-2}. There is no linear relationship between the 3107 cm^{-1} hydrogen peak intensity and the total nitrogen abundance (Figure 3.12). Such a relationship had previously been reported by Iakoubovskii and Adriaenssens (2002), who suggested that diamonds with low hydrogen and high nitrogen grew from a source rich in N_2, while more hydrogen-rich samples relate to ammonium/ammonia-bearing fluids.

3.4.3. Other Absorbance Peaks

A portion of Chidliak diamonds display spectral peaks at ~ 2920 cm^{-1}, ~ 2850 cm^{-1}, and ~ 1010 cm^{-1}; additional peaks at 3085 cm^{-1}, ~ 1550 cm^{-1}, ~ 1525 cm^{-1}, 1462 cm^{-1}, 1344 cm^{-1}, 1096 cm^{-1}, and ~ 875 cm^{-1} were also identified. The peaks between 2700 cm^{-1} and

3100 cm^{-1}, at 1550 cm^{-1}, and at 1525 cm^{-1} can be related to hydrogen impurities: the peak at 2920 cm^{-1} is caused by asymmetric stretching of sp3 bonded CH_3^- groups and absorbance at ~ 2850 cm^{-1} results from symmetric stretching of sp3 bonded CH_2^{2-} (Titus et al., 2005). The peak at 1462 cm^{-1} may be linked to a H-C-H bending mode of the CH_2^{2-} group (Janssen et al., 1991). In addition, peaks at 1096 cm^{-1} and ~ 1010 cm^{-1} possibly relate to mineral inclusions of submicroscopic size (Weiss et al., 2009, 2010) or nitrogen B centers (Iakoubovskii and Adriaenssens, 2002; Thongnopkun and Ekgasit, 2005), and a peak at 875 cm^{-1} is likely attributed to carbonate (Chrenko et al., 1967).

3.4.4. Mantle Residence History

The precise mantle residence time is unknown for Chidliak diamonds. Based on the Jurassic Kimberlite magmatism (157~ 139.1 Ma in Heaman et al., 2015) and typical Proterozoic formation ages for eclogitic diamonds, a mantle residence time of 1 Ga has been assumed for Chidliak diamonds.

Residence temperatures for 1-3 Ga residence time are given in Table 3.4. Even for a longer residence time of 3 Ga, the calculated temperature would only change by about 30 ℃ relative to 1 Ga, as mantle residence temperatures are quite insensitive to residence time (Evans and Harris, 1989). For unaggregated Type IaA diamonds (with 0 %B center), according to Leahy and Taylor (1997), 0.5 %B was assumed to calculate the temperature (following Leahy and Taylor, 1997), which represents a maximum mantle residence temperature.

Typically two spots were analyzed per stone and the within-sample difference in residence temperature for 80 % of diamonds is lower than 30 ℃ but can be as high as 90 ℃ in one sample. For Chidliak diamonds, the nitrogen-based time-averaged residence temperature range from ~ 1000 to 1200 ℃ (one spot of B3K3-2 gives the temperature of 1201 ℃) and 73 % of samples fall between 1050 and 1150 ℃ (Figure 3.13; Figure 3.14). Type IaA diamonds resided at ~ 1000 to 1150 ℃, while type IaAB diamonds give temperatures of ~ 1080-1200 ℃.

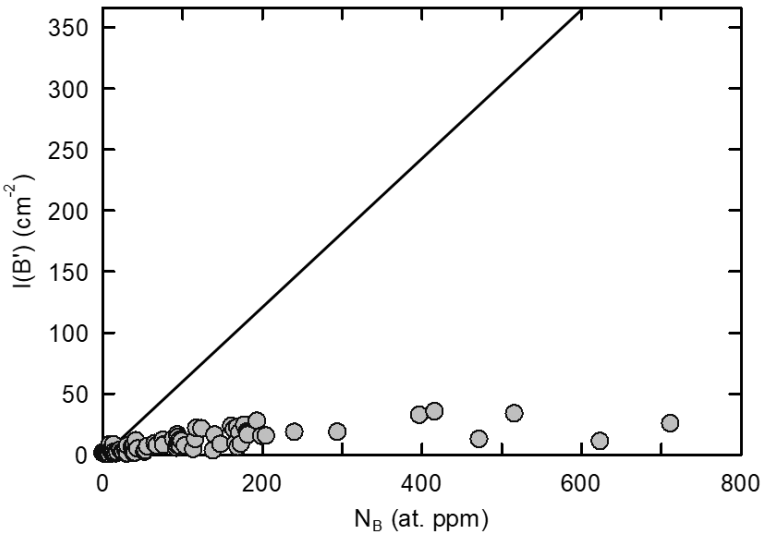

Figure 3.11. Platelet peak intensities (I(B')) versus nitrogen in B centers for Chidliak diamonds. The solid line indicates the linear relationship between plate peak area and nitrogen abundance in B aggregates (after Woods, 1986). All pure Type IaA (all spots with %B < 2) diamonds (16 stones; 22 %) were excluded.

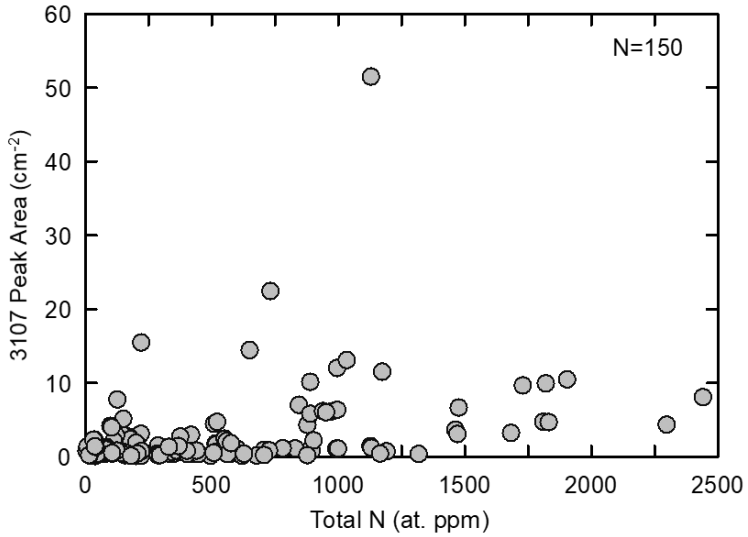

Figure 3.12. 3107 cm^{-1} hydrogen peak area versus the total nitrogen concentration for Chidliak diamonds. N=150 indicates the number of analysed spots.

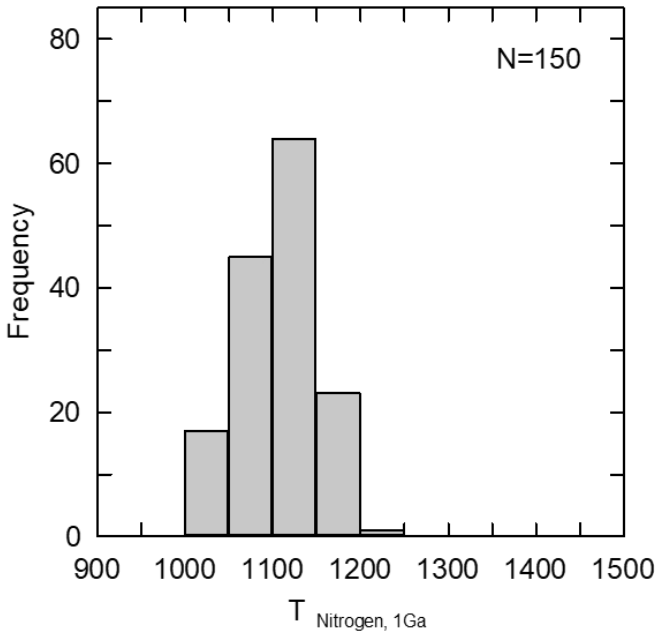

Figure 3.13. Frequency of time averaged mantle residence temperatures ($T_{Nitrogen}$) for Chidliak diamonds. Temperatures are calculated after Taylor et al. (1990) and Leahy and Taylor (1997) for a mantle residence time of 1 Ga. N=150 indicates the number of analyzed spots. An aggregation state of 0.5 %B was assumed for pure Type Ia samples (0 %B center).

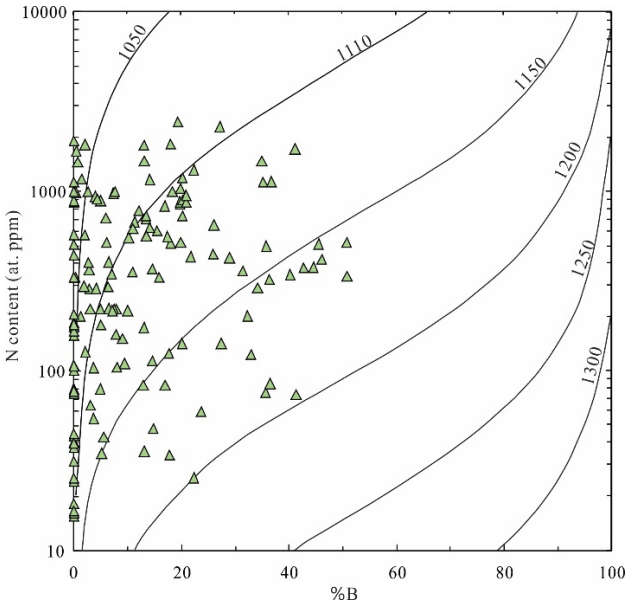

Figure 3.14. Time averaged mantle residence temperatures for 150 analytical spots on 74 diamonds from Chidliak. Isotherms for 1 Ga mantle residence time were calculated after Taylor et al. (1990) and Leahy and Taylor (1997). An aggregation state of 0.5 %B was assumed for pure Type Ia samples (0 %B center). %B expresses the nitrogen aggregation as percentage of nitrogen in the B center.

3.5. SIMS

A subset of 22 diamonds (117 points analyses) were analyzed for carbon and nitrogen isotope compositions and nitrogen abundances by SIMS.

3.5.1. Carbon Isotopic Composition

The carbon isotope composition in diamonds worldwide varies from -41 to +5 ‰ (Cartigny, 2005; De Stefano et al., 2009). Both peridotitic and eclogitic diamonds share a common mode in $\delta^{13}C_{VPDB}$ at -5 ± 1 ‰ (which also is the mantle value; Deines, 1980 and 2002; Cartigny, 2005). Diamonds deriving from eclogitic sources, however, span a wider range from -41 to +5 ‰ than those of the peridotitic suite, which normally fall between -10 to 0 ‰ (Kirkley et al., 1991; Cartigny, 2005; Stachel et al., 2009).

Chidliak diamonds have a spread in $\delta^{13}C$ from -25 to -1.6 ‰, which is consistent with the dominance of ecologic inclusions and also compares well with Hogberg et al. (2016) in which diamonds from CH-7 have $\delta^{13}C$ values ranging from -23.7 to -1.1 ‰ with a mode at -5.8 ‰. $\delta^{13}C$ of diamonds with peridotitic inclusions ranges from -5.8 to -1.6 ‰, with a mean of -3.5 ‰ which is close to the mantle value. Diamonds with eclogitic inclusions encompass a much broader range from -24.8 to -3.2 ‰. Eclogitic diamonds have a bimodal distribution: a primary mode in class bin -5 to -4 ‰ and a secondary mode in class bin -17 to -16 ‰ (Table 3.5 and Figure 3.15). Two to ten points were analyzed per sample and not averaged. In this subset of samples, no correlation between $\delta^{13}C$ values and physical characteristics (e.g., morphology), was observed.

3.5.2. Nitrogen Concentrations and Isotopic Composition

Nitrogen contents of the 22 diamonds have a range of 1 to 2468 at. ppm, with a median of 158 at. ppm (Table 3.5). This range coincides with that from FTIR (7 at. ppm to 2443 at. ppm), but the median value is lower than the FTIR data (336 at. ppm). Averaged FTIR bulk measurements from the same diamond differ by up to 628 at. ppm (Figure 3.16). This difference reflects the vast difference in sampled volume during FTIR (transmission of a 100 x 100 μm beam through sample) and SIMS analysis (15 x 15 μm beam size with < 1 μm sputtering depth). The variations of nitrogen contents within individual sample can reach up to 2448 at. ppm, but 65 % of diamonds vary less than 247 at. ppm.

Table 3.5. SIMS data for Chidliak diamonds

Sample	Spot	$\delta^{13}C$ (‰) (VPDB)	2σ error (‰)	N (at. ppm)	2σ error (ppm)	$\delta^{15}N$ (AIR)	2σ error (‰)
B2K4-1	S5129@1	-5.80	0.14	1101.0	11.4	-3.04	0.66
B2K4-1	S5129@2	-5.58	0.13	1062.1	11.0	-3.39	0.71
B2K4-1	S5129@3	-5.57	0.12	1059.5	11.2	-3.52	0.67
B2K4-6	S5130@1	-4.23	0.13	74.3	1.1		
B2K4-6	S5130@2	-4.21	0.13	115.4	1.5	-6.04	2.02
B2K4-6	S5130@3	-4.13	0.14	131.9	2.1	-6.85	2.16
B2K4-8	S5131@1	-3.71	0.13	902.7	9.4	-2.57	0.80
B2K4-8	S5131@2	-3.84	0.12	938.9	10.7	-0.91	0.82
B2K4-8	S5131@3	-4.67	0.14	389.6	6.1		
B2K4-8	S5131@4	-4.59	0.13	929.5	9.8	-3.02	0.75
B2K4-8	S5131@5	-3.16	0.13	796.4	8.6	-0.20	0.75
B2K4-8	S5131@6	-3.73	0.14	127.3	2.0	6.25	1.90
B2K4-10	S5132@1	-4.64	0.15	448.5	4.9	-3.82	1.13
B2K4-10	S5132@2	-4.48	0.13	332.2	3.7	-2.64	1.20
B2K4-10	S5132@3	-4.24	0.14	347.8	4.0	-3.29	1.18
B2K4-10	S5132@4	-4.30	0.14	378.9	5.1	-1.15	1.11
B2K4-12	S5133@1	-17.58	0.12	135.8	2.2	3.01	1.96
B2K4-12	S5133@2	-17.70	0.14	143.2	2.0	3.72	1.86
B2K4-12	S5133@3	-17.72	0.13	142.9	1.8	1.88	1.86
B2K4-14	S5134@1	-5.76	0.13	1051.4	11.2	-3.25	0.68
B2K4-14	S5134@2	-5.65	0.13	1156.4	12.1	-2.88	0.65
B2K4-14	S5134@3	-5.42	0.12	1035.5	10.9	-3.37	0.67
B2K4-14	S5134@4	-5.06	0.13	537.8	5.8	-3.61	0.93
B2K4-16	S5135@1	-4.54	0.13	47.1	0.8		
B2K4-16	S5135@2	-4.74	0.13	25.9	0.5		
B2K4-16	S5135@3	-4.63	0.14	32.6	0.6		
B2K4-16	S5135@4	-5.09	0.12	1.2	0.2		
B4WK2-1	S5136@1	-4.48	0.12	271.1	3.1	0.07	1.40
B4WK2-1	S5136@2	-3.86	0.13	243.2	2.8	2.87	1.38
B4WK2-1	S5136@3	-3.96	0.13	312.3	3.5	4.68	1.24
B4WK2-1	S5136@4	-4.05	0.12	65.4	1.1		
B4WK2-2	S5137@1	-17.00	0.15	32.3	1.0		
B4WK2-2	S5137@2	-16.81	0.12	90.3	1.2	1.01	2.15
B4WK2-2	S5137@3	-16.77	0.14	89.2	1.2	0.88	2.26
B4WK2-2	S5137@4	-16.83	0.12	166.8	2.0	1.08	1.77
B5K2-2	S5138@1	-24.74	0.15	232.7	2.7	-1.30	1.42
B5K2-2	S5138@2	-24.75	0.14	220.2	2.8	0.17	1.62
B5K2-2	S5138@3	-24.76	0.13	159.0	2.0	0.20	1.67
B5K2-4	S5139_XS1@1	-2.18	0.12	9.5	0.3		
B5K2-4	S5139_XS1@2	-1.98	0.12	3.7	0.2		
B5K2-4	S5139_XS1@3	-1.80	0.14	3.3	0.2		
B5K2-4	S5139_XS1@4	-1.68	0.12	1.9	0.1		
B5K2-4	S5139_XS1@5	-1.61	0.13	1.5	0.1		
B5K2-4	S5139_XS1@6	-1.57	0.14	2.2	0.1		
B5K2-4	S5139_XS1@7	-1.88	0.13	2.3	0.1		
B5K2-4	S5139_XS2@1	-2.03	0.13	7.1	0.3		
B5K2-4	S5139_XS2@2	-1.84	0.15	4.5	0.2		

Table 3.5. Cont.

Sample	Spot	$\delta^{13}C$ (‰) (VPDB)	2σ error (‰)	N (at. ppm)	2σ error (ppm)	$\delta^{15}N$ (AIR)	2σ error (‰)
B5K2-4	S5139_XS2@3	-1.73	0.14	1.6	0.1		
B5K2-10	S5140@1	-5.16	0.14	707.8	8.1	0.55	0.90
B5K2-10	S5140@2	-2.62	0.12	43.5	0.9		
B5K2-10	S5140@3	-5.76	0.14	15.8	0.4		
N1K5-1	S5141@1	-3.20	0.13	14.4	1.0		
N1K5-1	S5141@2	-3.19	0.15	9.4	0.3		
N1K5-1	S5141@3	-3.31	0.12	22.0	0.5		
N1K5-1	S5141@4	-3.16	0.12	14.5	0.6		
N1K5-1	S5141@5	-3.23	0.14	11.8	0.3		
N1K5-2	S5142@1	-16.40	0.13	2468.1	25.1	3.79	0.43
N1K5-2	S5142@2	-16.37	0.13	1490.7	16.1	3.36	0.54
N1K5-2	S5142@3	-16.33	0.14	639.6	7.3	2.91	0.83
N1K5-2	S5142@4	-16.38	0.14	381.6	4.2	3.02	1.05
N1K5-2	S5142@5	-16.39	0.14	364.5	4.0	2.99	1.25
N1K5-2	S5142@6	-16.39	0.12	83.1	1.2	2.40	2.53
N1K5-2	S5142@7	-16.31	0.16	55.3	0.9		
N1K5-2	S5142@8	-16.38	0.13	40.4	0.8		
N1K5-2	S5142@9	-16.39	0.13	394.4	4.3	7.09	1.05
N1K5-2	S5142@10	-16.55	0.13	20.0	0.5		
N2K4-2	S5143@1	-9.11	0.13	157.8	1.9	9.76	1.84
N2K4-2	S5143@2	-8.03	0.13	215.1	2.7	1.75	1.40
N2K4-2	S5143@3	-8.00	0.14	221.9	2.6	0.89	1.39
N2K4-2	S5143@4	-8.97	0.13	236.1	2.7	9.54	1.34
N2K4-2	S5143@5	-8.12	0.15	191.5	2.3	1.44	1.55
N2K4-4	S5144@1	-3.64	0.13	23.8	0.5		
N2K4-4	S5144@2	-3.34	0.14	23.6	0.5		
N2K4-4	S5144@3	-3.44	0.14	110.1	1.9	2.45	2.11
N2K4-4	S5144@4	-4.02	0.14	43.0	0.7		
N2K4-4	S5144@5	-3.89	0.14	46.5	0.8		
N2K4-4	S5144@6	-3.94	0.12	26.7	0.9		
N2K4-4	S5144@7	-4.08	0.12	50.0	0.8		
N2K4-5	S5145@1	-4.10	0.14	191.5	2.6	-4.31	1.56
N2K4-5	S5145@2	-4.15	0.13	203.4	2.5	-3.07	1.47
N2K4-5	S5145@3	-4.05	0.12	193.0	2.3	-2.51	1.46
N2K4-5	S5145@4	-4.24	0.12	197.3	2.6	-4.20	1.34
N2K4-5	S5145@5	-4.10	0.13	192.4	2.3	-3.67	1.51
N2K4-6	S5146@1	-4.31	0.13	11.0	0.4		
N2K4-6	S5146@2	-4.10	0.13	14.9	0.6		
N2K4-6	S5146@3	-4.10	0.13	26.5	0.8		
N2K4-6	S5146@4	-3.96	0.14	18.5	0.4		
N2K4-6	S5146@5	-3.98	0.14	31.1	0.6		
N2K4-7	S5147@1	-3.15	0.13	99.7	1.6	-3.88	2.32
N2K4-7	S5147@2	-3.48	0.15	171.8	2.1	-3.33	1.59
N2K4-7	S5147@3	-3.54	0.12	157.8	2.2	-5.10	1.68
N2K4-7	S5147@4	-3.75	0.15	239.0	3.1	-2.19	1.34
N2K4-7	S5147@5	-4.31	0.12	342.6	3.9	-3.66	1.13
N2K4-8	S5148@1	-4.81	0.14	720.0	8.0	-2.92	0.83

Table 3.5. Cont.

Sample	Spot	$\delta^{13}C$ (‰) (VPDB)	2σ error (‰)	N (at. ppm)	2σ error (ppm)	$\delta^{15}N$ (AIR)	2σ error (‰)
N2K4-8	S5148@2	-5.30	0.13	946.3	9.9	-3.78	0.68
N2K4-8	S5148@3	-4.69	0.14	784.9	8.2	-3.27	0.85
N2K4-8	S5148@4	-5.05	0.12	880.2	9.8	-2.92	0.71
N2K4-8	S5148@5	-4.83	0.13	834.9	9.0	-3.85	0.74
N2K4-8	S5148@6	-4.87	0.14	391.0	4.3	-3.22	1.15
N2K4-8	S5148@7	-5.11	0.13	746.2	7.9	-3.23	0.92
N2K4-8	S5148@8	-4.90	0.16	387.9	4.3	-0.56	1.07
N5K2-2	S5149@1	-16.08	0.13	397.3	4.5	2.86	1.06
N5K2-2	S5149@2	-16.31	0.13	368.1	4.1	2.95	1.10
N5K2-2	S5149@3	-16.20	0.14	387.4	4.6	1.93	1.07
N5K2-2	S5149@4	-15.99	0.12	529.0	5.7	3.07	0.93
N5K2-2	S5149@5	-16.45	0.13	30.9	0.8		
N5K2-5	S5150@1	-5.39	0.13	935.6	10.0	-2.47	0.69
N5K2-5	S5150@2	-4.92	0.14	151.7	2.0	-2.00	1.60
N5K2-5	S5150@3	-5.57	0.16	1210.5	12.5	-3.22	0.69
N5K2-5	S5150@4	-4.80	0.13	9.3	0.3		
N5K2-5	S5150@5	-4.81	0.13	37.2	0.7		
N5K2-5	S5150@6	-13.68	0.14	79.1	1.4	5.42	2.07
N5K2-7	S5151@1	-16.47	0.13	568.2	6.5	2.42	0.89
N5K2-7	S5151@2	-16.34	0.12	884.6	9.4	2.67	0.86
N5K2-7	S5151@3	-16.24	0.13	464.5	5.0	1.73	0.99
N5K2-7	S5151@4	-16.26	0.15	48.7	1.0		
N5K2-7	S5151@5	-16.40	0.12	46.3	0.8		
N5K2-7	S5151@6	-16.25	0.15	49.6	1.1		
N5K2-7	S5151@7	-16.19	0.14	375.9	4.2	2.61	1.10
N5K2-7	S5151@8	-16.19	0.15	169.7	2.3	3.87	1.94
N5K2-7	S5151@9	-16.36	0.13	183.3	2.2	4.47	1.60

Only eighteen diamonds (72 analyses) have N contents high enough to measure N-isotope compositions (requiring N contents > ~ 80 at. ppm). Nitrogen isotope compositions of the entire analyzed subset show a range between -6.9 to +9.8 ‰ with a main mode in class bin -4 to -3 ‰ and secondary mode in class bin +2 to +3 ‰ (Figure 3.17). $\delta^{15}N$ values of diamonds with peridotitic inclusions range from -6.9 to +4.7 ‰, whilst diamonds with eclogitic inclusions encompass a larger range from -5.1 to +9.8 ‰. Diamonds from CH-7 in Hogberg et al. (2016) have a wider range from -5.7 to +18.7 ‰, with a mode at -3 ‰.

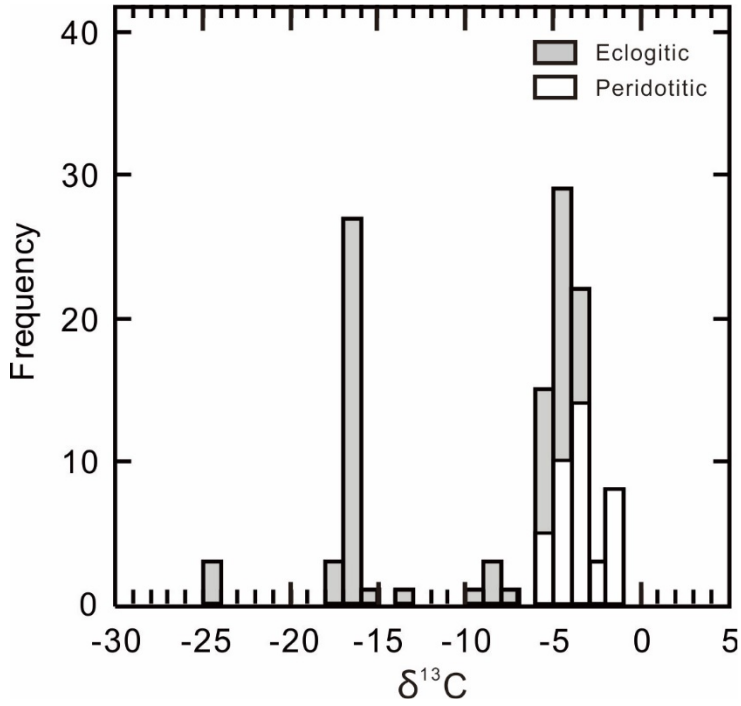

Figure 3.15. $\delta^{13}C$ values for Chidliak inclusion-bearing diamonds (multiple points per diamonds are present). A major mode in class bin -5 to -4 ‰ and a secondary mode in class bin -17 to -16 ‰ are seen, with a tail extending to strongly $\delta^{13}C$ depleted values.

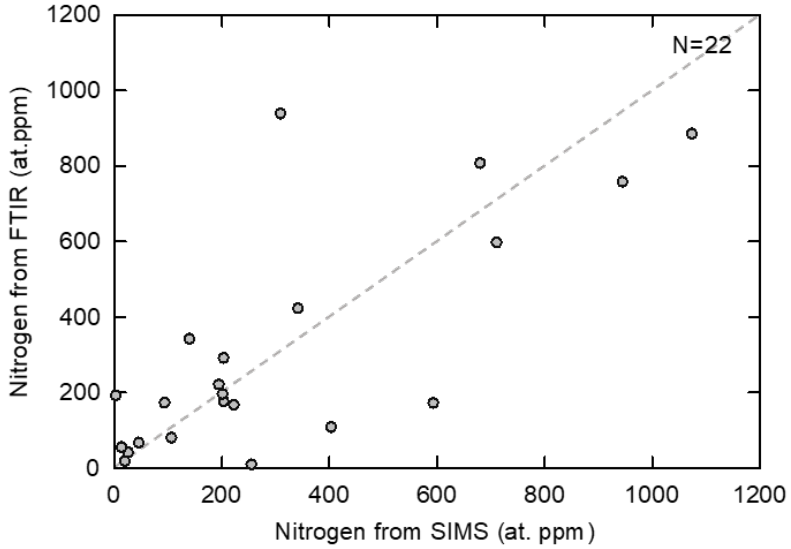

Figure 3.16. Averaged nitrogen contents of 22 inclusion-bearing diamonds from FTIR versus those from SIMS. A crude linear relationship (slope=1) is observed. Outliers are due to significant variations of nitrogen concentration within individual samples.

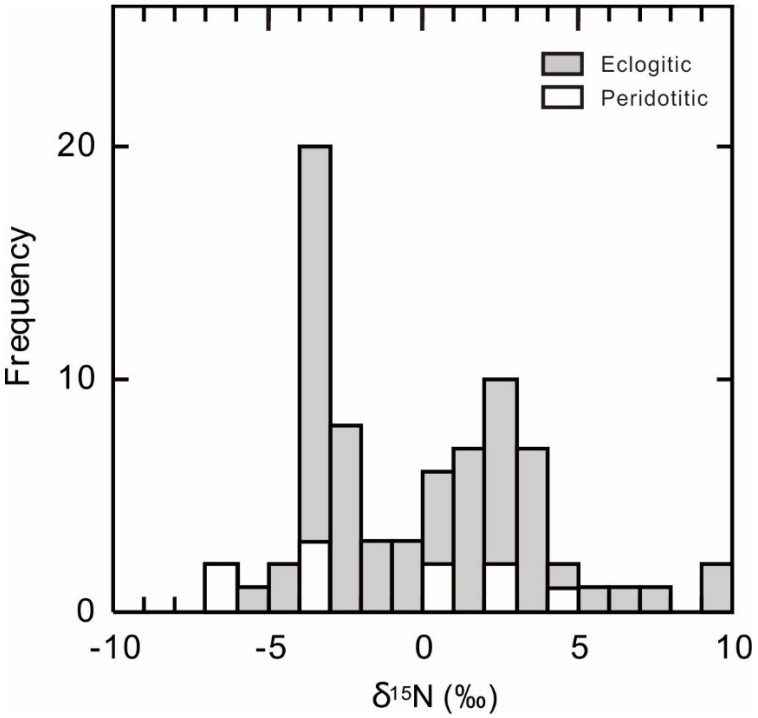

Figure 3.17. Histograms of $\delta^{15}N$ for inclusion-bearing diamonds. Twenty diamonds (72 spots) have a main mode in class bin -4 to -3 ‰ and a secondary mode in class bin +2 to +3 ‰.

3.5.3. CL images and SIMS

Twenty-two diamonds were imaged before SIMS analyses by cathodoluminescence imaging in order to examine the internal growth structure. Due to the recovery of inclusions, mounting and polishing procedures, analyzed fragments are sectioned in random directions. Consequently, the core of diamond likely was not exposed and growth layering is not cut at 90° and hence appears artificially complex.

Most diamonds appear to have nearly constant $\delta^{13}C$ values across growth zones (e.g., Figure 3.18a), but a subset presents large variations in nitrogen content at constant $\delta^{13}C$ (e.g., Figure 3.18b). However, there are two diamonds (N2K4-2 and N5K2-5) that display significant variations in carbon isotopic composition across different layers (Figure 3.18c, d). In the core of sample N2K4-2 (Figure 3.18c), the $\delta^{13}C$ values of -8.1 to -8.0 ‰ is slightly less negative compared to the rim (-9.1 to -9.0 ‰). The carbon isotope data in sample N5K2-5 (Figure 3.18d) display a more dramatic difference from -13.7 to -4.8 ‰ in

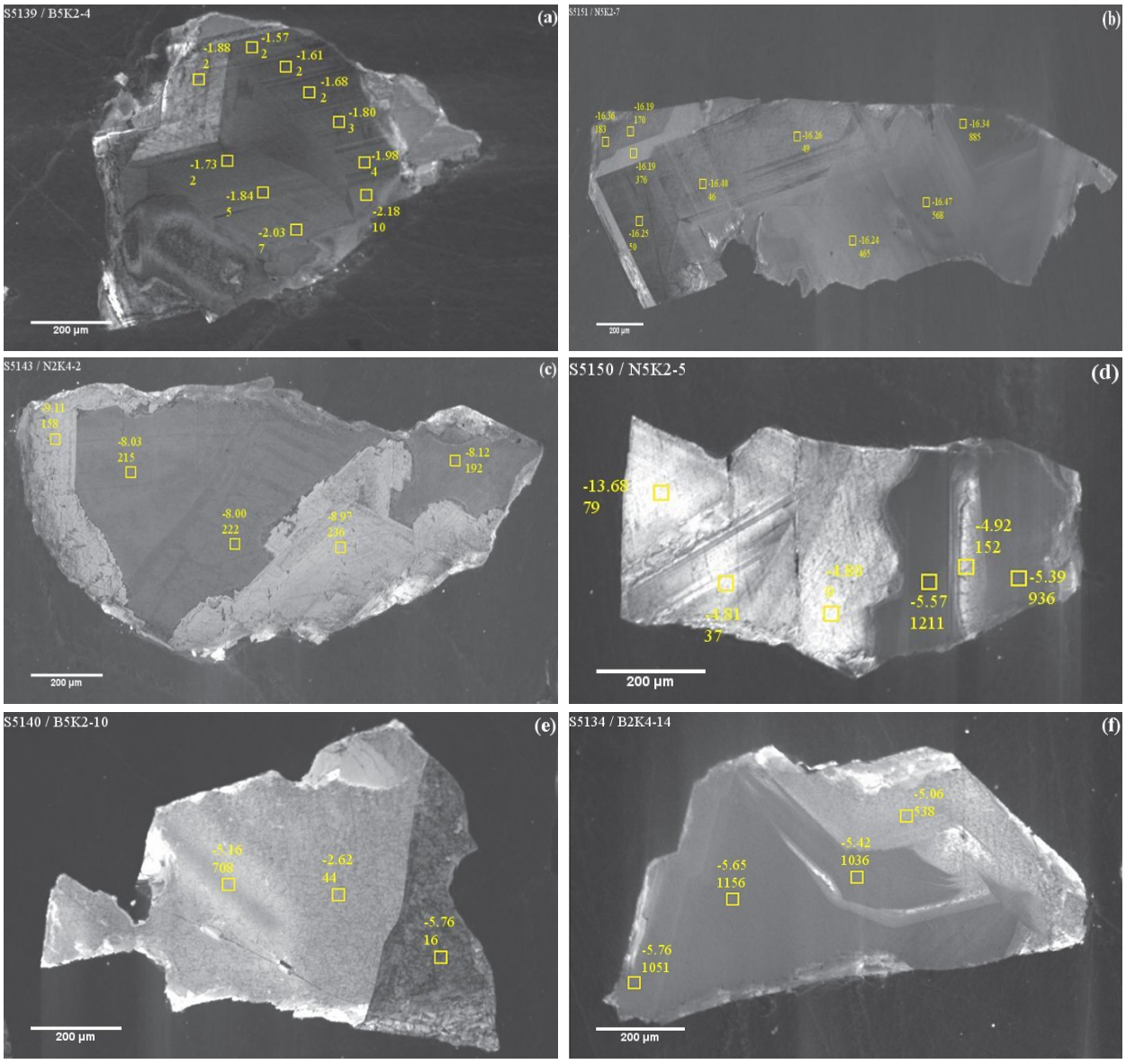

Figure 3.18. CL images for Chidliak diamonds. $\delta^{13}C$ (‰) and nitrogen abundance (at. ppm) are labeled for each spot, $\delta^{13}C$ is above the nitrogen concentration.

separate zones, with evidence of resorption in between. The CL image does not allow for determination of the direction of growth. $\delta^{13}C$ of -5.2 ‰ and -2.6 ‰ within a single growth layer (sample B5K2-10; Figure 3.18e) is evident. An irregular contact between core and rim (Figure 3.18f), a strong increase in nitrogen content and minor increase in $\delta^{13}C$ from core to rim, are indicative of resorption predating rim crystallization. Some stones show more complex CL images and have erratic variations in both nitrogen content and carbon

isotopic composition. No systematic co-variations in $\delta^{13}C$ and nitrogen content were evident for the analyzed diamonds.

3.6. Inclusion Thermometry and Barometry

When multiple minerals are incorporated in the same diamond, the mineral associations enable estimation of the P and T of last equilibration. Touching inclusion pairs re-equilibrate during residence in the mantle. Non-touching pairs, if in equilibrium, yield the P-T conditions of diamond formation; if the chemical/physical conditions changed during subsequent incorporation, they would be in disequilibrium, and therefore, P-T results would be meaningless (Stachel and Harris, 2008).

The Cr-in-garnet P_{38} barometer (Grütter et al., 2006) was applied to the high-Cr garnet (in the diamond B4WK2-1) and yielded the minimum pressure of 50 kbar. As the conductive geotherm of Chidliak is cool (36 mW/m^2; Pell et al., 2013) and the minimum pressure is 50 kbar, a pressure of 55 kbar has been assumed to calculate the temperatures. The mineral association of garnet and two olivines (in the diamond B4WK2-1) yielded temperatures of 1140 to 1150 °C at an assumed pressure of 55 kbar based on Fe-Mg exchange between garnet and olivine (O'Neill and Wood, 1979). The exact spatial relationship among the garnet and olivine inclusions is unknown, but most likely they were separate and hence reflect temperature conditions of diamond formation. This peridotitic diamond formed at temperatures coinciding with the worldwide average (1158 ± 106 °C) for peridotitic diamonds (Stachel et al., 2008). The uncertainty of the geothermometer means that the estimate is only accurate to ± 60 °C or more (Nimis and Grütter, 2010).

A non-touching eclogitic garnet and two clinopyroxenes enclosed in sample N2K4-5, gave temperatures of 1370 to 1377 °C at an assumed pressure of 55 kbar, on the basis of Fe-Mg exchange (Krogh, 1988). The results reflect the temperature of diamond crystallization. These temperatures exceed the mantle adiabat (Rudnick et al., 1988; Stachel and Harris, 2008), and are much higher (~ 250 °C) than the nitrogen-based residence temperatures (1110 to 1114 °C, 1 Ga). There are two possible explanations: 1) Diamond formation was followed by rapid cooling; the temperature difference (~ 250 °C) is, however, much larger

than the maximum estimates for cooling following diamond formation (~ 170 ℃; Meyer and Tsai, 1976). 2) The physical/chemical conditions changed during the successive crystallization of garnet and clinopyroxenes and the non-touching phases are in disequilibrium. The garnet with high Mg# formed from a more mafic eclogitic substrate, then after re-enrichment, clinopyroxenes with decreased Mg# crystallized. In this case, the estimated temperatures are meaningless, and this latter explanation is more likely.

Table 3.6. High precision Al analyses for olivine inclusions

Sample	Al [ppm]	Al %ERR	Cr#	P [kbar]	Al-in-olivine T [℃]
B4WK2-1a	49	7.8	18	55	1135
B4WK2-1b	43	9.3	20	55	1115
B5K2-10	91	4.5	42	55	1230
N1K5-1	28	14.3	13	55	1057
N2K4-4	27	15.0	15	55	1052
N2K4-6	25	15.7	16	55	1046

The Al-in-olivine thermometer (Bussweiler et al., 2017) could be applied to six olivines from five diamonds; These olivine inclusions were analyzed for Al, Ca and Cr in a trace element mode with very high precision via electron microprobe (Table 3.6). They give temperatures of 1115-1135 ℃ (two olivines in B4WK2-1), 1230 ℃, 1057 ℃, 1052 ℃ and 1046 ℃ when a pressure of 55 kbar is assumed.

For the olivine-garnet assemblage (diamond B4WK2-1), the temperatures calculated via the Al-in-olivine thermometer are in good agreement with those calculated by the garnet-olivine thermometer. The differences in temperatures based on olivine and nitrogen in diamond are acceptable for three samples (differences of 10-60 ℃) but exceed the combined uncertainties of the two thermometers in two instances (differences of 100-110 ℃ for sample B5K2-10 and N2K4-4). The latter deviations may be explained by: 1) The Al-in-olivine thermometer is less reliable for olivines with relatively low Cr#. Bussweiler et al. (2017) suggested that this thermometer is most applicable for olivines with Cr# > 45 with the analyzed Chidliak olivines falling at Cr# 13-42 (Table 3.6). 2) Nitrogen in

diamond gives time-averaged residence temperatures, integrated over a long period of time, but the Al-in-olivine thermometer records the temperature during crystallization of olivines.

Chapter 4: Discussion and Conclusions

4.1. Subcratonic Lithospheric Mantle Beneath the Chidliak Area

4.1.1 The Diamond Source Region

The chemical composition of mineral inclusions in Chidliak diamonds indicates that the inclusion-bearing diamond suite is dominated by an eclogitic affinity (68 %; n=15), with a minor component of peridotitic diamonds (32 %; n=7). This agrees with Nichols (2014; MSc thesis), who studied diamonds without inclusions from Chidliak but used the carbon isotope compositions and overall high nitrogen abundances of the diamonds to suggest an eclogitic source. One of the five peridotitic diamonds contains a harzburgitic garnet and a further three have olivine inclusions with low CaO and relatively high Mg#, which are likely also of harzburgitic origin. The remaining peridotitic diamond contained an olivine with high CaO and relatively low Mg# and thus may derive from a lherzolitic source. The high Cr# (33) of the harzburgitic garnet implies a highly depleted peridotitic source (Griffin et at., 1999) combined with formation at elevated pressure (Grütter and Sweeney, 2000; Grütter et al., 2006). The host diamonds of harzburgitic olivines with a narrow range of Mg# (92.5 to 93.2) derive from typically highly depleted sources, which is consistent with the geochemical composition of the harzburgitic garnet (Gurney, 1984; Bernstein et al., 2007). The diamond incorporating the potentially lherzolitic olivine (Mg# = 91.0) originated in less melt-depleted peridotite.

The eclogitic garnet inclusions with high CaO content and low REE concentrations may indicate formation from crustal protolith (Beard et al., 1996; Donnelly et al., 2007). The presence of positive Eu anomalies in eclogitic garnet and clinopyroxene inclusions indicate that the eclogite protolith experienced low-pressure feldspar fractionation/accumulation processes at crustal pressures (e.g., Ringwood and Green, 1967; Snyder et al., 1997; Barth et al., 2001; Aulbach et al., 2002; Tappert et al., 2005). However, these eclogitic garnet and clinopyroxene inclusions have mantle-like $\delta^{13}C$ values (Table 3.5), and they likely derive from mantle as discussed below (Chapter 4.2.1).

The median nitrogen concentration for worldwide peridotitic and eclogitic diamonds is 82 at. ppm and 494 at. ppm, respectively (Stachel, 2014). The nitrogen contents of Chidliak

stones vary from 7 to 2443 at. ppm with a median value of 336 at. ppm, and six diamonds have nitrogen greater than 1500 at. ppm. Thus, elevated nitrogen contents broadly indicate an eclogite-dominated source for Chidliak diamonds.

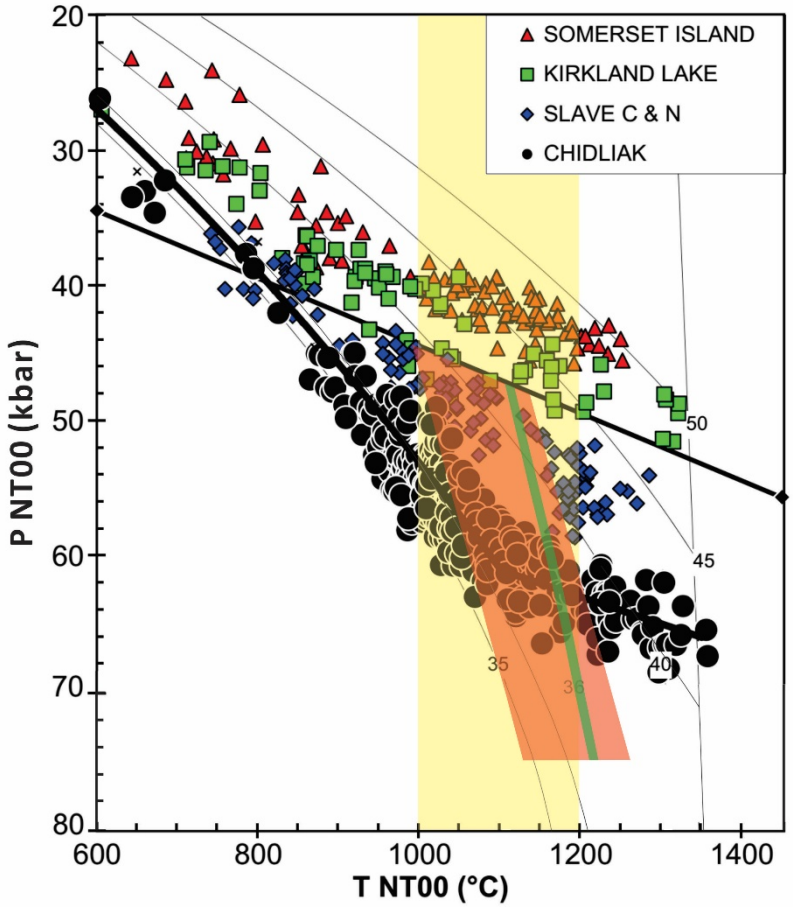

Figure 4.1. An inflected paleogeotherm for Chidliak based on the single clinopyroxene geothermobarometer (Nimis-Taylor, 2000). Figure is modified from Pell et al. (2013). The red band and green band present the average temperatures and 1 sigma range resulting from the single olivine inclusions (Bussweiler et al., 2017) and garnet-olivine pair (O'Neill and Wood, 1979), respectively. The yellow band shows time-averaged mantle residence temperatures based on nitrogen contents.

For peridotitic diamonds, a non-touching garnet-olivine assemblage (in diamond B4WK2-1) reflects a diamond formation temperature of 1140 to 1150 °C (assuming a pressure of 55 kbar), and the results from Al-in-olivine thermometry (Bussweiler et al., 2017) are of 1046-1230 °C (at an assumed pressure of 55 kbar). With two exceptions, these

temperature estimates agree well with nitrogen-based mantle residence temperatures of the associated host diamonds. For eclogitic diamonds, a garnet-clinopyroxene assemblage gives a much higher temperature than nitrogen-based thermometry, either due to the disequilibrium during successive crystallization or diamond formation followed by rapid lithospheric cooling.

The nitrogen concentrations and aggregation states determined by FTIR suggest that time-averaged mantle residence temperatures range from ~ 1000 to 1200 °C, when the assumed mantle residence time is 1 Ga. This range is consistent with the previously studied sample set of Nichols (2014; MSc thesis). Projecting both the results of inclusion thermometry and nitrogen-based temperatures on a xenolith/xenocryst-based cool geotherm (36 mW/m^2; Pell et al., 2013) indicates that the diamonds derive from a depth of ~ 160 to 200 km (Figure 4.1). The majority of Chidliak xenoliths/xenocrysts were sampled from a similar depth as the Chidliak diamonds. The conductive geotherm based on clinopyroxene xenocrysts derived from the deep SCLM exhibits an inflection due to a transient thermal event(s) that occurred contemporaneously with Jurassic kimberlite magmatism in the deepest part of SCLM, as discussed below.

4.1.2. Thermal History

A prominent thermal event prior to kimberlite emplacement is evident based on clinopyroxene geothermobarometry: clinopyroxene inclusions from < ~ 190 km depth imply a cool geotherm (36 mW/m^2) typically associated with stable cratonic areas (Figure 4.1). P-T data for grains collected from the deep portion (> ~ 190 km) define an inflected geotherm and record temperatures in excess of 1350 °C, indicative of massive heating. This implies that clinopyroxenes from > 190 km depth experienced a thermal event that only affected the deepest lithospheric mantle beneath Chidliak. The heat source could be upwelling asthenospheric melts or, as suggested by the supra-adiabatic temperatures, plume-related advective heat transfer into deep lithosphere over short time-scales. The presence of an inflection near the base of the lithosphere implies that the heating event coincided with late Jurassic kimberlite magmatism related to upwelling asthenosphere, Mesozoic-Cenozoic continental rifting and the opening of the Labrador Sea basin at Chidliak (Heaman et al., 2015).

The irregular relationship of the platelet peak area and the nitrogen content (Figure 3.10) is indicative of short-lived heating event(s) and/or strain. As 68 % of the diamonds present degraded platelet peaks, the large heating event constrained by clinopyroxene xenocrysts may have contributed to catastrophic platelet degradation.

4.2. Carbon and Nitrogen

4.2.1. Carbon Sources

The overall carbon isotope compositions (-25 to -1.6 ‰) of the inclusion-bearing sample set have a principal mode in class bin -5 to -4 ‰ (close to the typical mantle value: -5 ‰; Deines, 1980; Cartigny, 2005) and a secondary mode in class bin -17 to -16 ‰, extending to about -25 ‰. These results are consistent with the observation of an eclogite-dominated source component defined by this study and previous work (e.g., Hogberg et al., 2016). The $\delta^{13}C$ values of peridotitic diamonds range from -5.8 to -1.6 ‰; eclogitic diamonds have a wider range from -24.8 to -3.2 ‰, with a bimodal distribution and modes in class bin -17 to -16 ‰ and -5 to -4 ‰. Based on the narrow distribution about the mantle value, the carbon of peridotitic diamonds likely is mantle-derived (Cartigny et al., 2005). For eclogitic diamonds, the source of carbon is discussed below.

$\delta^{13}C$ values from -9.1 to -3.2 ‰

Eclogitic samples with non-depleted ^{13}C values (-9.1 to -3.2 ‰) compare very well with $\delta^{13}C$ values of the majority of worldwide eclogitic diamonds (-8 to -2 ‰; Deines, 2002; Cartigny, 2005). As the internal growth layers of Chidliak diamonds suggest multiple growth events involving distinct melts/fluids (Chapter 3.4), potential carbon sources may involve mixtures of the following reservoirs: 1) Fractionated mantle-sourced carbon; 2) Subducted marine carbonates with $\delta^{13}C$ of ~ 0 ‰ (Javoy et al., 1986; Schidlowski and Aharon, 1992); 3) Average altered oceanic crust (-4.7 ‰; Shilobreeva et al., 2011), which was carried into the mantle during subduction; 4) Methane-bearing fluids/melts from the asthenosphere; 5) The involvement of a very low proportion of organic sediments (average $\delta^{13}C$ of ~ -25 ‰; Schidlowski, 2001; Eigenbrode and Freeman, 2006).

Highly depleted $\delta^{13}C < -10$ ‰

The isotopically strongly $\delta^{13}C$-depleted ($\delta^{13}C < -10$ ‰) of some eclogitic stones near the second mode in class bin -17 to -16 ‰, with some outliers extending to about -25 ‰, can be explained by a number of models about the source of the carbon:

1) A primordial isotopic variability preserved in the mantle during Earth's accretion (Deines, 1980; Haggerty, 1999) has been suggested to provide isotopically light carbon. However, the preservation of primordial mantle compositions has not been confirmed by mantle geochemical data (Cartigny, 2005). In addition, if eclogites relate to subducted oceanic crust, the heterogeneities would not only relate to the eclogitic suite (Smart et al., 2011), which is the least likely to preserve primordial heterogeneities.

2) Deines (2002) suggested that $\delta^{13}C$-depleted diamonds formed through exsolution of dissolved trace-level carbon in mantle minerals (e.g., olivine). The large fractionation factors (range from about -10 to -20 ‰) at mantle temperatures can explain the strongly negative carbon isotopic compositions. However, the process of exsolution of carbon is unclear (Smart et al., 2011) and the solubility of carbon in mantle silicate minerals has been shown to be lower than that in previous work (Keppler et al., 2003), which limits the viability of this model (Smart et al., 2011).

3) Fractionation of mantle-derived fluid/melt in an open system can create strongly negative $\delta^{13}C$ values (Javoy et al., 1986; Galimov, 1991; Cartigny et al., 2001). In this model, if CO_2 fractionated from the growth medium, diamonds would precipitate with increasingly depleted $\delta^{13}C$. However, only < 1 % of the initial fluid/melt reaches $\delta^{13}C$ values less than -14 ‰ and none reach values below -20 ‰ (e.g., Smart et al., 2011). Thus, the $\delta^{13}C$ is still too high. Additionally, uniform $\delta^{13}C$ values within diamonds with low $\delta^{13}C$ (Figure 3.18b) and absence of systematic co-variation of $\delta^{13}C$-[N] do not support formation from a continuously fractionating fluid/melt.

4) Subducted carbon of crustal origin contributes to the low $\delta^{13}C$ values (Milledge et al., 1983; McCandless and Gurney, 1997). Organic sediments have an average $\delta^{13}C$ of ~ -25 ‰ (Schidlowski, 2001; Eigenbrode and Freeman, 2006), whereas marine

carbonates are ~ 0 ‰ (Javoy et al., 1986; Schidlowski and Aharon, 1992). Therefore, low $\delta^{13}C$ carbon may be sourced solely from organic matter or represent mixtures of organic matter and carbonates that are dominated by the former (e.g., McCandless and Gurney, 1997).

Nitrogen isotopes can also be used to trace subducted carbon. The isotopic composition of nitrogen in samples from Earth's mantle and oceanic sediments is distinct. (Meta)sediments have positive $\delta^{15}N$ values, the average is around +6 ‰ (Cartigny, 2005). The increasing metamorphism in the process of subduction may lead to the relative enrichment in ^{15}N, and thus further increasing $\delta^{15}N$ (Haendel et al., 1986; Cartigny et al., 1998). The $\delta^{15}N$ values in Earth's mantle span a larger range from -25 to +15 ‰, with the majority being depleted at around -5 ± 3 ‰ (Cartigny, 2005). Due to the correlation between strongly negative $\delta^{13}C$ values (< -10 ‰) and subduction-related sediments, eclogitic diamonds with such negative $\delta^{13}C$ values are expected to have positive $\delta^{15}N$. A rough association of positive $\delta^{15}N$ and depleted $\delta^{13}C$ is revealed in Figure 4.4: eclogitic diamonds with low $\delta^{13}C$ (< -10 ‰) show $\delta^{15}N$ values from -1.3 to +7.1 ‰ (only one spot has negative $\delta^{15}N$), with a median of +2.9 ‰ (Table 3.5). The elevated $\delta^{15}N$ values are permissible for the Chidliak eclogitic diamonds with strongly negative $\delta^{13}C$ values, which is principally derived from ancient oceanic slabs. Eclogitic diamonds with $\delta^{13}C$ > -10 ‰ have $\delta^{15}N$ values from -5.1 to +9.8 ‰. Due to the dominance of negative $\delta^{15}N$, the overall mantle-like carbon may well derive from the mantle, or through mixing of a predominantly mantle-derived source and subducted carbon.

4.2.2. Correlations Between Carbon and Nitrogen

For eclogitic diamonds worldwide, the maximum nitrogen concentration has been proposed to decrease with decreasing $\delta^{13}C$ (Stachel and Harris, 1997). The highest nitrogen abundances are found at a $\delta^{13}C$ value near -5 ‰ and decrease towards both higher and lower $\delta^{13}C$ (Stachel and Harris, 2009). Diamonds from CH-7 in Hogberg et al. (2016) were found to overall follow this trend, but on the scale of individual diamonds, the association of decreasing $\delta^{13}C$ with increasing nitrogen concentration was observed in some samples. However, such a relationship between nitrogen content and $\delta^{13}C$ has not been identified in this study (Figure 4.2). Systematic co-variations of $\delta^{13}C$ and nitrogen content are neither

evident within individual diamonds nor for the total sample set (Figure 4.2). Instead large variations in nitrogen content with no associated changes in $\delta^{13}C$ are observed (Figure 3.18b). Therefore, closed system Rayleigh fractionation likely is not applicable to Chidliak diamonds. The strong variability in N content at nearly constant $\delta^{13}C$ observed on the scale of individual diamonds and the entire CH-7 sample set (Figure 4.2) then can be explained through: 1) Kinetic effects (related to growth speed) controlling the incorporation of nitrogen in diamond (Cartigny et al., 2011); 2) Mixing of fluids with distinct N contents but constant $\delta^{13}C$; 3) fractionation/addition of N through crystallization/break-down of N-bearing phases such as phlogopite or clinopyroxene (Peats et al., 2012; Smith et al., 2014).

Examining the relationship between $\delta^{15}N$ and nitrogen content (Figure 4.3), no systematic co-variations are observed. A crude trend of decreasing maximum N content with increasing $\delta^{15}N$ (ignoring three N-rich outliers with $\delta^{15}N \sim +3$ to +4 ‰) can be explained by having more than one source of nitrogen: a dominant mantle-derived, negative $\delta^{15}N$ component with variable nitrogen content, mixes with a subduction-derived, positive $\delta^{15}N$ component with low nitrogen abundance. Coherent fractionation trends from a primary diamond forming fluid with low $\delta^{15}N$ and high N content toward higher $\delta^{15}N$ and low N, as observed by Hogberg et al. (2016) are not apparent from Figure 4.3.

Systematic co-variances between $\delta^{13}C$ and $\delta^{15}N$ have been identified on the scale of individual diamonds (e.g., Petts et al., 2015; Smit et al., 2016) and the total sample set (e.g., Thomassot et al., 2007). At Chidliak (Figure 4.4; see also Hogberg et al., 2016), such relationships between $\delta^{13}C$ and $\delta^{15}N$ are absent. An increase in the overall variability of $\delta^{15}N$ with increasing $\delta^{13}C$ may simply reflect strongly increasing sampling density in the same direction.

It is worth noting that the diamonds studied by Thomassot et al. (2007) belong to a single population (from one xenolith), and systematic correlations among $\delta^{13}C$, $\delta^{15}N$, and nitrogen content were recognized on only a centimeter scale within the mantle. Diamonds extracted from a kimberlite pipe consist of different suites that likely formed at different times and depth (Thomassot et al., 2007). Therefore, the lack of systematic correlations among $\delta^{13}C$-$\delta^{15}N$-[N] in this study may result from: 1) mixing between distinct carbon and nitrogen sources; 2) the existence of more than one diamond population.

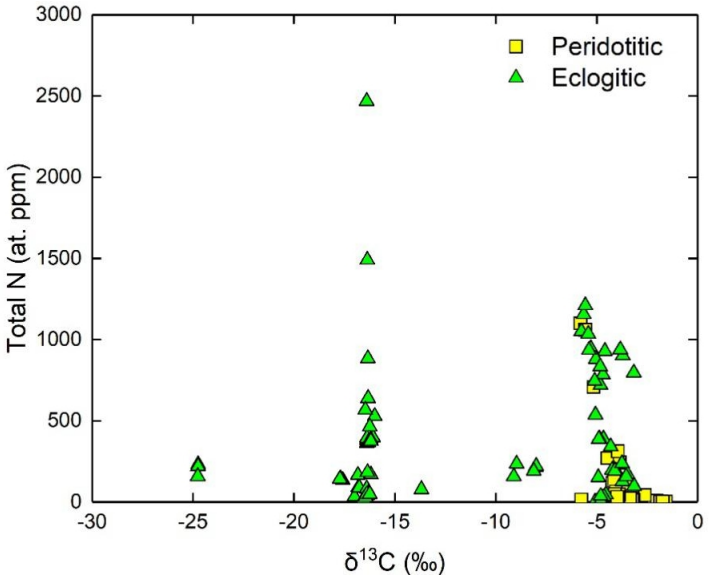

Figure 4.2. Nitrogen concentration (analyzed by SIMS) versus $\delta^{13}C$ for Chidliak inclusion-bearing diamonds. Errors of $\delta^{13}C$ and nitrogen content are smaller than the symbol size. No clear relationship is found. Individual spot analyses are not averaged (N=117).

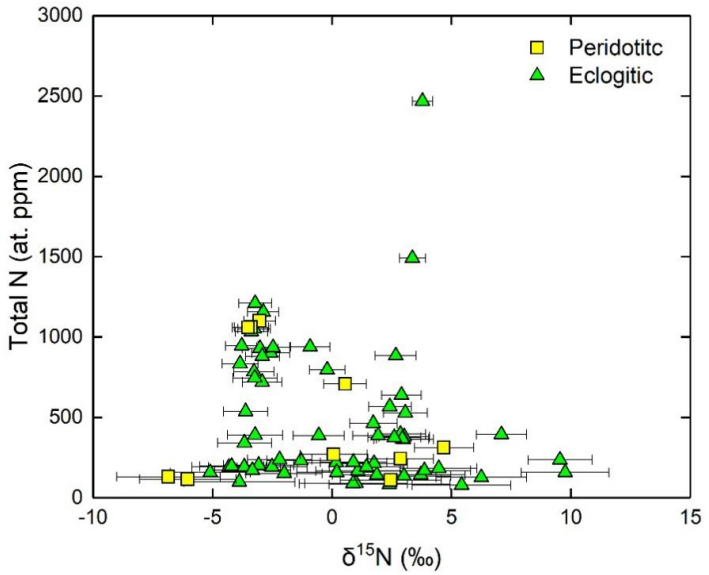

Figure 4.3. Nitrogen content (analyzed by SIMS) versus $\delta^{15}N$ for Chidliak inclusion-bearing diamonds. Error of nitrogen content is smaller than the symbol size; error bars for $\delta^{15}N$ are 2σ . No systematic co-variation was observed. Individual spot analyses are not averaged (N=72).

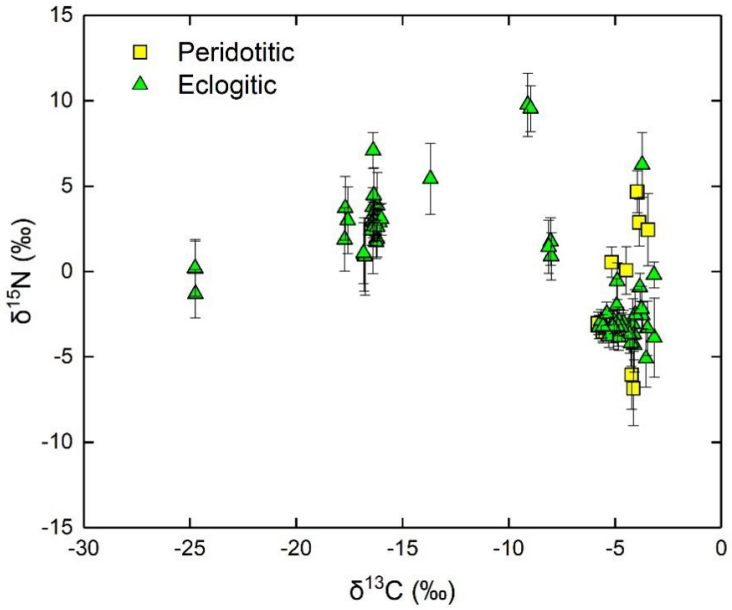

Figure 4.4. $\delta^{15}N$ versus $\delta^{13}C$ for Chidliak inclusion-bearing diamonds. Error bars for $\delta^{15}N$ are 2σ; error of $\delta^{13}C$ is smaller than the symbol size. Individual spot analyses are not averaged (N=72).

4.3. Diamond Growth Mechanism

SIMS data and CL images of inclusion-bearing diamonds reveal at least two distinct growth episodes, with diamond N5K2-5 displaying large $\delta^{13}C$ variability (from -13.7 to ~ -5 ‰) in two distinct zones (Figure 3.18d). On the scale of individual diamonds, multiple pulses of fluids/melts are represented by slightly more negative $\delta^{13}C$ in the core than in the rim (diamond N2K4-2; Figure 3.18c), by a large variability in nitrogen abundance at nearly constant $\delta^{13}C$, and by random fluctuations of $\delta^{13}C$ within the same growth layer (diamond B5K2-10; Figure 3.18e). Signs of resorption imply that shifts in $\delta^{13}C$ typically occur between two crystallization stages. Differences in nitrogen abundance and aggregation state for separate spots within individual diamonds lead to apparent temperature differences up to 90 °C. This likely relates to multiple crystallization events that either occurred over a long-time span (billions of years) or in a rapidly cooling environment. The quality of the FTIR spectra and the baseline correction, however, may also contribute to apparent temperature differences.

One diamond (N3K3-1) has a colourless core with a yellow coat, implying two episodes of diamond growth. More yellow coated samples associated with two growth episodes from Chidliak are reported in recent work of Lai et al. (2018; MSc thesis). The presence of nitrogen C centers in one diamond (B3K3-3) indicates that it may have crystallized in the last stage during diamond formation, or it may be taken at least as circumstantial evidence of multiple episodes of diamond growth.

4.4. Conclusions

The geochemical composition of syngenetic inclusions in diamonds from the CH-7 kimberlite at Chidliak suggests a predominance of eclogitic diamonds with a minor peridotitic suite. The determination of a strong skewness of $\delta^{13}C$ values towards ^{13}C depleted compositions and relatively high nitrogen content supports a predominantly eclogitic-affinity for Chidliak diamonds. The high Mg# (92.5-93.2) of most olivines and the presence of subcalcic garnet are evidence for peridotitic diamond formation in a strongly depleted harzburgitic reservoir. The low Mg# (91.0) of one olivine implies additional peridotitic diamond formation in less melt depleted peridotite (lherzolite). The high Cr content (Cr_2O_3 > 10 wt%) of the harzburgitic garnet is a signature of diamond formation in a depleted peridotitic reservoir at high pressure.

A separate garnet-olivine inclusion pair and multiple single olivine inclusions in diamond yield temperatures (~ 1050 to 1230 °C) in agreement with nitrogen-based thermometry. Based on an assumed residence time of 1 Ga, nitrogen thermometry gives mantle residence temperatures from ~ 1000 to 1200 °C (mainly 1050 to 1150 °C). Projecting the inclusion- and nitrogen-based temperature data on local 36 mW/m^2 paleogeotherm derived from clinopyroxene xenocrysts (Pell et al., 2013) gives a diamond formation depth of ~ 160 to 200 km. The thick SCLM beneath Chidliak allows for formation of diamonds at greater depth (up to 200 km) than typically observed (e.g., Stachel and Luth, 2015).

An inflection of the paleogeotherm towards higher heat flow values occurring near the base of the lithosphere documents the impact of a thermal event coeval with Jurassic kimberlite magmatism associated with upwelling asthenosphere, rifting and opening of the Labrador

Sea basin (Heaman et al., 2015). The dominance of "irregular" diamonds containing degraded platelets may be linked to short-lived heating events and/or to strain.

Only diamonds with recoverable inclusions were analyzed for C-, N-isotope compositions and N content via SIMS. These Chidliak diamonds have a wide distribution in $\delta^{13}C$ values from -25 to -1.6 ‰ with the $\delta^{13}C$ of peridotitic diamonds ranging from -5.8 to -1.6 ‰, and of eclogitic diamonds from -24.8 to -3.2 ‰. $\delta^{15}N$ of Chidliak diamonds shows a range between -6.9 to +9.8 ‰, with $\delta^{15}N$ values of peridotitic diamonds ranging from -6.9 ‰ to +4.7 ‰ and eclogitic diamonds from -5.1 to +9.8 ‰. The narrow range in $\delta^{13}C$ values of peridotitic diamonds from -5.8 to -1.6 ‰ (with a mode in class bin -4 to -3 ‰) is consistent with derivation from mantle-derived carbon. Combining the carbon and nitrogen isotopic characteristics and the association of elevated $\delta^{15}N$ with low $\delta^{13}C$, the isotopically light population ($\delta^{13}C < -10$ %) of eclogitic diamonds has a subduction origin. Diamonds with $\delta^{13}C > -10$ % may result from infiltration of predominantly mantle-derived fluids into recycled oceanic crust.

Chidliak diamonds present complicated CL images and erratic variations in $\delta^{13}C$ and nitrogen, and no systematic co-variations in $\delta^{13}C$ and nitrogen content were evident on the scale of individual diamonds and the total sample set. This suggests involvement of discrete pulses of fluids/melt, rather than Rayleigh fractionation in a fluid limited system as the dominant process. No significant correlations of $\delta^{15}N$ values and nitrogen content was found, but an overall vague trend of decreasing maximum N content with increasing $\delta^{15}N$ may be ascribed to mixing of nitrogen from distinct sources (predominantly mantle-related negative $\delta^{15}N$ with variable N, and subduction-derived positive $\delta^{15}N$ with low N). Overall, the lack of systematic variations among $\delta^{13}C$-$\delta^{15}N$-[N] may relate to mixing of distinct carbon and nitrogen reservoirs combined with more than one diamond population contained in the sample set.

At least two diamond growth events are revealed by the SIMS data, CL images, and the occurrence of a yellow-coated diamond. Diamond resorption occurred between distinct growth episodes. On the scale of individual diamonds, multiple pulses of fluids/melts are represented by isotopically slightly more negative $\delta^{13}C$ in the core compared to the rim, by

large variability in nitrogen abundance at nearly constant $\delta^{13}C$, and by the erratic fluctuations of $\delta^{13}C$ within single growth layers.

References

Aulbach, S., Stachel, T., Viljoen, S. K., Brey, G. P., & Harris, J. W. (2002). Eclogitic and websteritic diamond sources beneath the Limpopo Belt–is slab-melting the link? *Contributions to Mineralogy and Petrology, 143*(1), 56-70.

Barth, M. G., Rudnick, R. L., Horn, I., McDonough, W. F., Spicuzza, M. J., Valley, J. W., & Haggerty, S. E. (2001). Geochemistry of xenolithic eclogites from West Africa, part I: A link between low MgO eclogites and Archean crust formation. *Geochimica et Cosmochimica Acta, 65*(9), 1499-1527.

Beard, B. L., Fraracci, K. N., Clayton, R. A., Mayeda, T. K., Snyder, G. A., Sobolev, N. V., & Taylor, L. A. (1996). Petrography and geochemistry of eclogites from the Mir kimberlite, Yakutia, Russia. *Contributions to Mineralogy and Petrology, 125*(4), 293-310.

Bernstein, S., Kelemen, P. B., & Hanghøj, K. (2007). Consistent olivine Mg# in cratonic mantle reflects Archean mantle melting to the exhaustion of orthopyroxene. *Geology*, *35*(5), 459-462.

Blackadar, R. G. (1967). *Geological reconnaissance, southern Baffin Island, District of Franklin:(Report, figure and maps 16-1966, 17-1966, 18-1966)*. Geological Survey of Canada.

Boyd, F. R., & Gurney, J. J. (1986). Diamonds and the African lithosphere. *Science*, 232(4749), 472-477.

Bulanova, G. P., Griffin, W. L., Ryan, C. G., Shestakova, O. Y., & Barnes, S. (1996). Trace elements in sulfide inclusions from Yakutian diamonds. *Contributions to Mineralogy and Petrology, 124*(2), 111-125.

Bussweiler, Y., Brey, G. P., Pearson, D. G., Stachel, T., Stern, R. A., Hardman, M. F., Kjarsgaard, B. A. & Jackson, S. E. (2017). The aluminum-in-olivine thermometer for mantle peridotites—Experimental versus empirical calibration and potential applications. *Lithos*, *272*, 301-314.

Cartigny, P. (2005). Stable isotopes and the origin of diamond. *Elements, 1*(2), 79-84.

Cartigny, P., Harris, J. W., & Javoy, M. (1998). Eclogitic diamond formation at Jwaneng: no room for a recycled component. *Science, 280*(5368), 1421-1424.

Cartigny, P., Palot, M., Thomassot, E., & Harris, J. W. (2014). Diamond formation: a stable isotope perspective. *Annual Review of Earth and Planetary Sciences, 42*, 699-732.

Cawood, P. A., McCausland, P. J., & Dunning, G. R. (2001). Opening Iapetus: constraints from the Laurentia margin in Newfoundland. *Geological Society of America Bulletin, 113*(4), 443-453.

Chorlton, L. B. (2007). Generalized geology of the world: bedrock domains and major faults in GIS format. *Geological Survey of Canada, Open File, 5529*(1)

Clifford, T. N. (1966). Tectono-metallogenic units and metallogenic provinces of Africa. *Earth and Planetary Science Letters, 1*(6), 421-434.

Collins, A. T. (1982). Colour centers in diamond. *Journal of Gemmology, 18*(1), 37-75.

Connelly, J. N., & Mengel, F. C. (1996). Definition and refinement of Archean and Paleoproterozoic magmatic and tectonic events in the Nagssugtoqidian Orogen: a summary of conventional U–Pb geochronology results. *In Second DLC Workshop on Nagssugtoqidian Geology. Edited by M FC Engel.* Danish Lithosphere Centre, Copenhagen, Denmark, 71-73.

Connelly, J. N., Thrane, K., Krawiec, A. W., & Garde, A. A. (2006). Linking the Paleoproterozoic Nagssugtoqidian and Rinkian orogens through the Disko Bugt region of West Greenland. *Journal of the Geological Society, 163*(2), 319-335.

Corrigan, D., Pehrsson, S., Wodicka, N., & De Kemp, E. (2009). The Paleoproterozoic Trans-Hudson Orogen: a prototype of modern accretionary processes. *Geological Society, London, Special Publications, 327*(1), 457-479.

Deines, P. (1980). The carbon isotopic composition of diamonds: relationship to diamond shape, colour, occurrence and vapor composition. *Geochimica et Cosmochimica Acta*, *44*(7), 943-961.

Deines, P. (2002). The carbon isotope geochemistry of mantle xenoliths. *Earth-Science Reviews, 58*(3-4), 247-278.

DeVries, R. C. (1975). Plastic deformation and "work-hardening" of diamond. *Materials Research Bulletin, 10*(11), 1193-1199.

Donnelly, C. L., Stachel, T., Creighton, S., Muehlenbachs, K., & Whiteford, S. (2007). Diamonds and their mineral inclusions from the A154 South Pipe, Diavik Diamond Mine, Northwest Territories, Canada. *Lithos, 98*(1-4), 160-176.

Eigenbrode, J. L., & Freeman, K. H. (2006). Late Archean rise of aerobic microbial ecosystems. *Proceedings of the National Academy of Sciences, 103*(43), 15759-15764.

Evans, T. (1992). Aggregation of nitrogen in diamond. *The Properties of Natural and Synthetic Diamond*, 259-290.

Evans, T., & Phaal, C. (1962). Imperfections in Type I and Type II diamonds. *Proc. R. Soc. Lond. A*, *270*(1343), 538-552

Evans, T., & Qi, Z. (1982). The kinetics of the aggregation of nitrogen atoms in diamond. *Proc. R. Soc. Lond. A*, *381*(1780), 159-178.

Evans, T., Kiflawi, I., Luyten, W., Van Tendeloo, G., & Woods, G. S. (1995). Conversion of platelets into dislocation loops and voidite formation in type IaB diamonds. *Proc. R. Soc. Lond. A*, *449*(1936), 295-313.

Fersman, A. E., & Goldschmidt, V. (1911). *Der Diamant*. Heidelberg, Germany. pp. 274.

Field, J. E. (1992). *The properties of natural and synthetic diamond* Academic Press.

From, R. E., Camacho, A. L., & St-Onge, M. R. (2012). Preliminary observations on the nature and origin of the eastern orthogneiss complex of Southern Hall Peninsula, Baffin Island, Nunavut. *Summary of Activities*, 43-54.

From, R. E., St-Onge, M. R., & Camacho, A. L. (2014). Preliminary characterization of the Archean orthogneiss complex of Hall Peninsula, Baffin Island, Nunavut. *Summary of Activities 2013*, 53-62.

From, R. E., Camacho, A., Pearson, D. G., & Luo, Y. (2018). U-Pb and Lu-Hf isotopes of the Archean orthogneiss complex on eastern Hall Peninsula, Southern Baffin Island, Nunavut: Identification of exotic Paleo-to Mesoarchean crust beneath eastern Hall Peninsula. *Precambrian Research, 305*, 341-357.

Galimov, E. M. (1991). Isotope fractionation related to kimberlite magmatism and diamond formation. *Geochimica et Cosmochimica Acta, 55*(6), 1697-1708.

Goss, J. P. (2003). Theory of hydrogen in diamond. *Journal of Physics: Condensed Matter, 15*(17), R551.

Goss, J. P., Coomer, B. J., Jones, R., Fall, C. J., Briddon, P. R., & Öberg, S. (2003). Extended defects in diamond: the interstitial platelet. *Physical Review B*, *67*(16), 165208.

Goss, J. P., Briddon, P. R., Hill, V., Jones, R., & Rayson, M. J. (2014). Identification of the structure of the 3107 cm^{-1} H-related defect in diamond. *Journal of Physics: Condensed Matter, 26*(14), 145801.

Green, D. H., & Ringwood, A. E. (1967). An experimental investigation of the gabbro to eclogite transformation and its petrological applications. *Geochimica et Cosmochimica Acta, 31*(5), 767-833.

Griffin, W. L., O'Reilly, S. Y., & Ryan, C. G. (1999). The composition and origin of sub-continental lithospheric mantle. *Special Publication - Geochemical Society*, *6*13-45.

Grütter, H.S., & Quadling, K.E. (1999). Can sodium in garnet be used to monitor eclogitic diamond potential? In *Proceedings of 7th International Kimberlite Conference, Red Roof Design, Cape Town,* 314-320.

Grütter, H. S., & Sweeney, R. J. (2000). Tests and constraints on single-grain Cr-pyrope barometer models: some initial results. In *GACMAC GeoCanada 2000 Conference, Calgary.*

Grütter, H. S., & Tuer, J. (2009). Constraints on deep mantle tenor of Sarfartoq-area kimberlites (Greenland), based on modern thermobarometry of mantle-derived xenocrysts. *Lithos, 112*, 124-129.

Grütter, H. S., Gurney, J. J., Menzies, A. H., & Winter, F. (2004). An updated classification scheme for mantle-derived garnet, for use by diamond explorers. *Lithos, 77*(1-4), 841-857.

Grütter, H., Latti, D., & Menzies, A. (2006). Cr-saturation arrays in concentrate garnet compositions from kimberlite and their use in mantle barometry. *Journal of Petrology*, *47*(4), 801-820.

Gurney, J.J. (1984). A correlation between garnets and diamonds in kimberlites. In Publs. Geol. Dept. & Univ. Extension, Univ. West. Aust. 8, 143–166.

Gurney, J. J., & Switzer, G. S. (1973). The discovery of garnets closely related to diamonds in the Finsch pipe, South Africa. *Contributions to Mineralogy and Petrology, 39*(2), 103-116.

Gurney, J. J., Harris, J. W., & Rickard, R. S. (1984). Silicate and Oxide inclusions in diamonds from the Orapa Mine, Botswana. In: Kornprobst, J. (Ed.), Kimberlites II: the mantle and crust–mantle relationships. Elsevier, Amsterdam, pp. 3–9.

Haendel, D., Mühle, K., Nitzsche, H. M., Stiehl, G., & Wand, U. (1986). Isotopic variations of the fixed nitrogen in metamorphic rocks. *Geochimica et Cosmochimica Acta*, *50*(5), 749-758.

Haggerty, S. E. (1999). A diamond trilogy: superplumes, supercontinents, and supernovae. *Science, 285*(5429), 851-860.

Harris, J.W. (1968a). The recognition of diamond inclusions. Part 1: syngenetic mineral inclusions. *Industrial Diamond Review 28*, 402–410.

Harris, J.W. (1968b). The recognition of diamond inclusions. Part 2: epigenetic mineral inclusions. *Industrial Diamond Review 28*, 558–561.

Harris, J. W. (1987). Recent physical, chemical, and isotopic research of diamond. *Mantle xenoliths*. Wiley, Chichester, 477-500.

Harris, J. W. (1992). Diamond geology. *The properties of natural and synthetic diamond*, 345-393.

Harris, J. W. & Gurney, J. J. (1979). Inclusions in diamond. *The Properties of Diamond*, 555-591.

Harris, J. W., Hawthorne, J. B., Oosterveld, M. M., & Wehmeyer, E. (1975). A classification scheme for diamond and a comparative study of south African diamond characteristics. *Physics and chemistry of the earth*, 765-783.

Harte, B. & Harris, J. W. (1999). Lower mantle mineral associations in diamonds from Sao Luiz, Brazil. *Mantle Petrology: Field Observations and High-Pressure Experimentation: A Tribute to Francis R. (Joe) Boyd, 6*, 125-153.

Harte, B., Fitzsimons, I. C. W., & Kinny, P. D. (1996). Clinopyroxene-garnet trace element partition coefficients for mantle peridotite and melt assemblages. VM Goldschmidt Conference Abstracts. In *Journal of Conference Abstracts* (Vol. 1, p. 235).

Heaman, L. M., Pell, J., Grütter, H. S., & Creaser, R. A. (2015). U–Pb geochronology and Sr/Nd isotope compositions of groundmass perovskite from the newly discovered Jurassic Chidliak Kimberlite Field, Baffin Island, Canada. *Earth and Planetary Science Letters, 415*, 183-199.

Hoffman, P. F., Bally, A. W., & Palmer, A. R. (1989). Precambrian geology and tectonic history of North America. *The Geology of North America—an Overview*, 447-512.

Hogberg, K., Stachel, T., & Stern, R. A. (2016). Carbon and nitrogen isotope systematics in diamond: Different sensitivities to isotopic fractionation or a decoupled origin? *Lithos, 265*, 16-30.

Howell, D., O'Neill, C. J., Grant, K. J., Griffin, W. L., O'Reilly, S. Y., Pearson, N. J., & Stachel, T. (2012). Platelet development in cuboid diamonds: Insights from micro-FTIR mapping. *Contributions to Mineralogy and Petrology, 164*(6), 1011-1025.

Hunt, L., Stachel, T., & McCandless, T. E. (2008). Diamonds from the Renard kimberlites, Quebec. In *9th International Kimberlite Conference, Frankfurt, German, Extended Abstract No. 9IKC-A-00185,* 1-3.

Hunt, L., Stachel, T., Morton, R., Grütter, H., & Creaser, R. A. (2009). The Carolina kimberlite, Brazil—insights into an unconventional diamond deposit. *Lithos, 112*, 843-851.

Hunt, L., Stachel, T., McCandless, T. E., Armstrong, J., & Muelenbachs, K. (2012). Diamonds and their mineral inclusions from the Renard kimberlites in Quebec. *Lithos, 142*, 267-284.

Jackson, G. D., Hunt, P. A., Loveridge, W. D., & Parrish, R. R. (1990). Reconnaissance geochronology of Baffin Island, NWT. *Radiogenic Age and Isotopic Studies, Report 3: Geological Survey of Canada Paper 89-2*, 123-148.

Jacob, D. E. (2004). Nature and origin of eclogite xenoliths from kimberlites. *Lithos*, *77*(1-4), 295-316.

Janse, A. J. A. (1994). Is Clifford's Rule still valid? Affirmative examples from around the world. In *Diamonds: characterization, genesis and exploration. Diamonds: characterization, genesis and exploration. CPRM Special Publication.* Brasilia, Brazil, 215-235.

Janssen, G., Vollenberg, W., Giling, L. J., Van Enckevort, W., Schaminee, J., & Seal, M. (1991). Rapid growth of single-crystal diamond on diamond substrates. *Surface and Coatings Technology, 47*(1-3), 113-126.

Jaques, A. L., Sun, S. S., & Chappell, B. W. (1989). Geochemistry of the Argyle (AK1) lamproite pipe, Western Australia. *Geological Society of Australia Special Publication, 14*(170), 188.

Javoy, M., Pineau, F., & Delorme, H. (1986). Carbon and nitrogen isotopes in the mantle. *Chemical Geology, 57*(1-2), 41-62.

Jordan, T. H. (1978). Composition and development of the continental tectosphere. *Nature, 274*(5671), 544.

Jugo, P. J., Luth, R. W., & Richards, J. P. (2005). An experimental study of the sulfur content in basaltic melts saturated with immiscible sulfide or sulfate liquids at 1300°C and 1.0 GPa. *Journal of Petrology, 46*(4), 783-798.

Kalsbeek, F., & Nutman, A. P. (1995). Reconnaissance SHRIMP U–Pb dating: assistance for lithological mapping and understanding the tectonothermal evolution of the Nagssugtoqidian orogen. In *Proceedings of the DLC Workshop "Nagssugtoqidian Geology 1995", Danish Lithosphere Center, Copenhagen,* 29–33.

Kalsbeek, F., & Nutman, A. P. (1996). Anatomy of the Early Proterozoic Nagssugtoqidian orogen, West Greenland, explored by reconnaissance SHRIMP U-Pb zircon dating. *Geology*, *24*(6), 515-518.

Keppler, H., Wiedenbeck, M., & Shcheka, S. S. (2003). Carbon solubility in olivine and the mode of carbon storage in the earth's mantle. *Nature, 424*(6947), 414.

Kirkley, M. B., Gurney, J. J., Otter, M. L., Hill, S. J., & Daniels, L. R. (1991). The application of C isotope measurements to the identification of the sources of C in diamonds: a review. *Applied Geochemistry, 6*(5), 477-494.

Kopylova M.G., Tso E., Ma F., Liu J., & Pearson D.G. (2017). Peridotite xenoliths of the Chidliak Kimberlite Province (NE Canada): The North Atlantic cratonic mantle with recent thermal and Ti-Na metasomatic disturbance. In *11th International Kimberlite Conference, Gabarone, Botswana, Extended Abstract No. 11IKC-4578.*

Krogh, R. (2000). The garnet-clinopyroxene Fe^{2+}-Mg geothermometer: an updated calibration. *Journal of Metamorphic Geology, 18*(2), 211-219.

Kullerud, G. (1969). Phase relations in the Cu-Fe-S, Cu-Ni-S, and Fe-Ni-S systems. *Economic Geology Monograph, 4*, 323-343.

Lai, MY., & Stachel, T. (2018). Spectroscopic analysis of yellow diamond. Unpublished MSc thesis, University of Alberta.

Le Maitre, R. W. (1989). A Classification of Igneous Rocks and Glossary of Terms. Blackwell Scientific Publications, Oxford, 193 p.

Litvin, Y. A., & Butvina, V. G. (2004). Diamond-forming media in the system eclogite-carbonatite-sulfide-carbon: experiments at 6.0-8.5 GPa. *Petrology*, *12*(4), 377-387.

MacGregor, I. D., & Manton, W. I. (1986). Roberts Victor eclogites: ancient oceanic crust. *Journal of Geophysical Research: Solid Earth*, *91*(B14), 14063-14079.

Machado, G., Bilodeau, C., Takpanie, R., St-Onge, M. R., Rayner, N. M., Skipton, D. R., & Braden, Z. M. (2012). Hall Peninsula regional bedrock mapping, Baffin Island, Nunavut: Summary of fieldwork. *Summary of Activities*, 13-22.

McCandless, T.E. (2016a). Morphology and breakage study of diamonds from the CH-7 Kimberlite, Chidliak Project, Nunavut. Confidential internal report prepared for Peregrine Diamonds Ltd., 28 January 2016, 34 p.

McCandless, T.E. (2016b). CH-7 Meeting Follow-up Notes. Confidential internal memorandum prepared for Peregrine Diamonds Ltd., 22 February 2016, 8 p.

McCandless, T.E. (2016c). Breakage assessment of diamonds by size class for the CH-7 kimberlite, Chidliak project, Nunavut. Confidential internal memorandum prepared for Peregrine Diamonds Ltd. 24 May 2016, 20 p.

McCandless, T. E., & Gurney, J. J. (1989). Sodium in garnet and potassium in clinopyroxene: criteria for classifying mantle eclogites. *Special Publication - Geological Society of Australia*, *14*(2), 827-832.

McCandless, T. E., & Gurney, J. J. (1997). Diamond eclogites: comparison with carbonaceous chondrites, carbonaceous shales, and microbial carbon-enriched MORB. *Russian Geology and Geophysics, 38,* 394-404.

McDonough, W. F., & Sun, S. (1995). The composition of the Earth. *Chemical Geology, 120*(3-4), 223-253.

Meyer, H. O. (1987). Inclusions in diamond. *In: Nixon, P.H. (Ed.), Mantle Xenoliths*. John Wiley and Sons, Chichester, England, pp. 501–522

Meyer, H. O., & Boyd, F. R. (1969). Mineral inclusions in diamonds. *Carnegie Inst. Wash. Yearb, 67*, 130-135.

Meyer, H. O., & Tsai, H. (1976). The nature and significance of mineral inclusions in natural diamond: A review. *Miner Sci Eng, 8(4), 242-261.*

Milledge, H. J., Mendelssohn, M. J., Seal, M., Rouse, J. E., Swart, P. K., & Pillinger, C. T. (1983). Carbon isotopic variation in spectral Type II diamonds. *Nature, 303*(5920), 791.

Moore, M., & Lang, A. R. (1974). On the origin of the rounded dodecahedral habit of natural diamond. *Journal of Crystal Growth, 26*(1), 133-139.

Neilson, S., Grutter, H., Pell, J., & Grenon, H. (2012). The evolution of kimberlite indicator mineral interpretation on the Chidliak project, Baffin Island, Nunavut. In *10th International Kimberlite Conference, Bangalore, India, Extended Abstract No. 10IKC-162.*

Nichols, K. (2014). Diamond sources beneath the Hall Peninsula, Baffin Island, Nunavut: A preliminary assessment based on Chidliak diamonds. MSc thesis, University of Alberta.

Nowicki, T. E., Coopersmith, H., & Pilotto, D. (2016). Mineral resource estimate for the Chidliak Project, Baffin Island, Nunavut. Report for Peregrine Diamonds Ltd: report number msc16/006r.

Peats, J., Stachel, T., Stern, R. A., Muehlenbachs, K., & Armstrong, J. (2012). Aviat diamonds: A window into the deep lithospheric mantle beneath the northern Churchill Province, Melville Peninsula, Canada. *The Canadian Mineralogist*, *50*(3), 611-624.

Pearson, D. G., Shirey, S. B., Bulanova, G. P., Carlson, R. W., & Milledge, H. J. (1999). Re-Os isotope measurements of single sulfide inclusions in a Siberian diamond and its nitrogen aggregation systematics. *Geochimica et Cosmochimica Acta, 63*(5), 703-711.

Pell, J., Grütter, H., Grenon, H., Dempsey, S., & Neilson, S. (2012). Exploration and discovery of the Chidliak Kimberlite Province, Baffin Island, Nunavut, Canada's newest diamond district. Extended abstract. In *Proceedings of 10th International Kimberlite Conference, Bangalore, India,* 209-227.

Pell, J., Clements, B., Grütter, H., Neilson, S., & Grenon, H. (2013). Following kimberlite indicator minerals to source in the Chidliak Kimberlite Province, Nunavut. *New Frontiers for Exploration in Glaciated Terrain. Edited by RC Paulen and MB McClenaghan. Geological Survey of Canada. Open File, 7374*, 21-26.

Pell, J., Grütter, H., Neilson, S., Lockhart, G., Dempsey, S., & Grenon, H. (2013). Exploration and discovery of the Chidliak Kimberlite Province, Baffin Island, Nunavut: Canada's newest diamond district. In *Proceedings of 10th International Kimberlite Conference, Bangalore, India,* 209-227.

Petts, D. C., Chacko, T., Stachel, T., Stern, R. A., & Heaman, L. M. (2015). A nitrogen isotope fractionation factor between diamond and its parental fluid derived from detailed SIMS analysis of a gem diamond and theoretical calculations. *Chemical Geology*, *410*, 188-200.

Phaal, C. (1964). Plastic deformation of diamond. *Philosophical Magazine*, 10(107), 887-891.

Pokhilenko, N. P., Sobolev, N. V., Reutsky, V. N., Hall, A. E., & Taylor, L. A. (2004). Crystalline inclusions and C isotope ratios in diamonds from the Snap Lake/King Lake kimberlite dyke system: evidence of ultradeep and enriched lithospheric mantle. *Lithos, 77*(1-4), 57-67.

Pollack, H. N., & Chapman, D. S. (1977). On the regional variation of heat flow, geotherms, and lithospheric thickness. *Tectonophysics, 38*(3-4), 279-296.

Rayner, N. M. (2013). New U-Pb geochronological results from Hall Peninsula, Baffin Island, Nunavut. *Summary of Activities*, 9-52.

Richardson, S. H., Gurney, J. J., Erlank, A. J., & Harris, J. (1984). Origin of diamonds in old enriched mantle. *Nature, 310*(5974), 198.

Robinson, D. N. (1979). Surface textures and other features of diamonds. Doctoral dissertation, University of Cape Town.

Rudnick, R. L., Arndt, N. T., & Presper, T. (1988). Geochemistry of granulite terrains and granulite xenoliths: Relevance to present day lower crustal composition. *Terra Cognita, 8*, 271.

Rudnick, R. L., Eldridge, C. S., & Bulanova, G. P. (1993). Diamond growth history from in situ measurement of Pb and S isotopic compositions of sulfide inclusions. *Geology, 21*(1), 13-16.

Rudnick, R. L., McDonough, W. F., & O'Connell, R. J. (1998). Thermal structure, thickness and composition of continental lithosphere. *Chemical Geology, 145*(3-4), 395-411.

Schidlowski, M. (2001). Carbon isotopes as biogeochemical recorders of life over 3.8 Ga of Earth history: evolution of a concept. *Precambrian Research, 106*(1-2), 117-134.

Schidlowski, M., & Aharon, P. (1992). Carbon cycle and carbon isotope record: geochemical impact of life over 3.8 Ga of earth history. *Early organic evolution* (pp. 147-175) Springer.

Scott, D. J. (1995). U–Pb geochronology of a Paleoproterozoic continental magmatic arc on the western margin of the Archean Nain craton, Northern Labrador, Canada. *Canadian Journal of Earth Sciences, 32*(11), 1870-1882.

Scott, D. J. (1996). Geology of the Hall Peninsula east of Iqaluit, Southern Baffin Island. *Geological Survey of Canada, Current Research*, 83-91.

Scott, D. J. (1999). U–Pb geochronology of the eastern Hall Peninsula, Southern Baffin Island, Canada: a northern link between the Archean of West Greenland and the Paleoproterozoic Torngat Orogen of Northern Labrador. *Precambrian Research, 93*(1), 5-26.

Scott, D. J., & Campbell, L. (1993). Evolution of Paleoproterozoic Torngat Orogen, Labrador, Canada: recent advances using U-Pb geochronology and Nd isotope

systematics. Paper presented at the *Geological Society of America, Annual Meeting,* A23.

Scott, D. J., & Gauthier, G. (1996). Comparison of TIMS (U-Pb) and laser ablation microprobe ICP-MS (Pb) techniques for age determination of detrital zircons from Paleoproterozoic metasedimentary rocks from northeastern Laurentia, Canada, with tectonic implications. *Chemical Geology, 131*(1-4), 127-142.

Sellschop, J., Madiba, C., Annegarn, H. J., & Shongwe, S. (1979). Volatile light elements in diamond. *Diamond Research. Industrial Diamond Information Bureau, London, United Kingdom*, 24-30.

Shilobreeva, S., Martinez, I., Busigny, V., Agrinier, P., & Laverne, C. (2011). Insights into C and H storage in the altered oceanic crust: Results from ODP/IODP hole 1256D. *Geochimica et Cosmochimica Acta, 75*(9), 2237-2255.

Skipton, D. R., & St-Onge, M. R. (2013). Paleoproterozoic deformation and metamorphism in metasedimentary rocks west of Okalik Bay: a field template for the evolution of eastern Hall Peninsula, Baffin Island, Nunavut. *Summary of Activities*, 63-72.

Smart, K. A., Chacko, T., Stachel, T., Muehlenbachs, K., Stern, R. A., & Heaman, L. M. (2011). Diamond growth from oxidized carbon sources beneath the northern Slave Craton, Canada: A $\delta^{13}C$–N study of eclogite-hosted diamonds from the Jericho kimberlite. *Geochimica et Cosmochimica Acta, 75*(20), 6027-6047.

Smit, K. V., Shirey, S. B., Stern, R. A., Steele, A., & Wang, W. (2016). Diamond growth from C-H-N-O recycled fluids in the lithosphere: Evidence from CH_4 micro-inclusions and $\delta^{13}C$-$\delta^{15}N$-N content in Marange mixed-habit diamonds. *Lithos*, *265*, 68-81.

Smith, E. M., Kopylova, M. G., Frezzotti, M. L., & Afanasiev, V. P. (2014). N-rich fluid inclusions in octahedrally-grown diamond. *Earth and Planetary Science Letters, 393,* 39-48.

Snyder, D. B. (2010). Mantle lithosphere structure beneath southeast Baffin Island, Nunavut from teleseismic studies. *Geological Survey of Canada, Current Research 2010-8,* 6 p.

Snyder, G. A., Taylor, L. A., Crozaz, G., Halliday, A. N., Beard, B. L., Sobolev, V. N., & Sobolev, N. V. (1997). The origins of Yakutian eclogite xenoliths. *Journal of Petrology, 38*(1), 85-113.

Sobolev, N. V., & Lavrent'ev, J. G. (1971). Isomorphic sodium admixture in garnets formed at high pressures. *Contributions to Mineralogy and Petrology, 31*(1), 1-12.

Sobolev, N. V., Kuznetsova, I. K., & Zyuzin, N. I. (1968). The petrology of grospydite xenoliths from the Zagadochnaya kimberlite pipe in Yakutia. *Journal of Petrology, 9*(2), 253-280.

Sobolev, N. V., Pokhilenko, N. P., & Yefimova, E. S. (1984). Diamond-bearing peridotite xenoliths in kimberlites and the problem of the origin of diamonds. *Geologiya i Geofizika, 25*(12), 62-76.

Stachel, T. (2014). Diamonds. *Geology of Gem Deposists Edition, 2*, 1-28.

Stachel, T., & Harris, J. W. (1997). Syngenetic inclusions in diamond from the Birim Field (Ghana)–a deep peridotitic profile with a history of depletion and re-enrichment. *Contributions to Mineralogy and Petrology, 127*(4), 336-352.

Stachel, T., & Harris, J. W. (2008). The origin of cratonic diamonds—constraints from mineral inclusions. *Ore Geology Reviews*, *34*(1-2), 5-32.

Stachel, T., & Luth, R. W. (2015). Diamond formation—Where, when and how? *Lithos, 220*, 200-220.

Stachel, T., Harris, J. W., Tappert, R., & Brey, G. P. (2003). Peridotitic diamonds from the Slave and the Kaapvaal cratons—similarities and differences based on a preliminary data set. *Lithos*, *71*(2-4), 489-503.

Stachel, T., Viljoen, K. S., McDade, P., & Harris, J. W. (2004). Diamondiferous lithospheric roots along the western margin of the Kalahari Craton—the peridotitic

inclusion suite in diamonds from Orapa and Jwaneng. *Contributions to Mineralogy and Petrology, 147*(1), 32-47.

Stachel, T., Aulbach, S., Brey, G. P., Harris, J. W., Leost, I., Tappert, R., & Viljoen, K. F. (2004). The trace element composition of silicate inclusions in diamonds: a review. *Lithos, 77*(1-4), 1-19.

Stachel, T., Harris, J. W., & Muehlenbachs, K. (2009). Sources of carbon in inclusion bearing diamonds. *Lithos, 112*, 625-637.

Steenkamp, H. M., & St-Onge, M. R. (2013). Overview of the 2013 regional bedrock mapping program on northern Hall Peninsula, Baffin Island, Nunavut. *Summary of Activities*, 27-38.

St-Onge, M., Searle, M. P., & Wodicka, N. (2006). Trans-Hudson Orogen of North America and Himalaya-Karakoram-Tibetan Orogen of Asia: Structural and thermal characteristics of the lower and upper plates. *Tectonics, 25,* TC4006, 22 p.

St-Onge, M., Wodicka, N., & Ijewliw, O. (2007). Polymetamorphic evolution of the Trans-Hudson Orogen, Baffin Island, Canada: integration of petrological, structural and geochronological data. *Journal of Petrology, 48*(2; 2), 271-302.

St-Onge, M., van Gool, Jeroen A M, Garde, A. A., & Scott, D. J. (2009). Correlation of Archaean and Paleoproterozoic units between Northeastern Canada and Western Greenland: constraining the pre-collisional upper plate accretionary history of the Trans-Hudson orogen. *Geological Society Special Publications, 318*, 193-235.

Tappert, R., & Tappert, M. C. (2011). *Diamonds in Nature: A Guide to Rough Diamonds.* Springer, New York, pp. 142.

Tappert, R., Stachel, T., Harris, J. W., Muehlenbachs, K., Ludwig, T., & Brey, G. P. (2005). Diamonds from Jagersfontein (South Africa): messengers from the sublithospheric mantle. *Contributions to Mineralogy and Petrology, 150*(5), 505-522.

Thomassot, E., Cartigny, P., Harris, J. W., & Viljoen, K. F. (2007). Methane-related diamond crystallization in the Earth's mantle: stable isotope evidences from a single diamond-bearing xenolith. *Earth and Planetary Science Letters, 257*(3), 362-371.

Weiss, Y., Kessel, R., Griffin, W. L., Kiflawi, I., Klein-BenDavid, O., Bell, D. R., & Navon, O. (2009). A new model for the evolution of diamond-forming fluids: Evidence from microinclusion-bearing diamonds from Kankan, Guinea. *Lithos, 112*, 660-674.

Whalen, J. B., Wodicka, N., Taylor, B. E., & Jackson, G. D. (2010). Cumberland Batholith, Trans-Hudson Orogen, Canada: petrogenesis and implications for Paleoproterozoic crustal and orogenic processes. *Lithos, 117*(1-4), 99-118.

Wilks, J., & Wilks, E. (1991). *Properties and applications of diamond.* Butterworth-Heinemann Ltd, Oxford. 525 p.

Williams, A. F. (1932). *The genesis of the diamond*. London: Ernest Been Ltd. 636 p.

Wittig, N., Pearson, D. G., Webb, M., Ottley, C. J., Irvine, G. J., Kopylova, M., & Nowell, G. M. (2008). Origin of cratonic lithospheric mantle roots: A geochemical study of peridotites from the North Atlantic Craton, West Greenland. *Earth and Planetary Science Letters, 274*(1), 24-33.

Yefimova, E. S., Lavrent'yev, Y., & Sobolev, V. S. (1984). Dominant calcsilicate association of crystalline inclusions in placer diamonds from southeastern Australia. *Doklady Earth Sci.,* 148-153.

Zhang, Z., & Fedortchouk, Y. (2012). Records of mantle metasomatism in the morphology of diamonds from the Slave Craton. *European Journal of Mineralogy, 24*(4), 619-632.

Appendix A

Methodology

A.1. Sample Preparation

Mineral inclusions within diamonds were identified by binocular microscope and liberated by a steel diamond cracker. The extracted inclusions were mounted in small brass pips using West System® #105 epoxy resin and #206 Hardener, and polished on sand papers with increasing finer media ending with 1μm Buehler® polycrystalline diamond suspension. The inclusions were then carbon coated for analysis.

A.2. Electron Probe Microanalysis (EPMA)

The major and minor elements of inclusions were determined by wavelength dispersive spectrometers (WDS) on a CAMECA SX100 electron microprobe at the University of Alberta. A 20kV accelerating voltage and a 20nA beam current were used, while beam size depended on the size of inclusions. The peak count times ranged from 30-60 seconds, and half the time was utilized on background measurements. Silicate, oxide and sulphide standards were used for calibration. When possible, three spots on each sample were analyzed and averaged. Typical limits of detection for oxides are 0.01 wt%.

The Al, Ca and Cr contents in olivine inclusions were determined via the same electro microprobe in a high-precision mode: a 20kV accelerating voltage, 300 seconds long count times (on peak and background measurements) and a 200 nA beam current were used, and detection limits of 8 ppm for Al, 6 ppm for Ca and 5 ppm for Cr were achieved.

A.3. Laser-ablation ICP-MS

Trace element analyses of selected eclogitic garnet and clinopyroxene inclusions were carried out by in situ laser ablation coupled with sector field inductively coupled plasma-mass spectrometry (LA-SF-ICP-MS) at University of Alberta. The instrument used was a Resonetics 193 nm excimer laser system (RESOlution M-50) connected to a sector-field ICP-MS Thermo Element XR via Nylon tubing. The mass spectrometer was operated in low mass resolution mode ($M/\Delta M$ = ca. 300).

Prior to each analysis, the background levels were measured for 40 seconds. Samples were analyzed for 60 seconds, with a spot size of 50 μm, 10 Hz repetition rate and on-sample fluence of ~ 4 J/cm^2. Ablated aerosols were entrained in a He cell gas flow (1000 mL/min) and Ar (0.8 mL/min) prior to entering the ICP-MS torch. The power of ICP-MS is 1300 W. The torch depth is of 3.5 mm. In order to achieve optimal signals on Co, La and Th and low oxide production rates (ThO/Th < 0.3 %), the flow of Ar-He gas mixture, the position of torch and focusing potentials were optimized. One spot per each inclusion were analyzed due to the size of grains.

The NIST SRM 612 glass standard was used for external calibration and optimization of instrument parameters, in conjunction with internal standardization using isotope ^{43}Ca. Garnet and clinopyroxene secondary standard grains (PHN1671A and BIR-1G) were ran to check for analytical accuracy. Data reduction and acquisition were obtained using Iolite v3 (Paton et al.; https://iolite-software.com/). The results of the secondary standards have the relative uncertainties of typically 5-10 % or better at the 95 % confidence level.

A.4. Fourier Transform Infrared (FTIR) Spectrometry

Nitrogen contents and aggregation states of 74 diamonds were analyzed using a Thermo-Nicolet Nexus 470 FTIR spectrometer at the University of Alberta.

The spectra were collected in transmittance mode per 200 scans, and the wave number range is 650-4000 cm^{-1}, with 4 cm^{-1} spectral resolution. The system was purged with dry nitrogen-oxygen and background measurements were taken at regular intervals (2 hours).

After cleaning of samples in petrol ether, the fragments of diamonds after breakage were mounted on the edge of a glass slide with double-sided carbon tape. Two to three spots on fragments were measured in case of variability in nitrogen concentration and aggregation state within diamonds.

The spectra of samples were corrected for background and baselined using the OMNIC software, followed by normalization and subtraction of a Type II diamond (with 1 cm

thickness) standard spectrum. The Type II diamond was previously baseline corrected and normalized to 11.94 cm^{-1} at 1995 cm^{-1}.

A spreadsheet provided by David Fisher from the DTC Research Center in Maidenhead, UK, was used for deconvolution of sample spectra: the nitrogen related absorbance was converted to the nitrogen content (at. ppm).

A.5. Secondary Ion Mass Spectrometry (SIMS)

$\delta^{13}C$, $\delta^{15}N$ and nitrogen contents of twenty-two inclusion-bearing and one inclusion-free diamonds were measured via secondary ion mass spectrometry (SIMS) on a Cameca IMS1280 ion microprobe in the Canadian Centre for Isotopic Microanalysis (CCIM) at the University of Alberta.

Large fragments of 23 diamonds were mounted in epoxy, and then polished with metal-bonded diamond pads. The mount (M1489) was pressed into indium with CCIM reference materials (diamond S0230 and vitreous carbon S0223A), and subsequently coated with 10 nm of gold prior CL imaging. The CL images were obtained using a Zeiss EVO MA15 instrument. After the CL imaging, the epoxy mount was coated with additional 40 nm of gold.

Using methods and reference materials detailed in Stern et al. (2014), $\delta^{13}C$ analyses were carried out first; nitrogen concentrations and $\delta^{15}N$ were subsequently measured on the same spot.

For the analyses of carbon isotopic ratios, a 20 keV $^{133}Cs^{+}$ primary ion beam with 0.7-2.5 nA was used. The primary beam was first rastered to clean any possible contaminants. Both $^{12}C^{-}$ and $^{13}C^{-}$ were analyzed simultaneously in Faraday cups at mass resolutions of 2000 and 2900, respectively. The analysis time for each spot was ~ 4 minutes. The diamond standard was measured after every four analyses of unknowns. The reference material, diamond S0270 has a $\delta^{13}C_{VPDB}$ = -8.88 ± 0.10 ‰. Uncertainty of analyses is ~ 0.14 ‰ (2σ), including the uncertainty from the RM and the internal error. All results are reported relative to the international Vienna Pee-Dee Belemnite standard (V-PDB).

For N content, a 20 KeV $^{133}Cs^{+}$ primary ion beam with 0.7 nA was used, [$^{12}C^{13}C^{-}$] and [$^{13}C^{14}N^{-}$] were collected simultaneously using a Faraday cup-electron multiplier, combination with high mass resolutions of 6000 and 5500, respectively. The analysis time for each spot was 3.5 minutes. The diamond standard was run after every four analyses of unknowns. The nitrogen abundance of the reference material diamond S0270 was calibrated relative to S0280E diamond and is 1670 at. ppm (±5 ‰ absolute, 2σ) The uncertainties of unknowns in the N abundance measurements reported (Table 3.5) include uncertainties of calibration and reference material.

For $\delta^{15}N$, a 20 KeV $^{133}Cs^{+}$ primary ion beam with 2.3-2.6 nA was used, $^{12}C^{14}N^{-}$ and $^{12}C^{15}N^{-}$ were analyzed simultaneously in a Faraday cup-EM combination at mass resolutions of > 6200 and 5500, respectively. The Faraday cup baseline for N-isotopes was measured prior to each analysis. Electron multiplier counts were corrected for background and deadtime. The analysis time for each spot was 9 minutes. The diamond standard was analyzed after every four analyses of unknowns. The reference material diamond S0270 has $\delta^{15}N_{AIR}$ = -0.40 ± 0.50 ‰. The 95 % confidence uncertainty for the unknowns has a range from ± 0.4 to 2.5 ‰ (depending of N concentration).

References

Stern, R. A. (2014). Methods and reference materials for SIMS diamond C-and N-isotope analysis. Canadian Centre for Isotopic Microanalysis, University of Alberta.

Tappert, R., Stachel, T., Harris, J. W., Muehlenbachs, K., Ludwig, T., & Brey, G. P. (2005). Diamonds from jagersfontein (south africa): Messengers from the sublithospheric mantle. *Contributions to Mineralogy and Petrology, 150*(5), 505-522.

Appendix B

Diamond Photos

B.1. The Morphology of Diamonds from the CH-7 Kimberlite

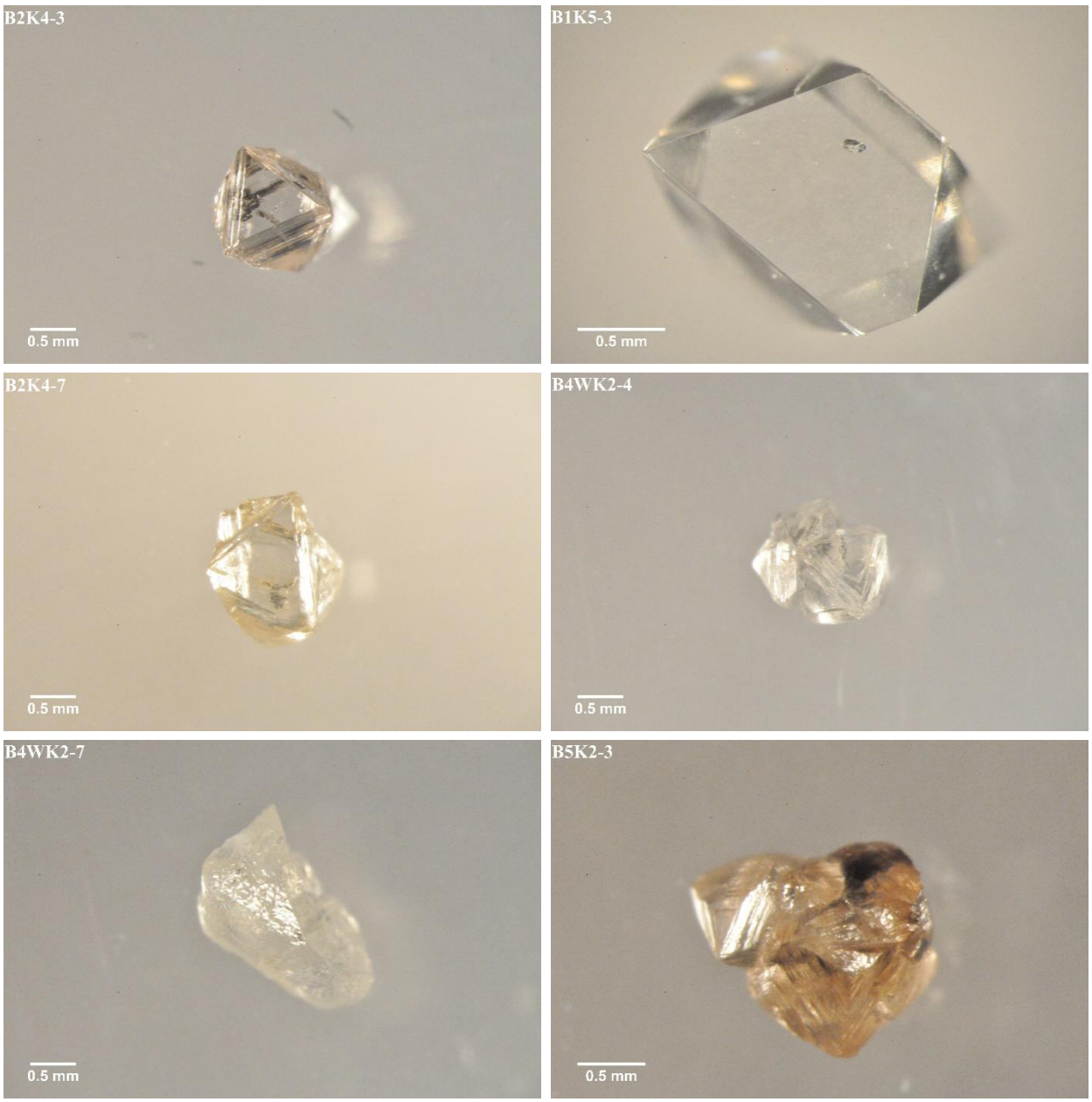

Figure B.1.1. Examples of diamond shapes: octahedron (B2K4-3), flattened octahedron (B1K5-3), twin (B2K4-7), octahedral aggregate (B4WK2-4), frosted cubic fragment (B4WK2-7) and do (dodecahedral-octahedral) aggregate (B5K2-3).

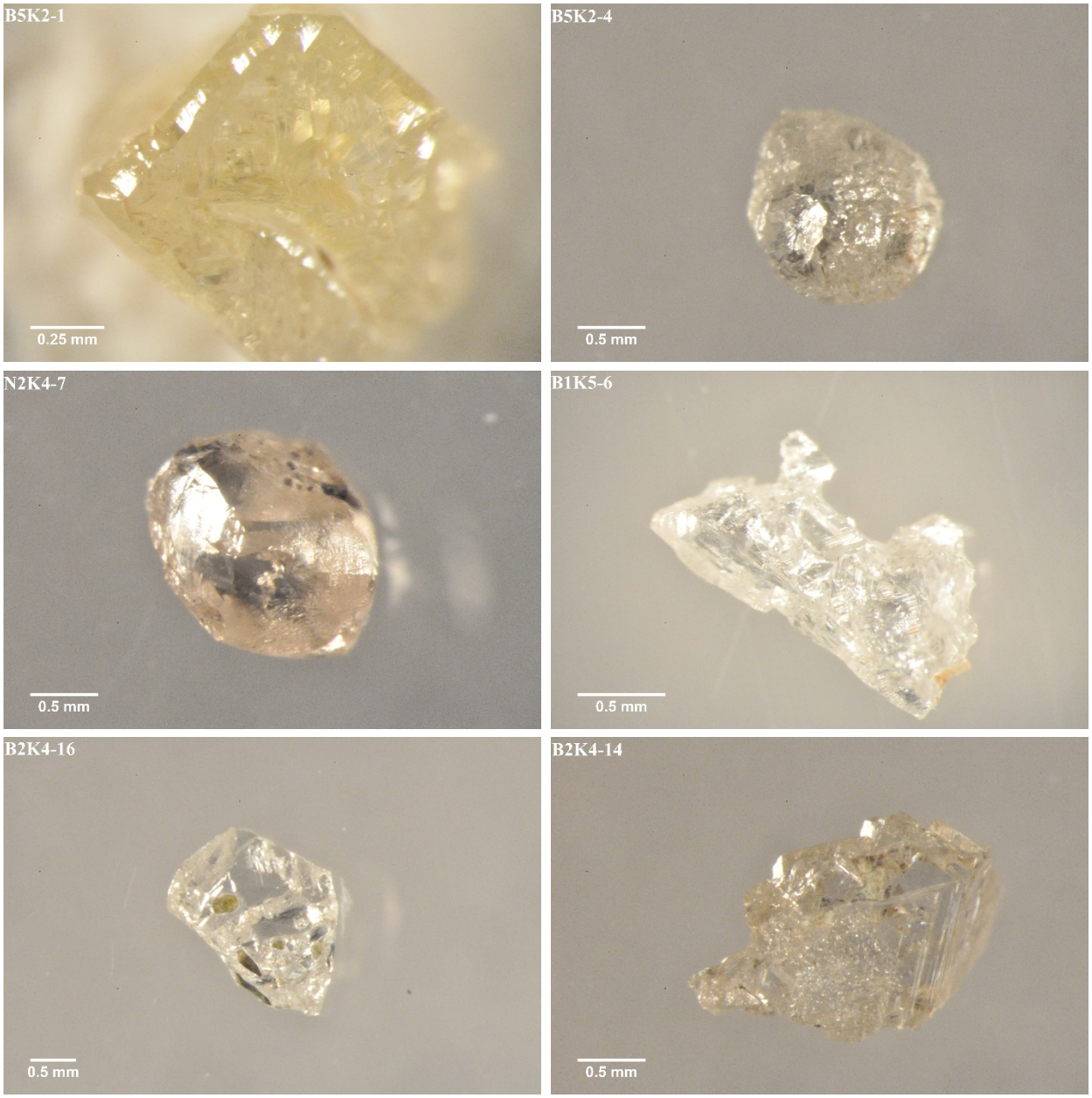

Figure B.1.2. Examples of diamond shapes: re-entrant cuboid (B5K2-1), do (B5K2-4), od (N2K4-7) and irregular diamonds (B1K5-6, B2K4-14 and B2K4-16).

B.2. The Colours of Diamonds from the CH-7 Kimberlite

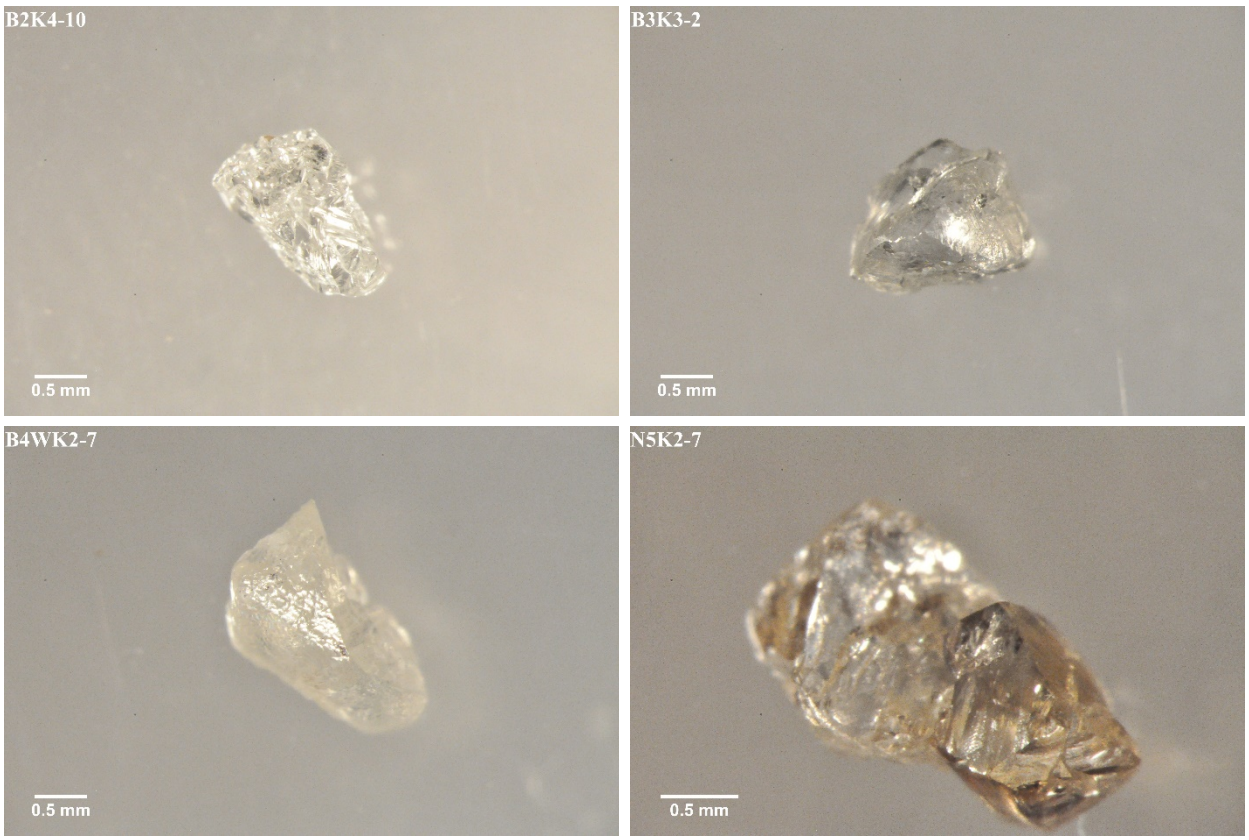

Figure B.2.1. Examples of colourless diamonds. Diamond N5K2-7 is half colourless, half brown.

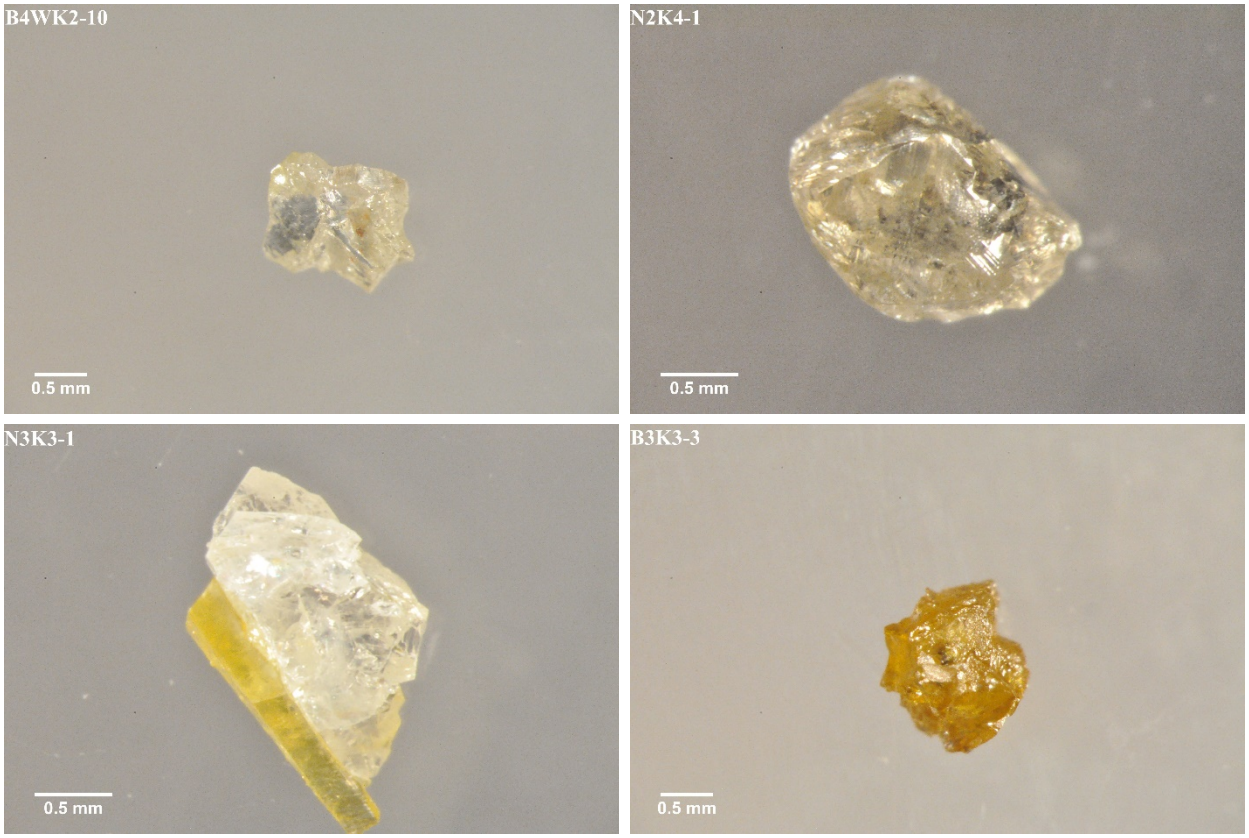

Figure B.2.2. Examples of yellow diamonds, with a range from light yellow to intense yellow. Diamond N3K3-1 has a yellow coat.

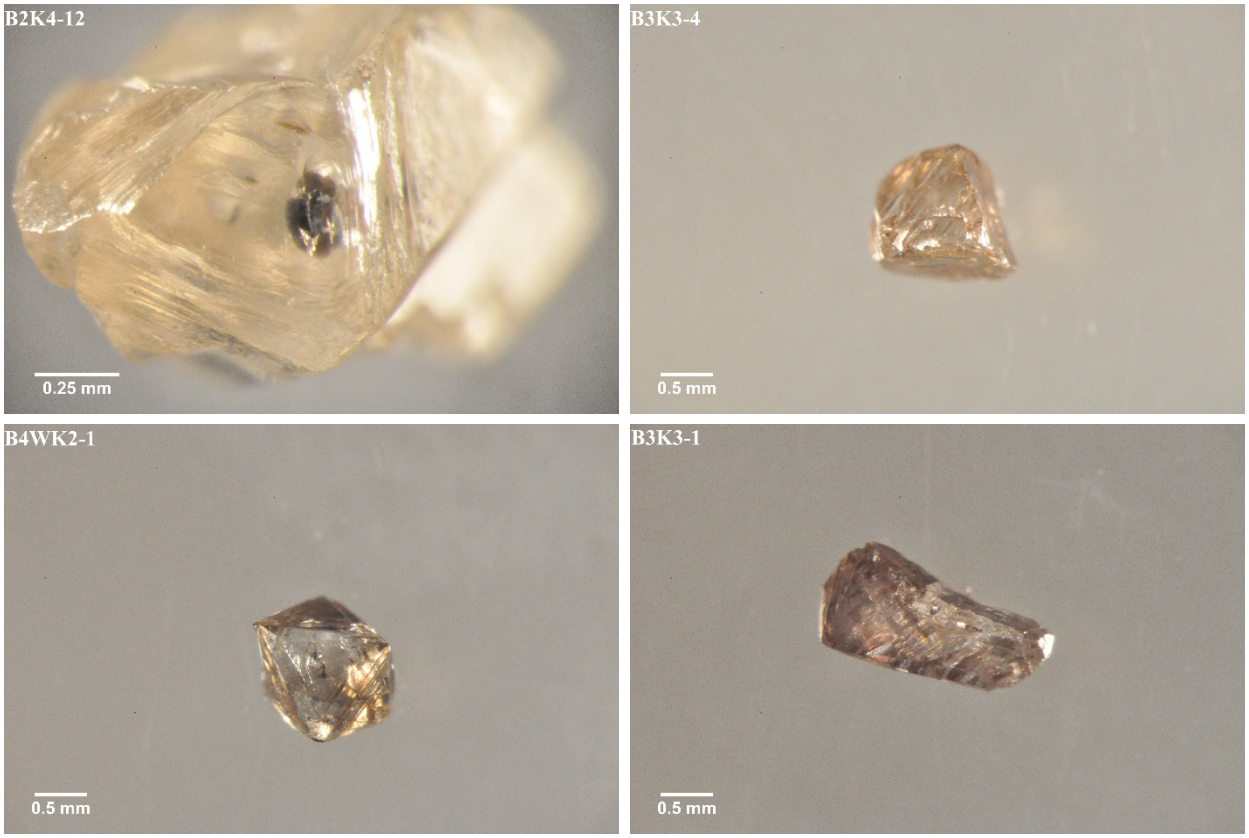

Figure B.2.3. Examples of brown diamonds, with a range from light brown to darker brown.

B.3. The Surface Textures of Diamonds from the CH-7 Kimberlite

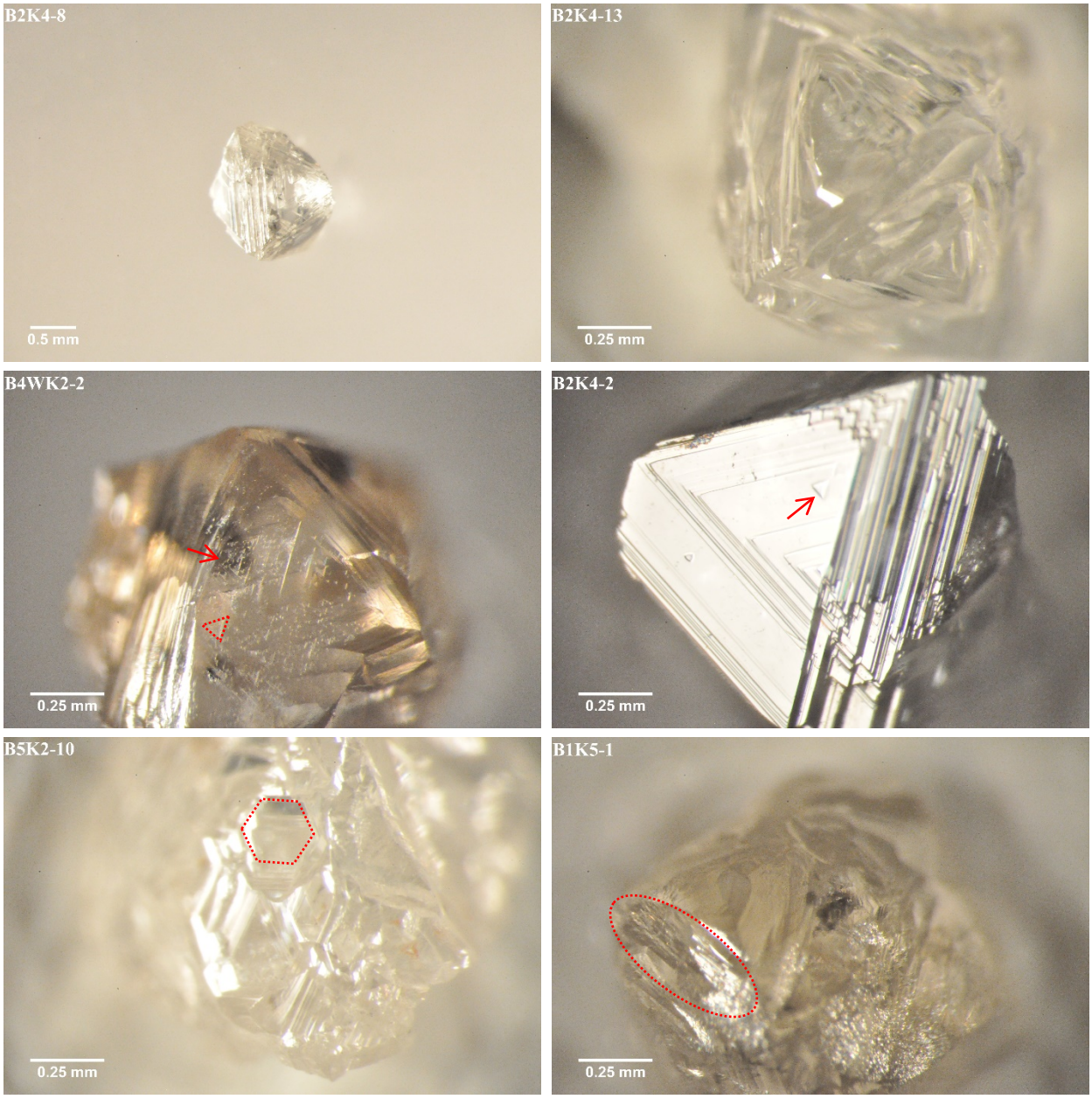

Figure B.3.1. Examples of surface textures of diamonds: stacked growth layers (B2K4-8), shield-shaped laminae (B2K4-13), negative trigons (B4WK2-2), positive trigons (B2K4-2), hexagons (B5K2-10) and hillocks (B1K5-1).

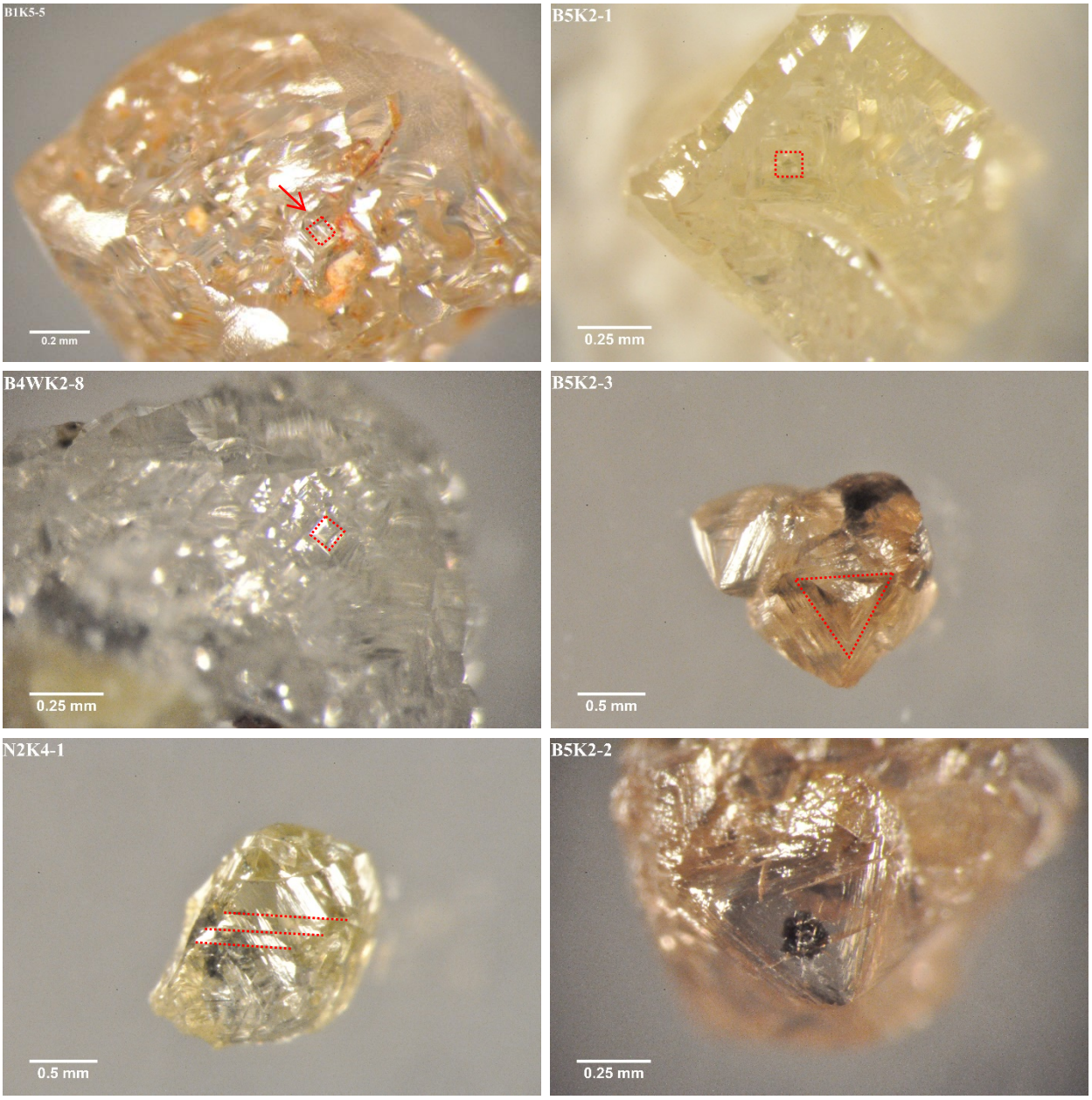

Figure B.3.2. Examples of surface textures of diamonds: positive tetragons (B1K5-5), negative tetragons (B5K2-1 and B4WK2-8), terraces (B5K2-3), deformation lines (N2K4-1) and ruts (last-stage etching; B5K2-2).

B.4. The Breakage of Diamonds from the CH-7 Kimberlite

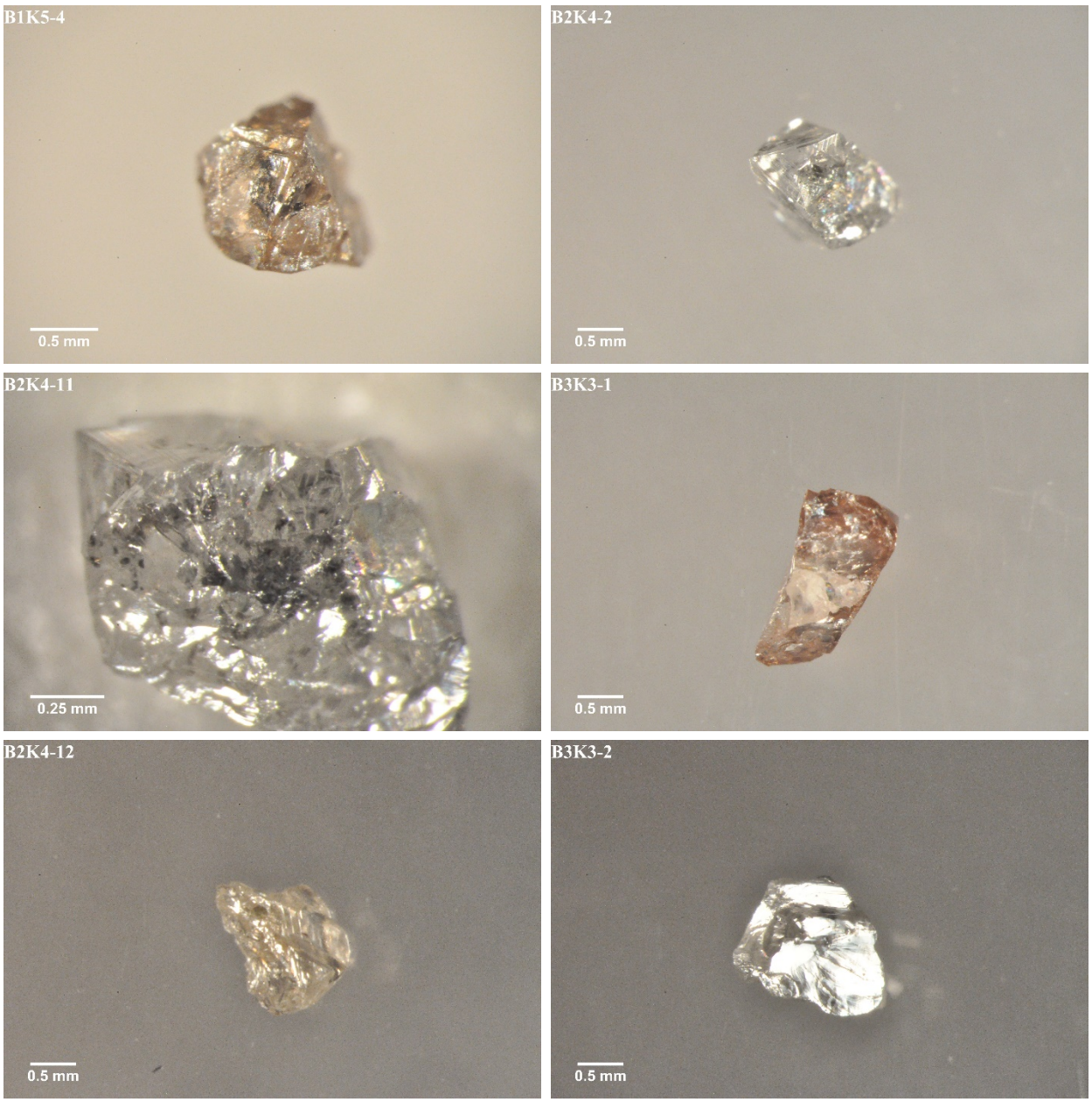

Figure B.4.1. Examples of breakage surfaces of diamonds: breakage surfaces (B1K5-4, B2K4-2, B2K4-11 and B3K3-1), and resorption on breakage surfaces (B2K4-12 and B3K3-2).

B.5. Inclusions of Diamonds from the CH-7 Kimberlite

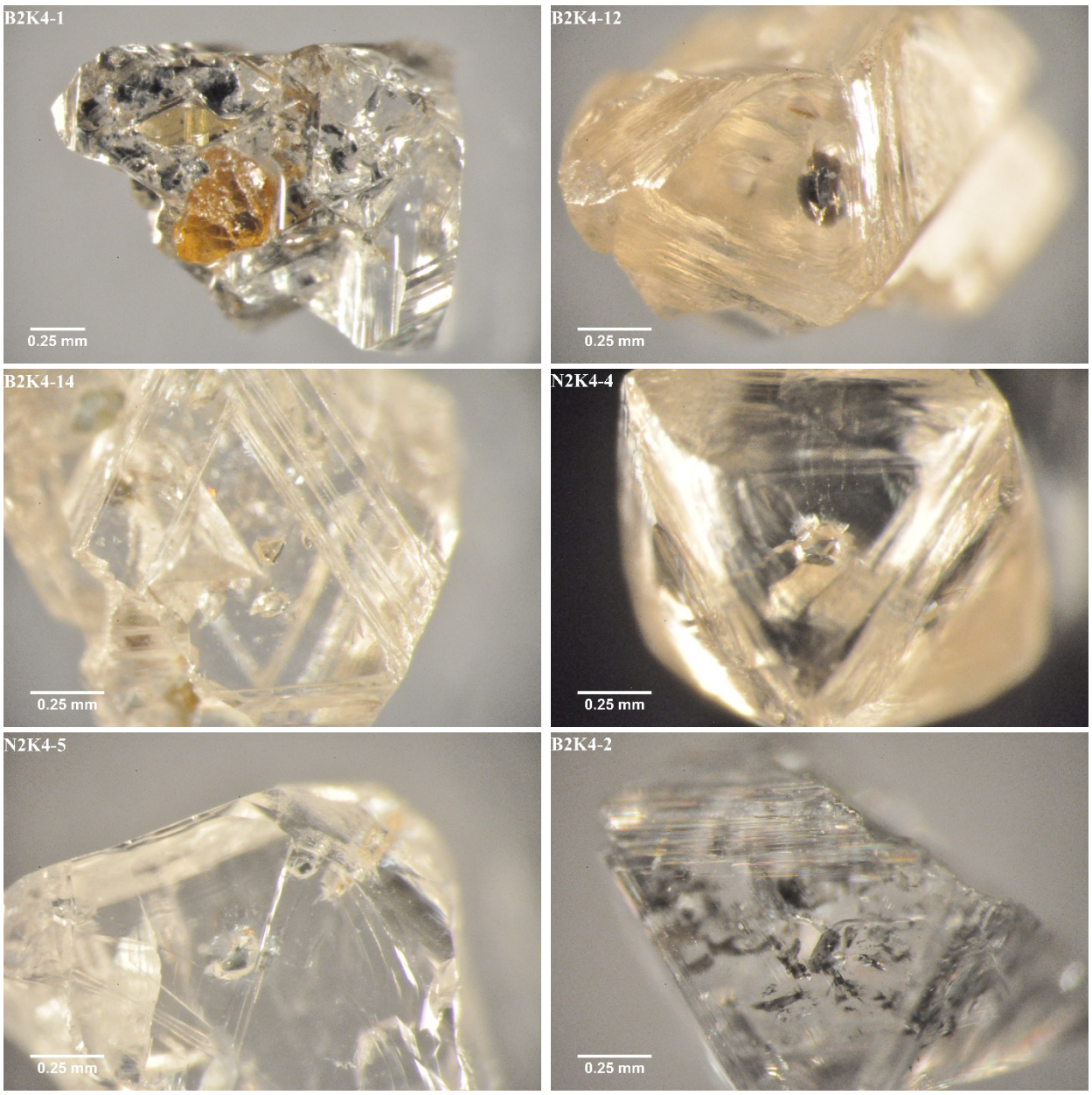

Figure B.5.1. Examples of inclusions within diamonds: orange garnet (B2K4-1), sulphide surrounded by fracture (B2K4-12), faint green clinopyroxenes (B2K4-14), colourless olivine (N2K4-4), mineral association of pale green clinopyroxene and orange garnet (N2K4-5) and graphite cluster (B2K4-2).

Appendix C

CL images

C.1. Annotated CL Images of Diamond Fragments from the CH-7 Kimberlite

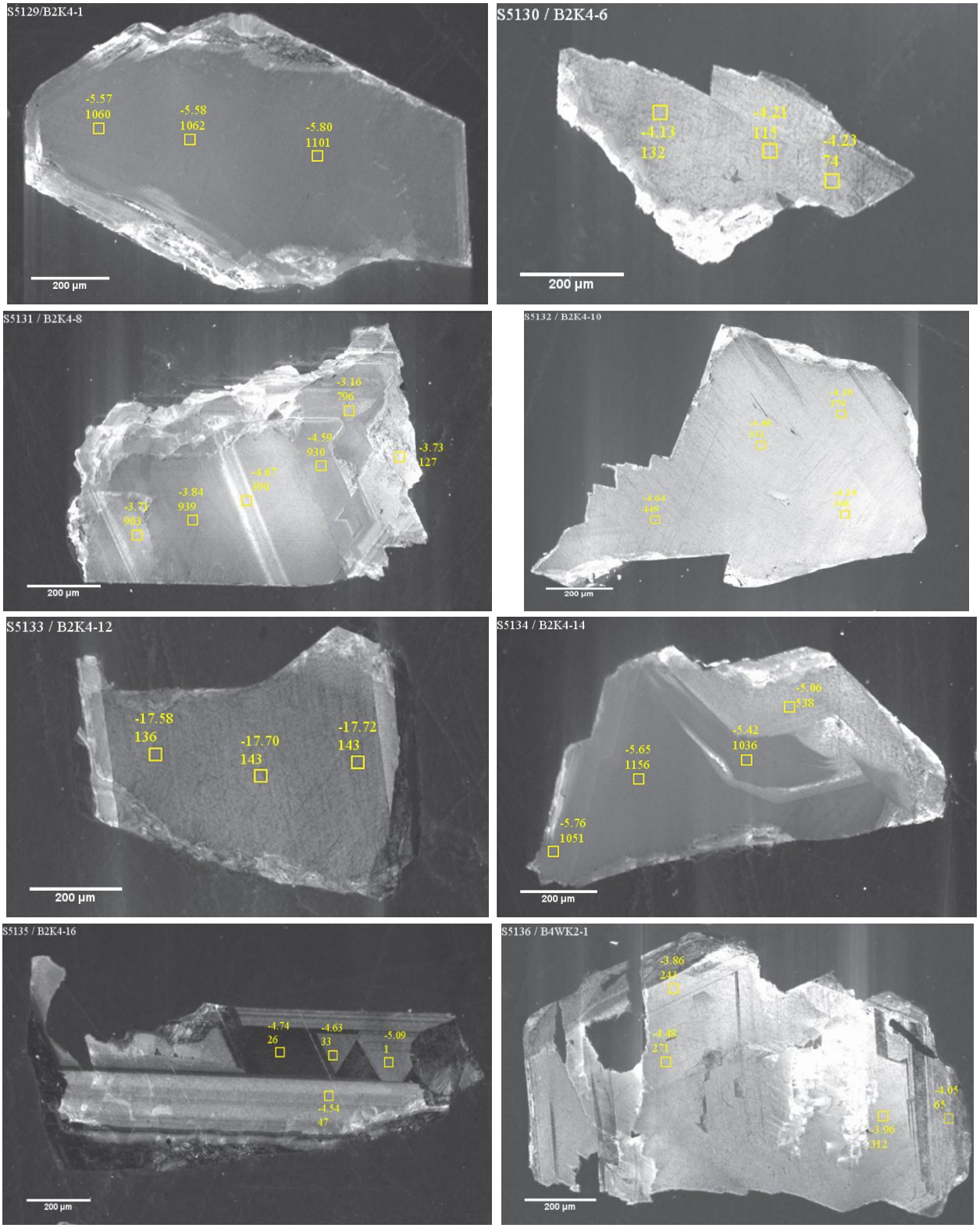

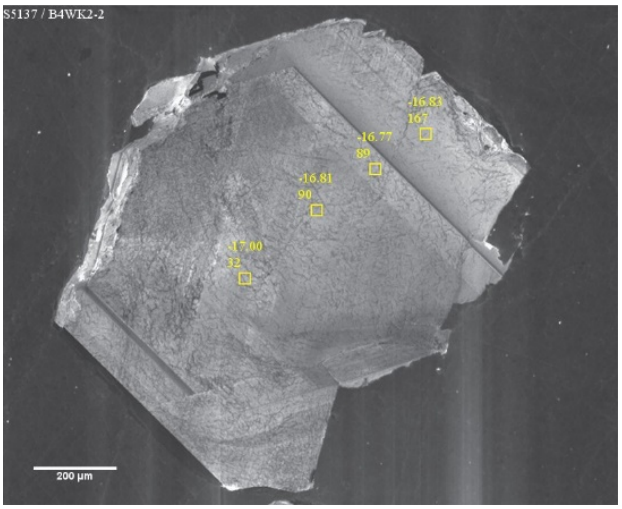
S5137 / B4WK2-2
-16.83
167
-16.77
89
-16.81
90
-17.00
32
200 µm

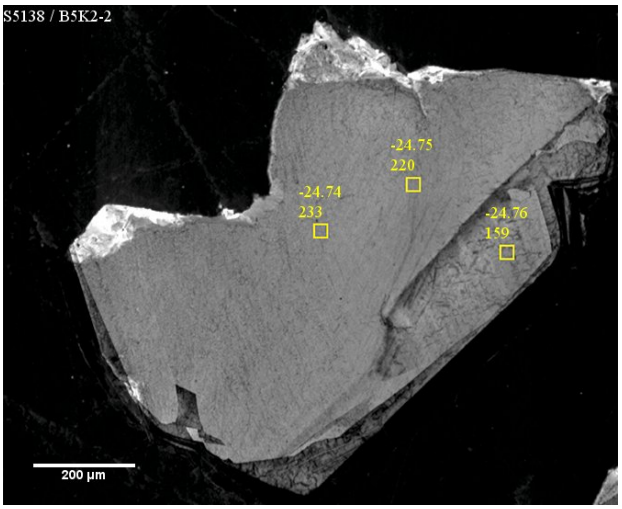
S5138 / B5K2-2
-24.75
220
-24.74
233
-24.76
159
200 µm

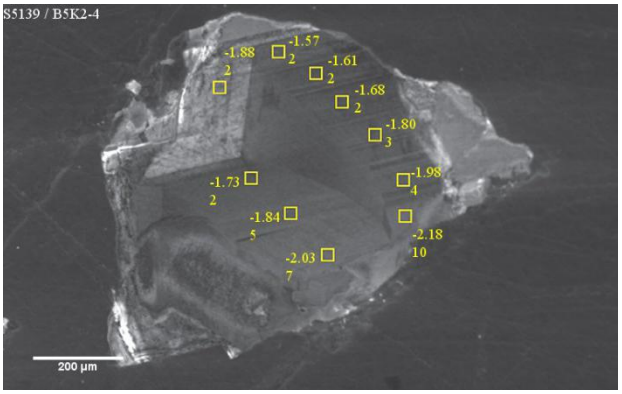
S5139 / B5K2-4
-1.88
2
-1.57
2
-1.61
2
-1.68
2
-1.80
3
-1.73
2
-1.98
4
-1.84
5
-2.18
10
-2.03
7
200 µm

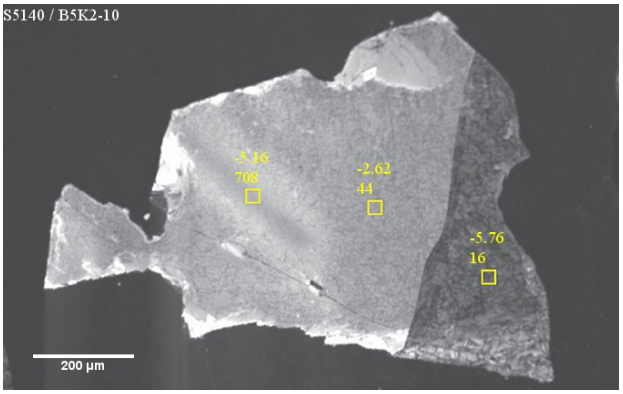
S5140 / B5K2-10
-5.16
708
-2.62
44
-5.76
16
200 µm

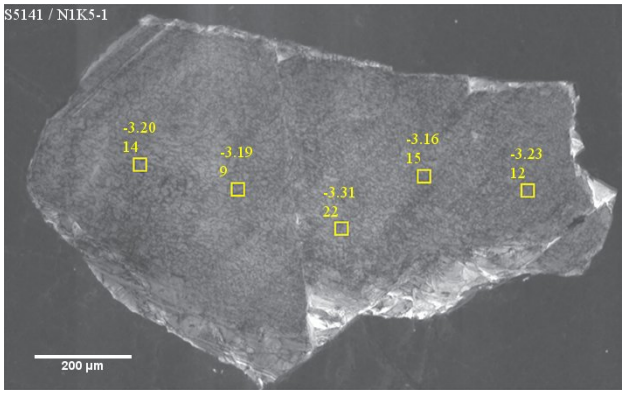
S5141 / N1K5-1
-3.20
14
-3.19
9
-3.31
22
-3.16
15
-3.23
12
200 µm

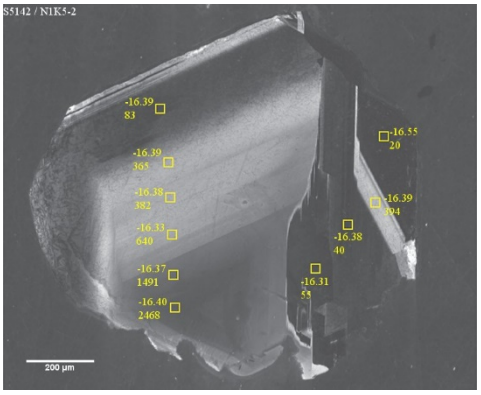
S5142 / N1K5-2
-16.39
83
-16.39
365
-16.38
382
-16.33
640
-16.37
1491
-16.40
2468
-16.55
20
-16.39
204
-16.38
40
-16.31
53
200 µm

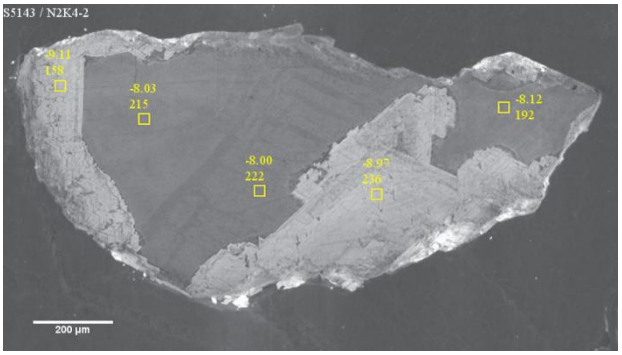
S5143 / N2K4-2
-8.11
158
-8.03
215
-8.00
222
-8.97
230
-8.12
192
200 µm

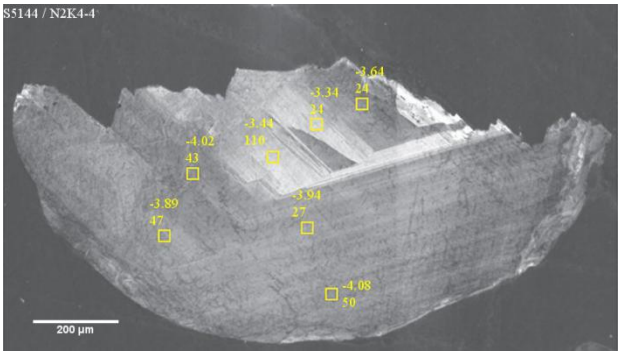
S5144 / N2K4-4
-3.64
24
-3.34
24
-3.44
110
-4.02
43
-3.89
47
-3.94
27
-4.08
50
200 µm

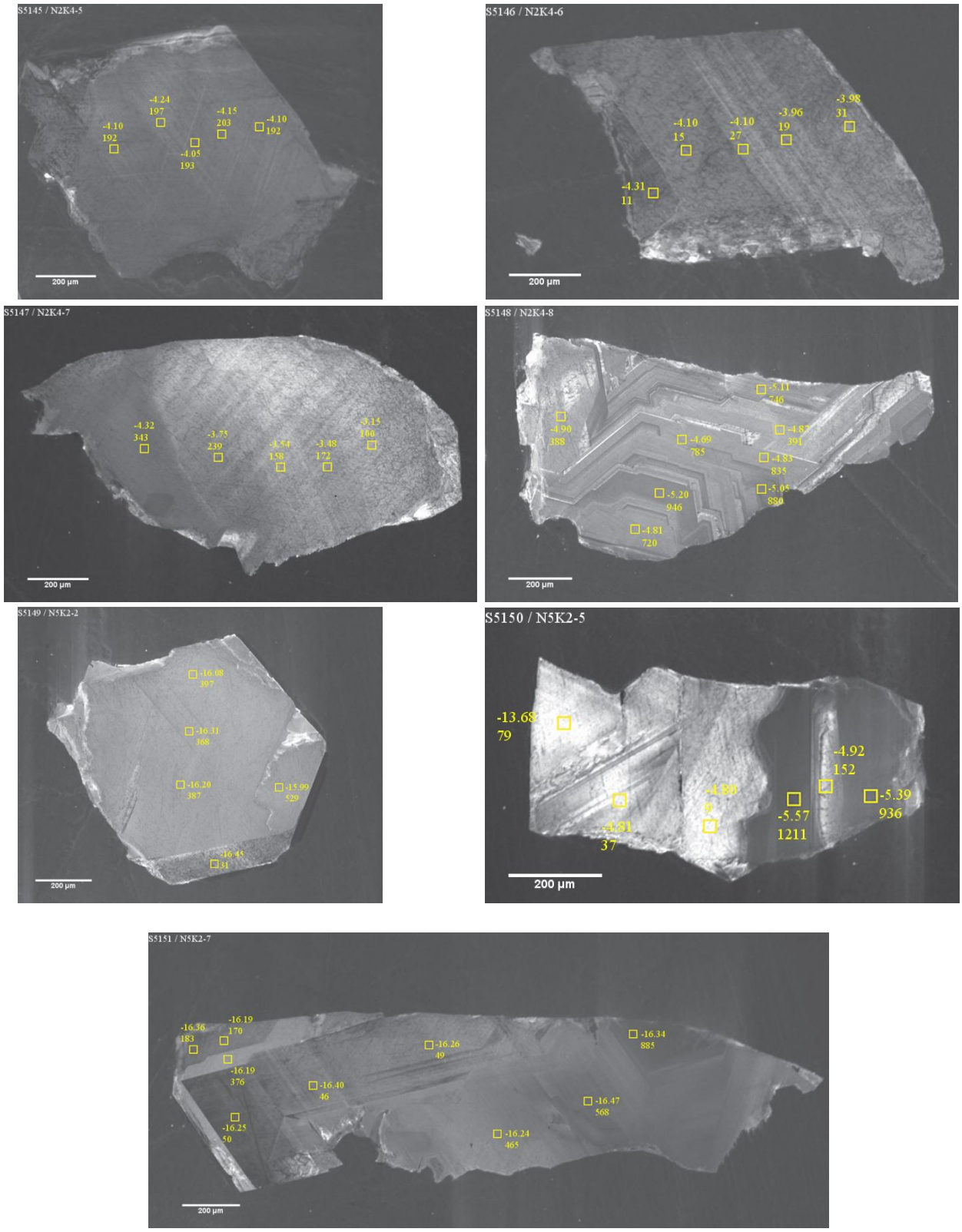

Figure C.1. Annotated CL images of twenty-two inclusion-bearing diamonds. Number on top is $\delta^{13}C$ in ‰, number below is nitrogen content in at. ppm.